UNIVERSITY OF ALBERTA

MEASUREMENT OF WATER-NMR RELAXATION IN PERIPHERAL NERVE

BY

MARK D. DOES

©

A thesis submitted to the Faculty of Graduate Studies and Research in partial fulfillment of the requirements for the degree of

DOCTOR OF PHILOSOPHY
in
MEDICAL SCIENCES – BIOMEDICAL ENGINEERING

Edmonton, Alberta
FALL 1997

National Library of Canada
Acquisitions and Bibliographic Services
395 Wellington Street
Ottawa ON K1A 0N4
Canada

Bibliothèque nationale du Canada
Acquisitions et services bibliographiques
395, rue Wellington
Ottawa ON K1A 0N4
Canada

Your file Votre référence

Our file Notre référence

The author has granted a non-exclusive licence allowing the National Library of Canada to reproduce, loan, distribute or sell copies of this thesis in microform, paper or electronic formats.

L'auteur a accordé une licence non exclusive permettant à la Bibliothèque nationale du Canada de reproduire, prêter, distribuer ou vendre des copies de cette thèse sous la forme de microfiche/film, de reproduction sur papier ou sur format électronique.

The author retains ownership of the copyright in this thesis. Neither the thesis nor substantial extracts from it may be printed or otherwise reproduced without the author's permission.

L'auteur conserve la propriété du droit d'auteur qui protège cette thèse. Ni la thèse ni des extraits substantiels de celle-ci ne doivent être imprimés ou autrement reproduits sans son autorisation.

0-612-22976-9

Canada

UNIVERSITY OF ALBERTA

LIBRARY RELEASE FORM

NAME OF AUTHOR: Mark D. Does

TITLE OF THESIS: Measurement of Water-NMR Relaxation in Peripheral Nerve

DEGREE: Doctor of Philosophy

YEAR THIS DEGREE GRANTED: 1997

Permission is hereby granted to the University of Alberta Library to reproduce single copies of this thesis and to lend or sell copies for private, scholarly, or scientific research purposes only.

The author reserves all other publication and other rights in association with the copyright in the thesis, and except as hereinbefore provided, neither the thesis nor any substantial portion thereof may be printed or otherwise reproduced in any material form without the author's prior written permission.

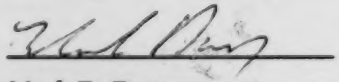

Mark D. Does

142 York St., Apt. #1

New Haven, CT

06510, USA

DATE: 28/7/97

UNIVERSITY OF ALBERTA

FACULTY OF GRADUATE STUDIES AND RESEARCH

The undersigned certify that they have read, and recommend to the Faculty of Graduate Studies and Research for acceptance, a thesis entitled MEASUREMENT OF WATER-NMR RELAXATION IN PERIPHERAL NERVE submitted by MARK D. DOES in partial fulfillment of the requirements for the degree OF DOCTOR OF PHILOSOPHY in MEDICAL SCIENCES–BIOMEDICAL ENGINEERING.

Richard E. Snyder (Supervisor)

Peter S. Allen

Brian J. Andrews

Tessa Gordon

Richard B. Stein

R. Mark Henkelman

DATE: July 25, 1997

D. Gwyn Hughes

Abstract

This thesis contains four studies, each of which involves measurement of water-NMR relaxation in peripheral nerve in some manner. The central basis of these studies is that peripheral nerve water exists in three broadly unique environments—myelinic, intra-axonal, and extra-axonal.

In the first study, multi-echo imaging identified three transverse relaxation (T_2) components in the frog sciatic nerve, including a long-lived component ($T_2 >$ 200 ms) which previously had only been identified *in vitro*. The existence of a long-lived T_2 component indicated echo times of 200-300 ms may provide maximal contrast-to-noise (*CNR*) (nerve to muscle) in T_2-weighted images. Averaging selected images from the multi-echo image set, the *CNR* was increased by a factor of nearly three.

In the second study, multi-echo imaging and *in-vitro* measurements showed progressive changes in the T_2-spectra of frog sciatic nerve undergoing Wallerian degeneration. The two most apparent changes as degeneration progressed were a reduction from three well-resolved T_2 components to one and a decline in the fraction of the spectra associated with short-lived T_2. The former change appears to reflect a collapse of myelinated fibres, while the latter a combination of interstitial oedema and myelin loss.

The third study found that each of the three T_2 components of peripheral nerve water exhibited unique longitudinal relaxation (T_1) and magnetisation transfer characteristics. Simulations demonstrated that mobile water exchange between axonal and myelinic components was not necessary to explain their similar steady-state magnetisation transfer contrast (*MTC*)s, and reasoning dictated that water exchange cannot be the primary mechanism for this similarity. Rather, the similar *MTC* of the two shorter-lived T_2 components results from

differing intrinsic T_1s. Therefore, interpreting *MTC* change to solely reflect a change in degree of myelination could lead to erroneous conclusions.

Finally, the fourth study used computer simulations and experimental data to demonstrate that when using sub-optimal spoiler gradients in a multi-echo imaging sequence, increasing the first spoiler gradient slightly reduces the fraction of unwanted signal by several times, resulting in T_2 measurements within 1% of those obtained using optimal spoiler gradients. Use of this spoiler adjustment reduces the peak spoiler gradient requirement by a factor of 2-4.

Acknowledgements

Giving due credit to all deserving credit for contributing to this thesis is more or less impossible becaue I am really nothing more than a reflection of a combination of all those who have shaped my life.

The most obviously important person to my doctoral studies has been Dr. Richard Snyder. Without a question, I'd be nowhere along this path without him. His efforts to secure my opportinity to pursue a PhD. were, in and of themselves, a tremendous feat. Additionally, and no less signficantly, he has been an excellent personal mentor: he is hard working and driven toward excellence, appreciates the value of science, and yet, all the while, he tempers his actions with a tremendous amount of compassion to his fellow human being. From day one he treated me and my thoughts with respect, and he went far out of his way to support me in both my personal and professional life. In addition to his love, I was also fortunate enough as to receive a wonderful amount of loving support from Rick's lovely wife Deloris, who's kind words boosted my spirits on several occasions.

Beyond my immidiate supervisor, there are several other professors to whom I am in debt. It's safe to say that without the preceeding and on-going work of Dr. Peter Allen the potential for my studies in medical Nuclear Magnetic Resonance at the U. of A. would be unlikely to exist. During my years as a graduate student Peter provided me with opportunities to research as well as vital insights into the field. In my experience he has been a kind and respectful man in addition to being an excellent scientist.

Additionally, Dr. Zoltan Koles has been an excellent mentor and friend. Although we have not worked together in research during my PhD. stuidies, his efforts to provide me teaching opportunities are tremendously appreciated. I also greatly appreciate the time we've spent together, over beers or around the lunch table, discussing science, politics, and life in general. Cheers to you Zoly.

I'd also like to thank the remaining examiners of my thesis: Dr. Gwynn Hughes, Dr. Brian Andrews, Dr. Tessa Gordon, Dr. Richard Stein, and Dr. Mark Henkelman. In particular I should point out that Gwynn's careful, thorough reading of my thesis and his accompanying advice was invaluable. I also appreciate Mark Henkelman making the journey from Toronto to attend my defense in person.

The entire group of staff and students in Biomedical Engineering have made studying/playing here a great time. In particular I'd like to thank Christian Beaulieu ("That's Dr. Beaulieu, to you.") for teaching me many tricks of the trade, sharing scientic insights, and, most of all, being an excellent friend – in return for which, I've done my best to teach him how to drink beer. Rich

Thompson (who needs no tutelage in drinking) falls into the same category. He gladly responded to all my physics questions, routinely out-golfed me (ok, Chris out-golfs me now, but that's a recent phenomenon), and throws an excellent party.

Ion Buicliu bravely battled and conquered the computer gremlins who sought to thwart my work, and, moveover, brought with himself every day a level of thought, taste, and kindness that made the office evironment a pleasureable one. Also, (and these are two others who've taken the pleasure in thrashing me on the golf course), Dan Doran and Karim Damji were vital in my learning the ins and outs of those crazy machines. Without Dan answering seven questions a day for the first six months of my studies I'd still be trying to generate my first image. It's a shame that new students now do not have the benefit of their friendly and proficient assistance.

Dr. Ming Chen (microscopy master) and Rosie Vishram (frog surgeon master) both played crucial roles in service and teaching, and alway did so in the most friendly way. Additionally, Dan Gheorghiu, Chris Hanstock, Carol Tymchuk, and Maisie Goh contribute routinely to the mechanics of this group. We'd all be at a standstill without their efforts. And finally, I should point out that although Adam Thrasher and Rich Williamson failed to make a chess player out of me, they and Angela Antoniu, Caroline Tam, and Nora O'Neil have made the tenth floor a lot of fun and a supportive group. Thanks.

And, of course, I must thank my immediate familiy – Mom, Dad, Karon and Drew – for their ongoing friendship and support. Additionally, I'd like to thank my extended family, Academy, who, like clockwork, saved me from becoming a hard-working student every Friday since ... I can't even remember (although, it's because of them that I really can't remember much). The task of thanking all of Academy individually is impossible: I'd be writing half the day. You know who you are, and you know that I love you all.

Table of Contents

CHAPTER 1. BACKGROUND 1

OVERVIEW 1
PERIPHERAL NERVE 2
Normal Anatomy 2
Degeneration and Regeneration 2
Assessing Nerve Injury and Repair 4
NUCLEAR MAGNETIC RESONANCE 5
Principles of Nuclear Magnetic Resonance, in brief 6
Interaction of Water ^{1}H with Magnetic Fields 6
Relaxation 8
Magnetisation Transfer 11
NMR Measurement and Analysis Techniques 13
Signal Detection and Image Generation 13
Relaxometry: T_2 15
Relaxometry: T_1 18
Magnetisation Transfer 19
Simulation of Multi-Echo MRI 20
NMR Properties of Peripheral Nerve 23
Transverse Relaxation of Peripheral Nerve Water 23
Magnetisation Transfer in Peripheral Nerve 25
REFERENCES 26

CHAPTER 2. T_2 RELAXATION OF PERIPHERAL NERVE MEASURED *IN VIVO*[1] 29

INTRODUCTION 29
METHODS 30
Animal Model 30
Imaging Studies 30
In vitro Studies 31
Analysis of Data 31
RESULTS 31
DISCUSSION 33
CONCLUSION 34
REFERENCES 36

CHAPTER 3. MULTI-EXPONENTIAL T_2 RELAXATION IN DEGENERATING PERIPHERAL NERVE[1] 37

INTRODUCTION 37
METHODS 38
Animal Model 38
In-Vitro Studies 38
Imaging Studies 39
RESULTS 40
Magnetic Resonance 40
Histology 44
DISCUSSION 45
CONCLUSION 48

REFERENCES 49

CHAPTER 4. MULTI-COMPONENT T_2 AND MT IN PERIPHERAL NERVE[†] 51

INTRODUCTION 51
METHODS 52
Longitudinal Relaxation 52
Magnetisation Transfer 53
RESULTS 55
Longitudinal Relaxation 55
MT measurements 57
DISCUSSION 58
Longitudinal Relaxation 58
Magnetisation Transfer 59
CONCLUSION 63
REFERENCES 65

CHAPTER 5. MULTI-ECHO IMAGING WITH SUB-OPTIMAL SPOILER GRADIENTS[‡] 66

INTRODUCTION 66
SPOILER GRADIENTS 66
METHODS AND RESULTS 68
Coherence Pathway Simulations 68
Bulk-Magnetisation Simulations 70
Slice Selection 71
MRI Measurements 72
DISCUSSION 73
Minimising Unwanted Signal 73
Factors Affecting $S_{...}$ 75
CONCLUSION 78
REFERENCES 80

CHAPTER 6. CLOSING COMMENTS 81

APPENDIX I MATLAB™ PROGRAMS 83

WARNING/DISCLAIMER 83
T_2 PROCESSING 83
2D PROCESSING 85
MAGNETISATION TRANSFER SIMULATION AND PROCESSING 86
MULTI-ECHO SIMULATIONS BY COHERENCE PATHWAY 88
MULTI-ECHO SIMULATIONS BY BLOCH EQUATION 92

List of Tables

Table 2.1. Measured multi-exponential transverse relaxation times of nerve and muscle. 33
Table 3.1. Image (*In vivo*) measured T_2 parameters (± S.D.) of normal and degenerating peripheral nerve..... 45
Table 4.1. Estimated values of various parameters of the two-pool model for all three T_2 components of peripheral nerve water..... 55
Table 5.1. Parameter values used in simulations..... 68
Table 5.2. Observed T_2s from 32 echo simulations using a range of R_1 and R_2 values..... 76

List of Figures

Fig. 1.1. A cross-section of peripheral nerve (sciatic nerve of the frog, see Fig 3.6) identifying the three broad types of unique water environments. 2
Fig. 1.2. Two-pool model of magnetisation transfer. 12
Fig. 1.3. A tree representing the possible coherence pathways of a multi-pulse sequence. 22
Fig. 2.1. Four transverse images from a 32-echo set of the thigh of *Xenopus laevis*. 32
Fig. 2.2. T_2 spectra of the sciatic nerve of *Xenopus laevis* measured a) *in vitro* and b) *in vivo*. 34
Fig. 2.3. Image obtained by averaging the 11th through 25th echo images of the 32-echo set presented in Fig. 2.1. 35
Fig. 3.1. T_2 spectra of the sciatic nerve of *Xenopus* measured *in vitro*, corresponding to a) normal, b) 7 days post-injury, c) 15-16 days post-injury, and d) 28-31 days post-injury. 41
Fig. 3.2. Four transverse images from the thigh of *Xenopus* corresponding to a) normal, b) 7 days post-injury, c) 14 days post-injury, and d) 32 days post-injury. 42
Fig. 3.3. Signal intensity versus echo time for normal and degenerating nerve. 43
Fig. 3.4. Typical T_2 spectra of the sciatic nerve of *Xenopus* measured *in vivo*, corresponding to a) normal, b) 7 days post-injury, c) 14 days post-injury, and d) 32 days post-injury. 44
Fig. 3.5. Fraction of spectra corresponding to low T_2 component determined from *in-vivo* measurements versus time following operation. 46
Fig. 3.6. Light micrographs of sciatic nerve of *Xenopus*. 47
Fig. 4.1. T_2 spectra from one nerve following different SR delays in a combination SR-CPMG pulse sequence. 56
Fig. 4.2. Saturation recovery curves for each of the three nerve water components segmented from T_2 spectra as shown in Fig. 4.1. 57
Fig. 4.3. T_1 spectra resulting from NNLS fits of each of the SR curves plotted in Fig. 4.2, corresponding to the three nerve water T_2 components. 59
Fig. 4.4. Direct 2-D T_1-T_2 NNLS fits of SR-CPMG data from two different nerve samples. 60
Fig. 4.5. A normal frog nerve T_2 spectrum (shaded dark) and the T_2 spectrum of the same nerve following off resonance rf saturation (shaded light). 61
Fig. 4.6. Steady-state longitudinal magnetisation of each of the three nerve water T_2 components following rf saturation at various off resonance frequencies. 62
Fig. 4.7. Longitudinal magnetisation of each of the three nerve water T_2 components and the buffer component following off resonance rf saturation pulses of various durations. 63
Fig. 4.8. Calculated steady-state longitudinal magnetisation of each of the three nerve water T_2 components given saturation rf at various off resonance frequencies and R_{ex}s estimated from the acquired T_{1ss} data. 64
Fig. 5.1. Spoiler gradient pattern for quantitative multi-echo imaging. 67
Fig. 5.2. Observed T_2s as a function of the spoiler adjustment, S_{adj}, for four cases of minimum spoiler gradient strength. 69
Fig. 5.3. Mean contribution per echo of magnetisation from the T_1-artefact pathways as a function of the spoiler adjustment, S_{adj}, for four cases of minimum spoiler gradient strength. 70
Fig. 5.4. Mean contribution per echo of magnetisation from the phase-artefact pathways as a function of the spoiler adjustment, S_{adj}, for four cases of minimum spoiler gradient. 71
Fig. 5.5. Amplitudes of unwanted pathways contributing to the eighth echo under the condition $S_{min} = \pi$ and (a) $S_{adj} = 0$, (b) $S_{adj} = 0.7\pi$. 72
Fig. 5.6. Echo magnitudes from 32 echo bulk-magnetisation simulations using the parameters given in Table 5.1. 73
Fig. 5.7. Difference between T_{2OPT} and T_{2OBS} as a percentage of T_{2OPT} plotted as a function of amplitude missetting of the rf refocussing pulse (B_{MIS}), with the offset frequency from resonance of the rf refocussing pulse (B_{OFF}) held constant at 25 Hz. 74

Fig. 5.8 Difference between T_{2OPT} and T_{2OBS} as a percentage of T_{2OPT} plotted as a function of the offset frequency from resonance of the rf refocussing pulse (B_{OFF}), with amplitude missetting of the rf refocussing pulse (B_{MIS}) held constant at 5%..... 75
Fig. 5.9 Mean contribution per echo of magnetisation from the T_1- and phase-artefact pathways as a function of the spoiler adjustment, S_{adj}, for $S_{adj} = \pi$ and four cases of slice offset (Θ) divided by slice thickness (δ). 77
Fig. 5.10. MRI echo magnitudes from 8 echo acquisitions..... 78

List of Symbols and Abbreviations

β	Correction term for imperfect saturation in T_1 processing.
γ	Gyromagnetic ratio for ^1H.
δ	Slice thickness.
ε	Relaxation term for a given time interval and coherence level.
η	Difference between N^- and N^+.
θ, α	Magnetisation tip angles.
λ	Smoothing weighting variable in NNLS fits.
μ	Magnetic moment.
Θ	Slice offset.
ρ	Time-dependent phase term.
τ	Utility timing variable for pulse sequence timing.
φ	Phase shift due to a spoiler gradient.
ϕ	Rf pulse phase angle.
χ^2	Chi-squared statistic.
ψ	Net phase term from a given coherence pathway in a particular pulse sequence.
ω	Angular frequency. Subscripted with 0 to define Larmor frequency, and with rf to define frequency of B_1 field.
Ω, Δ	Off resonance frequency in radians/sec and Hz, respectively.
$\vdash\rangle, \vdash\rangle$	Energy eigenstates.
A, S	Fitting and solution matrices, respectively, in NNLS fits.
B	Magnetic Field. Subscripted with 0 to define applied static field and with 1 to define applied radio-frequency field., and bolded to define a vector.
B_{MIS}	Rf pulse missetting factor.
B_{OFF}	Rf pulse off resonance frequency (same as Δ).
C	Utility constant of integration.
CNR	Contrast to noise ratio.
f	Scalar relating transfer of magnetisation from one coherence level to another.
$\hbar$	Planck's constant divided by 2π.
G	Gradient amplitude.
H	Hamiltonian operator.
i, j, k	Unit direction vectors.
I	Nuclear spin number.
k	Boltzmann's constant.
M	Magnetisation. May be subscripted or superscripted to define unique type, or bolded to define a vector.
MTC	Magnetisation Transfer Contrast.
n, m	Utility integer indices.

N, K	Utility matrix dimensions. May be subscripted to define unique type.
NE	Number of echoes in spin-echo pulse sequence.
N^-, N^+	Population of spins in energy eigenstates $\|-\rangle$ and $\|+\rangle$, respectively.
p	Coherence level. In bold defines a pathway of levels.
r_{lm}	Elements of a rotation matrix.
R	Rotation matrix.
R_{ab}, R_{ba}	Magnetisation transfer exchange rates.
R_{rf}	Rate of rf energy absorption.
S_{min}	Strength of the weakest pair of spoiler gradients in Poon-Henkelman multi-echo imaging pulse sequence.
S_{add}	Strength of additional gradient added to the first spoiler of a Poon-Henkelman multi-echo imaging pulse sequence.
T	Temperature in degrees kelvin.
T_1, R_1	Longitudinal relaxation time and rate.
T_2, R_2	Transverse relaxation time and rate.
T_{1sat}, R_{1sat}	Longitudinal relaxation time and rate, respectively, when semi-solid magnetisation is saturated.
T_{2OBS}	Measured transverse relaxation time.
T_{2OPT}	Measured transverse relaxation time in the case of optimal spoiler gradients.
TE	Echo time in spin-echo pulse sequence.
TR	Pulse sequence repetition time.
W^-, W^+	Probability per unit time of transitions from $\|-\rangle$ and $\|+\rangle$, and vice versa.
W	Average of W^- and W^+.
x, y, z	Cartesian coordinate axes.
CNS	Central Nervous System
EAE	Experimental Allergic Encephalomyelitis
EMG	Electromyogram
ENG	Electroneurogram
HTS	Hoffman-Tinal Sign
IR	Inversion recovery
MET_2	Multi-exponential T_2
min	Minutes
MRI	Magnetic Resonance Imaging
MS	Multiple Sclerosis
MT	Magnetisation Transfer
NEX	Number of excitations
NMR	Nuclear Magnetic Resonance
NNLS	Non-negative least squares
PNS	Peripheral Nervous System
rf	Radio-frequency
ROI	Region of interest
SR	Saturation recovery

Chapter 1. Background

Overview

This work herein, a quantitative investigation of some characteristics of the nuclear magnetic resonance (NMR) signal of normal and injured peripheral nerve and methods of their measurement, represents a contribution to a research programme aiming towards understanding how various NMR tissue characteristics can serve to differentiate between various pathophysiologic states of nerve and how these characteristics can be measured *in vivo* using magnetic resonance imaging (MRI).

Following a severe enough injury, a peripheral nerve degenerates and attempts to regenerate. Regeneration is a slow process and may not be quantifiable or even detectable in humans for many weeks or months after the original trauma. If no signs of spontaneous regeneration can be found surgical repair of the nerve may be attempted. However, if many months are required to determine that little or no spontaneous regeneration is taking place recovery will at least be greatly delayed and at worst significantly reduced in likelihood. For this reason an effective method of assessing peripheral nerve following injury would be of great value. MRI offers unique attributes, such as the ability to probe changes in microanatomy, that make it a promising diagnostic tool for assessing peripheral nerve.

Magnetic resonance imaging is being extensively investigated as a tool for assessing nervous tissue. The vast majority of nerve-related MRI research has been aimed at central nervous system (CNS) tissue and diseases thereof. However, as is discussed below, within the past few years it has been demonstrated that MRI can be used to visualize the peripheral nervous system (PNS) as well. Also, MRI technology is currently advancing from simply a tool for visualizing tissues to a tool for measuring NMR signal characteristics which may serve as anatomic or physiologic indicators. The hypothesis upon which this programme is based is that some combination of these NMR signal characteristics can be measured *in vivo* using MRI, and that these measures will identify and quantify various pathophysiologic states of nerve tissue. The work presented within chapters 2 through 4 of this thesis use this hypothesis to: i) demonstrate a method of visualising peripheral nerve using MRI, ii) investigate the change of one particular NMR signal characteristic (transverse relaxation) during the degeneration of peripheral nerve, and iii) investigate the nature of two other NMR signal characteristics in the context of peripheral nerve micro-anatomy. The fifth chapter of this thesis presents the development of an experimental technique that aids in the accurate measurement of transverse relaxation using MRI.

Peripheral Nerve

Normal Anatomy

(Sunderland, 1991)

A healthy peripheral nerve consists, on a gross level, of both myelinated and nonmyelinated axons interspersed with supportive connective tissue. The axon itself, whether myelinated or not, is composed of a central core of axoplasm enclosed by a membrane known as the axolemma. In addition to typical intracellular components such as mitochondria and endoplasmic reticula, axoplasm also contains neurofilaments and microtubules. These constituents are long fibrous elements oriented parallel to the length of the axon, providing structural support to the axon and contributing to axonal transport functions. In the case of myelinated axons (which dominate in the particular nerve-type discussed in chapters 2 through 4 of this thesis), the axolemma is wrapped by many membrane layers of Schwann cells. This wrapping is called myelin and serves to insulate the intra- from extra-axonal environments. Regions of myelin extend along the entire axon in segments approximately 1 mm in length, separated by narrow (1 to 20 μm) unmyelinated regions known as the Nodes of Ranvier, at which membrane depolarisation occurs during the propagation of an action potential.

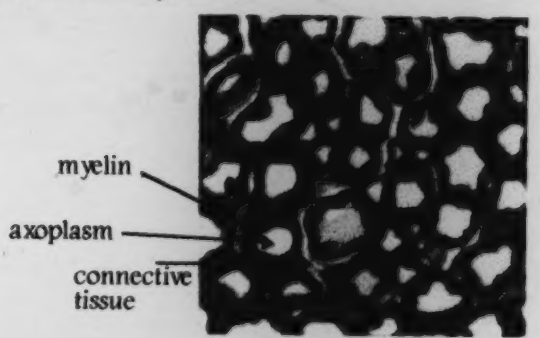

Fig. 1.1. A cross-section of peripheral nerve (sciatic nerve of the frog, see Fig 3.6) identifying the three broad types of unique water environments.

In the context of this thesis, the important characteristic of nerve anatomy is the three broad types of unique water environments: intra-axonal, extra-axonal, and myelinic (see Fig. 1.1). Each of these environments is thought to yield unique nuclear magnetic resonance characteristics, a topic which is discussed in more detail in chapters 2 through 4.

Degeneration and Regeneration

(Dyck, 1975; Schröder, 1975; Sunderland, 1991; Vrbová et al., 1995)

Focal pressure on the nerve may disturb the myelin sheath resulting in a localised demyelination, or neurapraxia. With removal of pressure this condition is rapidly self-correcting. However, if this pressure is significant enough to interrupt the axon as well, both axons and myelin degenerate distal to the lesion in a manner first described by Waller in 1850 (Waller, 1850) and henceforth known as Wallerian degeneration. When the continuity of the nerve is maintained by its connective tissue the axonal interruption is termed an axonotmesis, while complete nerve severance is called neurotmesis, each of which result in Wallerian degeneration.

The morphological characteristics of Wallerian degeneration are relatively well understood and bear significant similarity between species. The first anatomical changes to the distal axon during degeneration is the disintegration of the cytoskeleton—neurofilaments and microtubules—into granular debris. This loss of axoplasmic continuity results in the inability of the nerve to conduct action potentials. Shortly after the onset of axonal breakdown, the myelin begins to deteriorate. The myelin separates into short segments which collapse around axonal remains forming ovoids. Slowly, these ovoids are removed by phagocytosis, leaving behind basal lamina tubes. Concurrently with the breakdown and subsequent removal of myelin and axons, Schwann cells proliferate and fill the basal lamina tubes resulting in the so-called bands of Büngner, which provide physical guidance and trophic support for regenerating axons.

Axonal regeneration begins almost immediately following the onset of Wallerian degeneration. The rate of axonal growth varies within a given nerve, from nerve to nerve, across species, and as a function of distance from lesion site. In general, though, regeneration rates in human are between 1 and 5 mm/day, and are roughly four times slower in poikiotherms. From each parent axon in the proximal stump several daughter axons proceed in the distal stump along the bands of Büngner. All of these daughter axons remain and begin myelinating until one makes connection with the target, at which point the other daughter axons die away. Regenerating axons are much smaller in diameter than normal and do not begin to increase significantly in size until functional connection has been established, following which time they grow to the size of their parent.

While the prognosis for spontaneous recovery following axonotmesis is generally good, surgery is required to sustain axonal regeneration following neurotmesis. If surgery follows injury by less than 72 hours (Sunderland, p. 418, 1991), it may be possible to use electrical scanning techniques to assist in matching proximal and distal nerve stumps on a fasicular level. Successful recovery following Wallerian degeneration includes both well guided axon regeneration as well as complete reinnervation. The ability of an atrophic muscle to accept reinnervation is dependent on the degree of atrophy which

increases with time after denervation. For these reasons, early determination of the degree of nerve injury is important for optimizing the prospects of full functional recovery.

Assessing Nerve Injury and Repair

(Frykman et al., 1988; Sunderland, 1991; Parry, 1992; Chaudhry et al., 1992)

Electrodiagnostic measurements in combination with observation of various clinical signs presently constitute the best means of locating nerve lesions, identifying the type of damage, and assessing axonal regeneration. However, there are significant shortcomings in all three of these evaluations, most particularly, the latter—assessing axonal regeneration. Two broad types of electrodiagnostic measurement are used to assess neuromuscular injuries and disorders. The electromyogram (EMG) is a measure of the muscle electrical activity, usually following voluntary or externally applied stimulation of the motor nerve. Alternatively, the action potentials in nerve can be measured directly resulting in the electroneurogram (ENG). In addition to electrodiagnostics, various clinical signs aid in nerve injury diagnosis and prognosis.

Clinically locating a nerve lesion may be straightforward if the wound is open and the lesion is clean (such as a severance due to an impalement); however, electrodiagnostic methods are generally employed to locate lesions. For a variable length of time (hours to days, depending on length of nerve distal to injury site) following both axonotmesis and neurotmesis the distal nerve stump will still conduct action potentials. Thus, the EMG can be used to locate a nerve lesion by finding the most proximal point at which electrical stimulation of the nerve elicits an EMG response. In situations where the nerve damage is broad or jagged, the EMG may provide an incomplete spatial description of the lesion. Surgical exploration in combination with invasive ENG may be required to locate all lesions in complicated injuries.

In addition to locating a nerve lesion, it is also desirable to identify the extent of the injury as soon as possible. If enough time is allowed for the distal stump to degenerate, an EMG can be used to differentiate between neurapraxia and either axonotmesis or neurotmesis, because, in the case of the former, stimulation distal to the lesion will still elicit motor response. Also the EMG can identify denervation with the observation of fibrillation potentials at the neuromuscular junction. This measurement also requires a delay of sufficient time following injury for the distal nerve stump to degenerate and is limited in that the amount of denervation is difficult to quantify from fibrillation potentials. A more important diagnosis is the differentiation between axonotmesis and neurotmesis, as the former may require surgery while the latter certainly will, and, as mentioned above, the prognosis of recovery

following surgery decreases with time following injury. Electrodiagnostic techniques, however, are unable to distinguish between complete axonotmesis and neurotmesis. Currently, this differential diagnosis requires surgical exploration or one must wait for clinical signs of recovery to rule out the need for surgical repair. Even with surgical exploration, determining the severity of nerve damage may not be straightforward or even possible. In cases of brachial plexus injuries, neurotmesis of some branches does not preclude the partial or complete axonotmesis in other branches, which may not be visually obvious. Also, visually identifying a lesion as an axonotmesis does not preclude the necessity for surgery, although the decision to surgically repair an injury which may spontaneously regenerate should only be undertaken when no indication of such regeneration is observed. Therefore, the observation of clinical signs of axonal regeneration, spontaneous or after surgical repair, is fundamental in diagnostic and prognostic assessments of many nerve injuries.

The EMG can be used to identify denervation and subsequent reinnervation but gives no indication of axonal regrowth prior to reinnervation. On the other hand, the ENG can directly indicate the existence and estimate the number of conducting axons at a particular point along the nerve. However, the ENG is difficult to measure non-invasively. Percutaneous measurements of the ENG have poor sensitivity and may not be able to identify, let alone quantify, signals from deeply situated nerves. Furthermore, the spatial resolution of percutaneous ENG measurements is also poor, rendering it incapable of distinguishing between nerves with close proximity to each other. It is possible to perform invasive ENG measurements during surgery. Such an invasive approach carries obvious increased risk to the patient, and is entirely impractical for assessing regeneration on a repeated basis.

Aside from electrodiagnostics, there is the Hoffmann-Tinel sign (HTS), which is a tingling sensation elicited by a light percussion of the nerve trunk. The most distal point at which the HTS can be elicited indicates the furthest progression of regenerating sensory axons. However, this method, like the percutaneous ENG, has poor spatial resolution and may not elicit a response from deeply situated nerve trunks. Moreover, the HTS indicates only the furthest point of sensory axon regeneration, yielding no estimation of the number of regenerating axons, nor any indication of motor axon regeneration. Therefore, although identifying and quantifying axonal regeneration is fundamental in assessing nerve injury and repair, the methods available to do so are poor. Magnetic resonance imaging possesses the potential to fill this role well.

Nuclear Magnetic Resonance

The phenomenon of nuclear magnetic resonance (Bloch et al., 1946; Purcell et al., 1946) lends itself well to medical imaging for two important reasons. First, the NMR signal can be localised in three-dimensional space, which allows for

the generation of nuclear magnetic resonance images (NMRI or, more simply, MRI) (Lauterbur, 1973). Second, while not all atomic nuclei exhibit the phenomenon of NMR, the most abundant atomic nucleus in the human body, ^1H, does. The vast majority of ^1H nuclei exist within water molecules, which means, for medical purposes, MRI visualizes water in the body. However, the image contrast is not simply a function of water density. In fact, one of the unique capabilities of MRI is that the image contrast can be manipulated.

The NMR signal is dependent on several parameters which are sensitive to the physical and chemical environments of tissue, three of which are of particular interest to this thesis: transverse relaxation time (T_2), longitudinal relaxation time (T_1), and magnetisation transfer (MT). During MR image acquisition the NMR signal can be manipulated to weight the contribution of each of these signal parameters, thus allowing the mechanisms of image intensity to be controlled. For example, an image in which pixel intensity is primarily related to transverse-relaxation is referred to as a T_2-weighted image and will allow tissues with different T_2 characteristics to be distinguished from one another. Currently, MRI is moving from generating images which are weighted by a particular parameter, to measuring the parameter itself. That is, while one T_2-weighted image will allow for segmentation of tissues with differing T_2s, several images with different T_2 weightings can be used to measure the T_2 of a particular tissue, which may vary depending on its pathophysiologic state.

Principles of Nuclear Magnetic Resonance, in brief

Before venturing into the current and potential value of magnetic resonance imaging for assessing nerve pathologies, a brief description of the phenomenon known as NMR is in order.

Interaction of Water ^1H with Magnetic Fields

(Andrew, 1955; Slichter, 1990; Allen, 1994)

Water, the most abundant molecule in the body, is composed of one oxygen atom and two hydrogen atoms. From an NMR perspective, the oxygen atom means little to us, but the hydrogen atoms are meaningful because their nuclei (which are simply protons in the typical case of the ^1H isotope) possess a net magnetic moment. It is the interaction between these magnetic moments and externally applied magnetic fields that is the basis of the phenomenon known as NMR.

A proton (as well as other elementary particles such as neutrons and electrons) possesses an intrinsic property known as angular momentum, $\hbar I$, which relates to a magnetic moment with the fundamental equation $\mu = \gamma \hbar I$, where $\hbar$ is Planck's constant dividend by 2π and γ is known as the gyromagnetic ratio ($\approx 26.76 \times 10^3$ radians/(sec·Gauss) for ^1H). The interaction energy between such a magnetic moment and a static, uniform magnetic field, B_0, is given by the

Zeeman Hamiltonian, $\mathcal{H} = -\gamma\hbar\mathbf{I}\cdot\mathbf{B}_0$, which reduces to the scalar operation $\mathcal{H} = -\gamma\hbar I_z B_0$ when the z-axis is defined in the direction of the static magnetic field. In the case of protons, for which $I = 1/2$, the solution of the Schrödinger equation for this Hamiltonian yields two energy eigenstates, $|+\rangle$ and $|-\rangle$, with relative spin populations of N_0^+ and N_0^-, and their corresponding eigenvalues $-\gamma\hbar B_0/2$ and $\gamma\hbar B_0/2$.

At thermal equilibrium, the distribution of spins between the two eigenstates is dictated by the Boltzmann distribution:

$$N_0^+/N_0^- = \exp(\gamma\hbar B_0/kT), \qquad [1.1]$$

where k is Boltzmann's constant and T is the temperature in kelvins. This function indicates that a majority (a very slim majority at room temperature with a typical $B_0 \approx 1$ Tesla) of spins will exist in the lower energy eigenstate. Thus, an ensemble of spins at thermal equilibrium will result in a net magnetic moment, or net magnetisation ($|\mathbf{M}| = M_0$), aligned with the direction of the magnetic field $\mathbf{B}_0$. It is this net magnetisation that one manipulates and observes during the course of an NMR experiment.

From classical mechanics it can be said that in the presence of a magnetic field, a magnetic moment will experience a torque causing it to precess about the axis defined by the direction of the magnetic field, as described by

$$d\mathbf{M}/dt = \gamma\mathbf{M}\times\mathbf{B}. \qquad [1.2]$$

In the practice of an NMR experiment, the magnetic field is composed of a static component, $\mathbf{B}_0$, and a time-varying component, normally called $\mathbf{B}_1$. This $\mathbf{B}_1$ is circularly polarised in the plane to which $\mathbf{B}_0$ is normal, oscillating with an angular frequency ω_{rf}, where the subscript "rf" refers to the radio-frequency range (around 100 MHz). With the z-axis of a Cartesian coordinate system defined by the direction of $\mathbf{B}_0$, $\mathbf{B}_1$ thus exists in the x-y plane, and the net magnetic field can be written as

$$\mathbf{B} = B_1\cos(\omega_{rf}t)\mathbf{i} + B_1\sin(\omega_{rf}t)\mathbf{j} + B_0\mathbf{k}, \qquad [1.3]$$

where $\mathbf{i}$, $\mathbf{j}$, and $\mathbf{k}$ are unit vectors along the x, y, and z coordinate axes. In the case when $B_1 = 0$, the solution of equ. [1.2] yields

$$M_T(t) = M_x(t) + iM_y(t) = M_T(0)\,[\cos(\omega_0 t) + i\sin(\omega_0 t)],$$
$$M_z(t) = M_z(0) \qquad [1.4]$$

where

$$\omega_0 \equiv -\gamma B_0 \qquad [1.5]$$

is called the Larmor frequency of precession, and the subscript '*T*' on *M* refers to the transverse plane.

For the general case, when $B_1 \neq 0$, a coordinate axis transformation is useful in simplifying the results. Note that if $\omega_{rf} = \omega_0$ the applied B_1 field rotates about the *z*-axis at the same rate as M_T. Thus, in a coordinate system that also rotates about the *z*-axis at ω_0, B_1 appears stationary, as does M (in the absence of influence from B_1), and B_0 effectively becomes zero. So, the rotating frame of reference is then defined by coordinate axes aligned at the origin with the previously referred to axes (usually called the laboratory frame), but rotating about their common *z*-axis at a rate equal to ω_0. Defining ϕ as the phase angle between the rotating *x*-axis and B_1, Ω as the difference between the Larmor and rf frequencies ($\omega_0 - \omega_{rf}$), and the magnitude of B_1 in terms of frequency ($\omega_1 \equiv -\gamma B_1$), the net effective magnetic field after transforming to the rotating frame becomes

$$\boldsymbol{B} = B_x\mathbf{i} + B_y\mathbf{j} + B_z\mathbf{k}, \qquad [1.6]$$

where

$$\begin{aligned} B_x &= B_1\cos(\phi) = -(\omega_1/\gamma)\cos(\phi) \\ B_y &= B_1\sin(\phi) = -(\omega_1/\gamma)\sin(\phi) \\ B_z &= B_0 - (-\omega_{rf}/\gamma) = -\omega_0/\gamma + \omega_{rf}/\gamma = -\Omega/\gamma. \end{aligned} \qquad [1.7]$$

Then, in the rotating frame, the motion of the magnetisation vector becomes

$$\frac{d\boldsymbol{M}}{dt} = \begin{bmatrix} \dot{M}_x \\ \dot{M}_y \\ \dot{M}_z \end{bmatrix} = \begin{bmatrix} \gamma\left(B_z M_y - B_y M_z\right) \\ \gamma\left(-B_z M_x + B_x M_z\right) \\ \gamma\left(B_y M_x - B_x M_y\right) \end{bmatrix} = \begin{bmatrix} -\Omega M_y + \omega_1 \sin(\phi) M_z \\ \Omega M_x - \omega_1 \cos(\phi) M_z \\ -\omega_1 \sin(\phi) M_x + \omega_1 \cos(\phi) M_y \end{bmatrix}. \qquad [1.8]$$

Relaxation

(Bloembergen, 1948; Andrew, 1955; Slichter, 1990; Allen, 1994)

In addition to the applied magnetic fields, the nuclear magnetic moments in a sample will also respond to interaction with each other and their physical environment, which results in the phenomenon of relaxation. (In the following brief overview of relaxation, only effects resulting from the interaction between nuclear magnetic dipoles will be considered.) Given an ensemble of spins not residing in an equilibrium state (that is, the populations of the energy eigenstates do not satisfy the aforementioned Boltzmann relationship), energy will transfer from the spin system to the physical environment (called the lattice) as thermal motion, until the condition of thermal equilibrium, as stated

in equ. [1.1], is restored. This relaxation process, therefore, is called *spin-lattice* relaxation.

In the context of the quantum mechanical description of NMR, let the probability per unit time of transitions from energy eigenstate $|+\rangle$ to $|-\rangle$ be defined as W^+ and the converse as W^-. Then, at thermal equilibrium the number of transitions up (from lower to higher energy level) per unit time, $N_0^+W^+$, must equal the number of transition down, $N_0^-W^-$. Therefore, from equ. [1.1] the relative probabilities of upward and downward transitions is determined to be

$$W^+/W^- = N_0^-/N_0^+ = \exp(-\gamma\hbar B_0/kT). \qquad [1.9]$$

At any point in time the excess number of spins in the lower state is $\eta(t) = N^+(t) - N^-(t)$, and the rate of change of η as a function of time is

$$d\eta/dt = 2N^-W^- - 2N^+W^+ = 2W(\eta_0-\eta), \qquad [1.10]$$

where η_0 is η at thermal equilibrium and W is the mean of the W^- and W^+. Solving this equation yields

$$\eta = \eta_0 + C\exp(-R_1t), \qquad [1.11]$$

where C is a constant of integration and R_1 (= $2W$) is called the spin-lattice relaxation rate. The reciprocal of R_1, $T_1 = 1/R_1$, is the spin-lattice relaxation time.

In the case of water ^{1}H NMR, the important mechanism for producing transitions between $|+\rangle$ and $|-\rangle$ energy levels arises from thermally driven molecular motion (Brownian motion). At any point in space the nearby nuclear magnetic moments of rapidly moving molecules produce a randomly fluctuating magnetic field. The component of the field that exists at or near ω_0 in the spectral domain will produce energy level transitions as does the previously described applied field B_1. Additionally, energy level transitions result from the component of the field existing at or near $2\omega_0$ (for identical nuclei, or at $\omega_{0a} + \omega_{0b}$ for interaction between different nuclear species labelled *a* and *b*). This phenomenon is possible because the precessing component of a particular magnetic moment consists of both right- and left-circularly polarised components. (This fact is not evident from the above description of NMR and is not normally considered because only the left-circularly polarised component is observable.) A suitable motion at frequency $2\omega_0$, if the sense of rotation is reversed, may allow the right-circularly polarised component to interact with a neighbouring nucleus.

Clearly, as thermal equilibrium is restored, M_z approaches M_0 and, therefore, any magnetisation aligned along either the x- or y-axes must decay. This decay of transverse magnetisation, which results directly from the mechanisms of spin-lattice relaxation (i.e., fields at ω_0 and $2\omega_0$ resulting from thermal motion), is referred to as lifetime broadening. In addition, two other mechanisms contribute to the decay of transverse magnetisation, both of which involve interaction between spins, as opposed to interaction between spins and the lattice. For this reason, these mechanisms are termed spin-spin.

One spin-spin mechanism arises because the magnetic moment of each nucleus contributes to the net magnetic field over a small spatial neighborhood. Thus, at any point in space within the ensemble of spins the net magnetic field is equal to the main field, B_0, plus the contribution from nearby nuclear magnetic moments. Each spin, therefore, experiences a slightly different net magnetic field and, as a consequence of equ. [1.5], precesses at a slightly different frequency. The subsequent variation of resonance frequencies results in a progressive loss of phase coherence amongst spins within the ensemble; which is to say, a decay of transverse magnetisation. This mechanism of spin-spin relaxation is mitigated by molecular motion. More rapidly moving nuclei will experience a greater range of net magnetic fields in a given period of time, thereby tending to average out the effect of local field variations. For this reason, the term motional narrowing is applied to this spin-spin mechanism.

Transverse relaxation is also induced when two neighboring spins in opposing energy states generate energy level transitions in each other—sometimes called a 'flip-flop'. These energy exchanges may result when the precession of one spin produces a resonant rotating field at the location of another spin, and vice-versa. Each of these energy exchanges results in a loss of phase memory, thereby increasing the decay rate of phase coherence between spins

In the classical/vector description of NMR, the spin-lattice relaxation process is termed longitudinal relaxation and corresponds to the restoring of net magnetisation along the z-axis. Thence, by analogy to equ's. [1.10] and [1.11], the longitudinal relaxation of the magnetisation vector, $\boldsymbol{M}$, in the rotating frame and in the absence of B_1, is described by the relations

$$dM_z/dt = (M_0 - M_z)/T_1 \qquad [1.12]$$

and

$$M_z = [M_0 + C_z\exp(-t/T_1)], \qquad [1.13]$$

where C_z is a constant of integration. Likewise, the net loss of x- and y-magnetisation components is defined as transverse relaxation, which gives rise to an exponential decay of transverse magnetisation analogous to the exponential restoration of longitudinal magnetisation described above. Thus,

$$dM_x/dt = -M_x/T_2 \text{ and } dM_y/dt = -M_y/T_2, \quad [1.14]$$

and, likewise,

$$M_x = C_x\exp(-t/T_2) \text{ and } M_y = C_y\exp(-t/T_2), \quad [1.15]$$

where T_2 is called the transverse relaxation time. Incorporating these phenomenological descriptions of relaxation into the magnetic moment equations of motion, equ. [1.8], yields the Bloch equations:

$$\frac{dM}{dt} = \begin{bmatrix} \dot{M}_x \\ \dot{M}_y \\ \dot{M}_z \end{bmatrix} = \begin{bmatrix} -M_x/T_2 - \Omega M_y + \omega_1 \sin(\phi) M_z \\ \Omega M_x - M_y/T_2 - \omega_1 \cos(\phi) M_z \\ -\omega_1 \sin(\phi) M_x + \omega_1 \cos(\phi) M_y + (M_0 - M_z)/T_1 \end{bmatrix}. \quad [1.16]$$

Magnetisation Transfer

In addition to spin-lattice mechanisms as described above, longitudinal relaxation in tissue is generally influenced by a phenomenon known as magnetisation transfer (MT). It has been pointed out that dipolar interaction between nuclei can result in energy level transitions; however, it has not yet been pointed out that ^{1}H nuclei need not belong to water molecules to participate in dipolar interactions. In fact, water ^{1}H nuclei interact with a wide range of ^{1}H nuclei belonging to larger, less mobile molecules. Generally speaking, protons from these so-called semi-solid molecules exhibit far too rapid a transverse relaxation to be observed directly. They do, however, influence the water ^{1}H relaxation through an exchange of magnetisation—MT.

Consider a tissue sample to consist of two pools of ^{1}H nuclei: the liquid pool and the semi-solid pool (see Fig. 1.2). These two pools are labelled 'A' and 'B', respectively, each of which possesses its own unique longitudinal and transverse relaxation rates and net equilibrium magnetisation. Additionally, there are magnetisation exchange rates, R_{ab} and R_{ba}, between the liquid and semi-solid pools. Modified to account for MT as described by this simple two-pool model, the Bloch equations become (Henkelman et al., 1993)

$$\begin{bmatrix} \dot{M}_x^{a,b} \\ \dot{M}_y^{a,b} \\ \dot{M}_z^{a} \\ \dot{M}_z^{b} \end{bmatrix} =$$

$$\begin{bmatrix} -M_x^{a,b}/T_2^{a,b} - \Omega M_y^{a,b} + \omega_1 \sin(\phi) M_z^{a,b} \\ \Omega M_x^{a,b} - M_y^{a,b}/T_2^{a,b} - \omega_1 \cos(\phi) M_z^{a,b} \\ -\omega_1 \sin(\phi) M_x^{a} + \omega_1 \cos(\phi) M_y^{a} + \left(M_0^{a} - M_z^{a}\right)/T_1^{a} - R_{ab} M_z^{a} + R_{ba} M_z^{b} \\ -\omega_1 \sin(\phi) M_x^{b} + \omega_1 \cos(\phi) M_y^{b} + \left(M_0^{b} - M_z^{b}\right)/T_1^{b} - R_{ba} M_z^{b} + R_{ab} M_z^{a} \end{bmatrix} \quad [1.17]$$

This modified form of the Bloch equations implies that the relaxation mechanisms of the semi-solid pool are like those previously outlined for water, at least insofar as transverse and longitudinal relaxation being mono-exponential processes. In fact, the behaviour of the semi-solid pool is not properly described by the Bloch equations (Swanson et al., 1992; Henkelman et al., 1993; Kuwata, 1994).

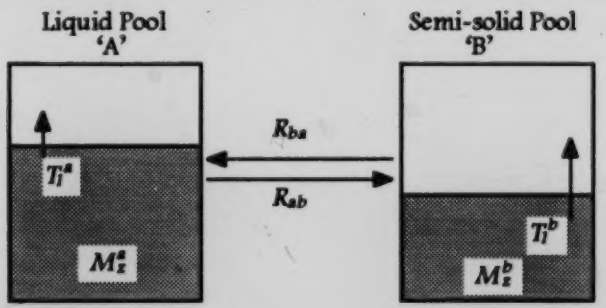

Fig. 1.2. Two-pool model of magnetisation transfer. Protons contributing to the bulk magnetisation belong to one of two groups: liquid (or mobile) and semi-solid (or motionally-restricted). The longitudinal magnetisation of each of these groups (indicated by shading) can exchange through physical or chemical means, resulting in the terms R_{ab} and R_{ba}.

Solving equ's. [1.17] at steady state allows definition of rf absorption rates. For the liquid pool as described by the Bloch equations, the steady state absorption of rf is

$$R_{rf}^{a} = \frac{\omega_1^2 T_2^{a}}{1 + \left(\Omega T_2^{a}\right)^2}, \quad [1.18]$$

which is a Lorentzian lineshape in the Ω domain. Such a lineshape, however, does not adequately describe the absorption of rf energy in the semi-solid pool. One lineshape that fits well to several tissues, including white matter, grey matter, and optic nerve is the so-called super-Lorentzian (Morrison and Henkelman, 1995), defined by

$$R_{rf}^{b} = \omega_1^2 T_2^b \sqrt{2\pi} \int_0^{\pi/2} \frac{\sin\theta}{\left|3\cos^2\theta - 1\right|} \exp\left\{-2\left[\frac{\Omega T_2^b}{\left|3\cos^2\theta - 1\right|}\right]^2\right\} d\theta. \quad [1.19]$$

The use of these constant rf absorption rates, having been arrived at from the steady state solutions, is not strictly correct during the transient response to B_1. However, in the presence of B_1, the semi-solid pool reaches steady-state (or, at least, quite close to steady-state) much more quickly than does the liquid pool, which allows the use of a constant R_{rf}^b when investigating the transient response of the *liquid* pool. Thus, the modified Bloch equations used to approximate the transient response of the liquid pool (Gounot et al., 1995) are

$$\begin{bmatrix} \dot{M}_x^a \\ \dot{M}_y^a \\ \dot{M}_z^a \\ \dot{M}_z^b \end{bmatrix} = \begin{bmatrix} -M_x^a/T_2^a - \Omega M_y^a + \omega_1 \sin(\phi) M_z^a \\ \Omega M_x^a - M_y^a/T_2^a - \omega_1 \cos(\phi) M_z^a \\ -\omega_1 \sin(\phi) M_x^a + \omega_1 \cos(\phi) M_y^a + \left(M_0^a - M_z^a\right)/T_1^a - R_{ab} M_z^a + R_{ba} M_z^b \\ \left(M_0^b - M_z^b\right)/T_1^b - \left(R_{ba} + R_{rf}^b\right) M_z^b + R_{ab} M_z^a \end{bmatrix} \quad [1.20]$$

NMR Measurement and Analysis Techniques

Signal Detection and Image Generation

Little will be said regarding the hardware and techniques involved in detecting the NMR signal and generating images, but a cursory overview is presented here for the sake of completeness.

Briefly applying B_1 will result in M rotating about the net field (as defined by equ's [1.6] and [1.7]) through some angle, normally called the tip angle. Thus, an on-resonance rf pulse with a 90° tip angle will rotate magnetisation from the z-axis through to the transverse plane. The phase angle ϕ (defined above) determines the axis in the rotating frame along which B_1 is aligned and about which M rotates if $\Omega = 0$. For example, if $\phi = 0$, B_1 is aligned along the x-axis;

and so a 90° pulse with $\phi = 0$ then is often referred to as simply a 90_x pulse, and will rotate $\boldsymbol{M}$ from the z-axis to the $-y$-axis.

Using an appropriate antenna ('coil', in the NMR vernacular) to generate a pulse, the principle of reciprocity tells us that the same coil can be used to receive a signal from the oscillating net magnetic moment, $\boldsymbol{M}$. Simply put, just as an appropriate current in the coil generates an oscillating magnetic field in the transverse(x-y) plane, so does oscillating transverse magnetisation induce an electric current in the coil. This data will not, however, contain any spatial information, which is required to generate an image.

Spatial information is encoded with the use of magnetic field gradients; that is, a magnetic field that adds to the main static magnetic field in a spatial varying manner. The standard approach is to wind three electrical coils that will generate three linear, orthogonal magnetic field gradients. Thence, each coil will change the resonant frequency linearly along one of the three Cartesian coordinate axes in the laboratory frame of reference. A number of different approaches can be taken to utilise these gradients in image generation, but the most common method, and the method relevant to the work within this thesis, is the so-called *spin warp* technique. Spin warp imaging involves three steps: slice selection, phase encoding, and read encoding, which correspond to spatial encoding in each of three orthogonal Cartesian directions.

Slice selection can be achieved by turning on one of the three gradients (call this the slice gradient) in conjunction with a $\boldsymbol{B_1}$ field. In practice, the applied $\boldsymbol{B_1}$ field does not oscillate at one infinitesimally narrow frequency, but rather over a range of frequencies, called the rf bandwidth. The gradient serves to change the resonant frequencies linearly in the slice direction, limiting excitation of nuclear spins to those in the slice containing resonant frequencies within this bandwidth. Read encoding is achieved in the converse manner. While acquiring signal, the resonant frequencies are encoded across the slice in one direction by applying a gradient (the read gradient). The acquired signal then has a finite bandwidth that linearly maps to the spatial domain in the read-gradient direction. Phase encoding is somewhat less intuitive. The phase-direction gradient is turned on for a finite period of time prior to acquisition. This gradient pulse will temporarily change the resonant frequencies of the spins in a linear manner across the phase direction, thereby imparting upon them a spatially dependent phase. Repeating the procedure of slice selection–phase encoding–read encoding many times, each time with a different amplitude phase gradient, results in a modulated signal with a linear mapping of modulation frequency to the spatial domain in the phase-gradient direction. Finally, after having collected a $K_1 \times K_2$ array of data, corresponding to K_1 phase encoding steps and K_2 samples per acquisition, a two-dimensional Fourier transform will yield an image.

Relaxometry: T_2

Although the Bloch equations tell us that transverse magnetisation decays exponentially at a rate of $1/T_2$, simply measuring the decay of M_T will not, in practice, yield an accurate estimate of T_2. Inevitable static field inhomogenieties will cause some spins to precess at different rates than others. Thus, the observed decay of M_T, called T_2^*, is much more rapid than the intrinsic transverse magnetisation of the sample. This additional loss of phase coherence can, however, be corrected for using the so-called *spin echo* pulse sequence.

Instead of acquiring signal immediately after tipping $\boldsymbol{M}$ into the transverse plane (excitation), dephasing is allowed to proceed for some duration τ, following which a 180° rf pulse is applied. This rf pulse flips all magnetic vectors in the transverse plane, thereby reversing their phase of precession in the rotating frame. After another delay of τ, the dephasing which occurred during the first delay due to the *static* field inhomogeneities is reversed and the transverse magnetisation refocusses to a peak called an echo. The time 2τ is thus called the echo time (TE). Diffusion of spins during the delay τ may cause them to experience a different static field during the rephasing period as compared to the dephasing period, resulting in incomplete refocussing. As long as the delay τ is sufficiently brief, the effect of diffusion is negligible and the echo magnitude is reduced solely due to the sample's intrinsic T_2. Transverse magnetisation can be repeatedly refocussed to form many echoes (called the Carr-Purcell (CP) or, with a slight modification, the Carr-Purcell-Meiboom-Gill (CPMG) pulse sequence (Carr and Purcell, 1954; Meiboom and Gill, 1958)). The amplitudes of these echoes can then be fitted to an exponential decay,

$$M_T(nTE) = M_T(2n\tau) = M_0\exp(-2n\tau/T_2), \qquad [1.21]$$

where n is the echo number and $TE = 2\tau$ is called the echo time, to estimate T_2.

Although the dephasing due to $\boldsymbol{B_0}$ inhomogeneities can be corrected using a spin-echo approach, $\boldsymbol{B_0}$ and $\boldsymbol{B_1}$ inhomogenieties preclude the possibility of perfect refocussing pulses; and, imperfectly refocussed magnetisation severely corrupts echo magnitudes, resulting in erroneous T_2 estimates. Because rf coils never generate perfectly homogeneous $\boldsymbol{B_1}$ fields, an rf pulse will not equally rotate all magnetic moments within the sample. $\boldsymbol{B_0}$ inhomogeniety results in an effective magnetic field in the rotating frame (given by equ's [1.6] and [1.7]), about which $\boldsymbol{M}$ rotates, containing a finite z-component (as given by Ω in equ. [1.7]). Consequently, a true 180° pulse is not possible. This problem is relatively minor when performing *in vitro* measurements. In such cases, the amplitude of $\boldsymbol{B_1}$ is usually much larger than Ω, making the z-component negligible. For example, in-vitro T_2 measurements referred to in this thesis use $\gamma B_1/2\pi = 25$ kHz, compared with $\Omega/2\pi$ magnitudes of approximately 50 Hz or less.

However, when imaging, B_1 magnitudes are usually in the range 100 Hz to 1 kHz, making the typical z-component of the effective field a significant factor.

Imperfectly refocussed magnetisation must be removed from the acquired data if accurate T_2 estimates are to be generated. There are two basic approaches to removing unwanted magnetisation present in a multi-echo pulse sequence: phase-cycling and gradient spoiling. Phase cycling involves repetition of a pulse sequence with altered rf pulse phases. The appropriate algebraic combination of the acquired signals results in cancellation of some or all of the erroneous magnetisation components. The simplest example of phase cycling is to alternate the excitation pulse phase by 180° in alternate scans, which will cancel a constant (DC) contribution to the echoes. Although phase cycles have been devised to compensate for imperfect refocussing in multi-echo sequences, completely eliminating erroneous signal requires a great many scans, limiting their practicality when imaging (Zur and Stokar, 1987; Barker and Mareci, 1989). Instead of using phase cycling to cancel unwanted magnetisation components, a method more suited to imaging is the use of spoiler gradients. By surrounding an rf refocussing pulse with two identical gradient pulses, only the transverse magnetisation that experiences a genuine 180° rotation will be rephased by the second gradient; all other magnetisation will remain dephased and, therefore, not contribute to the echo (Madjumar et al., 1986; Crawley and Henkelman 1987; Barker and Mareci, 1989; Poon and Henkelman, 1992). When spoilers are implemented in a multi-echo pulse sequence, the strengths and/or direction of each pair of spoilers must be adjusted such that magnetisation dephased by one gradient is not undesirably rephased by another. This practice is discussed in more detail in Chapter 5.

Although spoiler gradients can effectively remove erroneous magnetisation, the observed T_2 from a multi-echo sequence will be an underestimate of the true T_2 value due to repeated dephasing of improperly refocussed magnetisation. However, further improvement in T_2 measurements can be achieved by minimising the refocussing pulse imperfections. Altering the rf pulse phases within a given pulse sequence can be used to reduce the effect of B_0 and B_1 inhomogeniety—the Meiboom-Gill modification to the CP sequence being the most famous example—but such approaches are nullified by the application of spoiler gradients. An option that can be incorporated into an imaging protocol that includes spoiler gradients is the use of composite refocussing pulses. An example of a composite refocussing pulse is 90_x-180_y-90_x (Levitt and Freeman, 1981), which refers to the concatenation of three rf pulses. Imagining the 180_y component of this pulse to be perfect, it will compensate for the 90_x components being too strong or weak. A more elaborate composite (named the 'Version-S' pulse), designed to compensate for a prescribed range of B_0 and B_1 inhomogeniety (Poon and Henkelman, 1993), is used in the multi-echo imaging discussed in Chapters 2 and 3. The drawbacks to using composite

pulses are the increased rf power deposition into the tissue and the increased time that may be required to implement the pulse. For example, the Version-S pulse requires 5.4 times the energy of a simple 180 pulse and, consequently, is 5.4 times longer for a given power setting. Subsequent composite pulse designs have reduced this energy requirement by approximately a factor of 2 while maintaining similar refocussing qualities (Poon and Henkelman, 1995).

Given a collection of echoes, processing this data into a T_2 estimate is not always a straightforward problem. In the simplest scenario, the transverse relaxation of a sample is mono-exponential, making the fitting process trivial. However, as indicated later in this chapter, nervous tissue (among other types) does not exhibit a mono-exponential transverse relaxation, making equ. [1.21] inappropriate for estimating T_2. Instead, the multi-echo data must be fitted to more than one T_2 component. Without explicit knowledge of the number of components present in a sample, the preferred option is to fit the data in an non-negative least squares (NNLS) manner to a wide range of many T_2 components (Whittall and MacKay, 1989; Whittall et al., 1991). The result of this fit has been termed the T_2 spectrum and is given by the NNLS solution of

$$\boldsymbol{y} = \boldsymbol{A}\boldsymbol{S} \qquad [1.22]$$

for $\boldsymbol{S}$, where $\boldsymbol{y}$ is an N-element column vector of the measured echo amplitudes and $\boldsymbol{A}$ is the $N \times K$ element matrix of all possible exponential terms for the echo times and range of T_2s to which $\boldsymbol{y}$ is fitted:

$$\boldsymbol{A} = \exp\left(\begin{bmatrix} (-t_0/T_0) & (-t_0/T_1) & \cdots & (-t_0/T_K) \\ (-t_1/T_0) & \ddots & & (-t_1/T_K) \\ \vdots & & \ddots & \vdots \\ (-t_N/T_0) & (-t_N/T_1) & \cdots & (-t_N/T_K) \end{bmatrix}\right). \qquad [1.23]$$

(N.B., the above exponential function applies to each matrix element independently.) Due to the unavoidable contribution of noise to the data, an infinite variety of T_2 spectra, $\boldsymbol{S}$, can be adequately fitted, in a statistical sense, to a particular vector of multi-echo data, $\boldsymbol{y}$. For this reason, a constraint is required to ensure convergence of this fitting to a unique solution. While any spectral smoothing constraint would suffice, a minimum energy constraint is employed in the work within this thesis due to ease of implementation. Algebraically, the problem is again formulated as equ. [1.22], with the minimum energy constraint incorporated into an $(N+K) \times K$ $\boldsymbol{A}$ matrix as a $K \times K$ diagonal sub-matrix of terms λ:

$$A = \exp\left(\begin{bmatrix} (-t_0/T_0) & (-t_0/T_1) & \cdots & (-t_0/T_K) \\ (-t_1/T_0) & \ddots & & (-t_1/T_K) \\ \vdots & & \ddots & \vdots \\ (-t_N/T_0) & (-t_N/T_1) & \cdots & (-t_N/T_K) \\ \lambda & 0 & \cdots & 0 \\ 0 & \lambda & \ddots & \vdots \\ \vdots & \ddots & \ddots & 0 \\ 0 & \cdots & 0 & \lambda \end{bmatrix}\right) \qquad [1.24]$$

(Whittall and MacKay, 1989; Whittall et al., 1991). The raw data vector, $\mathbf{y}$, is then padded with zeroes to the appropriate dimension of $(N+K)\times 1$. The scalar λ must be adjusted iteratively until the fit is statistically satisfactory, a condition determined by the χ^2 statistic. An ideal fit should have $\chi^2 \approx N$, but a more conservative approach is to adjust λ until $\chi^2 \approx N + \sqrt{2N}$ or slightly larger to avoid spurious elements in $\mathbf{S}$ due to the noise. When signal-to-noise is relatively low, as may be the case when imaging, simulation studies have found that smoothing constraints are not effective in improving fit quality (Graham et al., 1996).

Relaxometry: T_1

Longitudinal relaxation measurements are significantly less sensitive to rf pulse imperfections. *In vitro*, the inversion-recovery (IR) or saturation-recovery (SR) pulse sequence may be used to measure T_1. The IR sequence works as follows. The net magnetisation is inverted to align with the negative z-axis using an 180° rf pulse. Following inversion, the magnetisation is allowed to relax back toward thermal equilibrium for a period of time, τ, after which a 90° pulse is used to rotate the longitudinal magnetisation into the transverse plane where its amplitude is measured with the rf coil. This procedure is repeated using various relaxation delays, and the resulting collection of magnetisation amplitudes fit to an exponential function recovering from $-M_0$ to $+M_0$ at a rate R_1. The SR procedure uses essentially the same approach except that instead of initially inverting the magnetisation it is saturated (i.e., altered to a state of no net magnetisation). The simplest approach to saturation is to eliminate longitudinal magnetisation with a 90° pulse, then employ phase-cycling techniques to cancel the remaining transverse relaxation. Any remaining longitudinal magnetisation is accounted for in fitting the data to

$$M_z(\tau) = M_0[1-\beta\exp(-\tau/T_1)], \qquad [1.25]$$

where β varies from unity if the initial 90° pulse does not eliminate M_z.

The T_1 measurements of nerve water ^1H discussed in Chapter 4 use the SR approach in combination with a CPMG sequence. This combination provides two-dimensional data which can be fit to a combination of T_1 and T_2 components. Fitting this data is done in two manners, neither of which are without short-comings. Direct non-negative least-squares (NNLS) fitting of the two-dimensional data (English et al., 1991) is one approach; however, it is limited by computational practicality. The equation to be solved is of the form of equ. [1.25], but the dimension of the $\boldsymbol{A}$ matrix becomes $(N_1N_2)\times(K_1K_2)$, where N_1 and N_2 are the number of echoes and SR delays respectively, and K_1 and K_2 are the number of T_2 and T_1 components to which the data is fit. With the addition of a minimum energy constraint, this matrix grows to a dimension $(N_1N_2+K_1K_2)\times(K_1K_2)$, which is likely far too large for practical implementation. This computational limit is avoided by processing the multi-echo for each SR delay independently, followed by segmenting the resulting T_2 spectra into some number of domains, from each of which an SR curve is extracted and fit to a range of T_1 values. This approach has the disadvantage of requiring user intervention, which may distort results; conversely, it has the advantage of allowing large N and K values and a spectra smoothing constraint, which may prevent some distorted results. Each approach having its own strengths and weaknesses, they may be used cooperatively, where spurious results from one method not resulting from the other are discarded.

Magnetisation Transfer

Normally, the effects of exchange between water and macromolecules are ignored. The longitudinal relaxation rate observed for water is known to be affected by MT, but it is not considered further, and the simple Bloch equations, equ. [1.16], are used to describe the magnetisation. However, this extra pathway of longitudinal relaxation can significantly affect observed magnetisation when the semi-solid pool magnetisation is excited differently from that of the liquid pool.

As pointed out previously, the semi-solid pool transverse relaxation is extremely rapid compared to that of the liquid pool. This is equivalent to saying that the absorption line width of semi-solid ^1H is much larger than that of liquid ^1H, as can be deduced from line shapes in equ's [1.18] and [1.19]. Thus, a $\boldsymbol{B}_1$ field applied far off resonance (i.e., a large Ω) will have much more of an effect on the semi-solid pool than on the liquid pool. The general approach then to quantifying the MT effect is to apply a $\boldsymbol{B}_1$ field several kHz off resonance which is assumed to have negligible affect on $\boldsymbol{M}^a$. Adopting a simplified view that ignores the R_{ab} term in equ. [1.17], this $\boldsymbol{B}_1$ field will rapidly saturate $\boldsymbol{M}^b$. Applying this $\boldsymbol{B}_1$ continuously for some period of time (typically, several seconds) will maintain $M_z^b = 0$ while reducing M_z^a to a new steady state value by means of the exchange term $R_{ab}M_z^a$ in equ [1.17]. The steady state solution to equ. [1.17] is then easily found to be

$$M_z^a = M_0^a / (1 + T_1^a R_{ab}). \qquad [1.26]$$

This simplified solution, however, is not accurate because assumptions that M^a is unaffected by B_1 and that $M_z^b = 0$ are not valid. The determination of exchange rate parameters is, in fact, much more complicated, requiring knowledge of the semi-solid pool lineshape and acquisition of many M_z^a values following applications of B_1 with various amplitudes and off-resonance frequencies (Henkelman et al., 1993).

In addition to the traditional steady-state measurements, MT characteristics can also be investigated during the transient period when the liquid and semi-solid pools are equilibrating via exchange terms R_{ab} and R_{ba}. This approach simply requires that the off-resonance B_1 pulse is terminated prior to the liquid pool reaching steady state. Repeating the measurement with various B_1 durations renders the transient behaviour M_z^a. This data can then be fit to equ. [1.20], yielding estimates of liquid–semi-solid exchange rates. Measuring this transient response is of particular value when investigating multi-compartment tissues such as nerve, because data can be acquired prior to the time when water exchange between the anatomical compartments can significantly influence the results. Such investigations of nerve, which are discussed further in Chapter 4, combine transient MT measurements with T_2 spectral decomposition (MT-CPMG) (Harrison et al., 1995), analogously to the combined T_1-T_2 measurements made from the SR-CPMG sequence.

Simulation of Multi-Echo MRI

Analysing multiple-pulse sequences becomes exceedingly complex when the assumption of ideal rf pulses is removed and a large number of pulses are involved. Analytical solutions become entirely impractical, making numerical solutions the only option. Computer simulations are particularly valuable when analysing multi-echo pulse sequences, where relatively small rf pulse imperfections translate into significant errors in T_2 estimates when the number of echoes becomes large. The obvious approach to simulating an NMR pulse sequence is to solve the Bloch equations directly. These solutions can be used to predict M at any point in a pulse sequence, but this approach does not provide details relating particular rf or gradient pulses from a complex pulse sequence to M at any point in time. However, it is possible to decompose the net magnetisation into the sum of unique components each of which represents a different pathways of magnetisation states (Woessner, 1961; Kaiser et al., 1974; Barker and Mareci, 1989; Simbrunner, 1994).

The density matrix (see Slichter, 1990; or Mateescu and Valeriu, 1993) of a single spin-1/2 system, which we consider accurate for water ^{1}H NMR, is 2×2 in dimension. There are two single-quantum coherence elements, labelled −1

and +1 (referring to their coherence levels), corresponding to clockwise and counter-clockwise rotating transverse magnetisation. (N.B., these labels are opposite to the standard definitions, but agree with the formalism of Simbrunner (Simbrunner, 1994), which is used in this thesis). The other two matrix elements correspond to longitudinal magnetisation and are labelled 0. (For the sake of brevity, a description of density matrix formalism has been omitted from thesis, as it is not necessary to understanding the bulk of the work herein. Suffice it to say that the complete information about the status of an ensemble of spins at a given time is given by the density matrix).

Assuming that a pulse sequence begins at thermal equilibrium, all magnetisation at any point in time within the sequence can be identified by the pathway of coherence levels it has experienced since thermal equilibrium. This pathway can, therefore, be described by a vector, $\boldsymbol{p} = (p_n, p_{n-1}, p_{n-2}, \ldots, p_1, p_0)$, where p_n refers to the coherence level following the nth pulse. At thermal equilibrium, all magnetisation is longitudinal, so p_0 is always zero and, consequently, usually dropped from the formalism altogether. Furthermore, if one is only interested in the coherence pathways of magnetisation that contribute to the observed signal, p_n can be constrained to 1, making $\boldsymbol{p} = (1, p_{n-1}, p_{n-2}, \ldots, p_1)$. In the case of multi-echo sequences with linear and evenly spaced echo times, p_1 must be ± 1 for magnetisation described by $\boldsymbol{p}$ to form an echo at the echo times. Figure 1.3 shows the tree of pathways that results from a multi-pulse sequence.

Given a particular coherence pathway vector, $\boldsymbol{p}_i$, the transverse magnetisation resulting from this pathway and contributing to the nth echo is given by (Simbrunner, 1994)

$$M_T(t_n) = M_0 f_n(1, p_{n-1}) f_{n-1}(p_{n-1}, p_{n-2}) \cdots f_1(p_1, 0) \times \exp\left(-i\psi - TE/(2T_2)\right)\varepsilon_1^{1/2} \prod_{i=2}^{n-1} \varepsilon_i \quad , \qquad [1.27]$$

where

$$\psi = \rho_n(TE/2) + p_{n-1}\rho_{n-1}(TE) + \cdots + p_1\rho_1(TE/2), \qquad [1.28]$$

and

$$\varepsilon_i = \exp\left(-|p_i|TE/T_2\right)\exp\left\{\left(|p_i|-1\right)TE/T_1\right\}. \qquad [1.29]$$

The ρ terms in equ. [1.28] are time-dependent phase terms which result from B_0 inhomogenieties or gradients pulses. The f_n terms are pulse-related scalars that factor in the amount of magnetisation that transfers from one coherence level to another following a particular rf pulse. For example, $f_j(p_j, p_{j-1})$ is the

fraction of magnetisation with coherence level p_{j-1} that is transferred to coherence level p_j by the jth rf pulse. These factors can be determined from elements of a rotation matrix as:

$$\begin{gathered} f_j(1,1) = (r_{11} + r_{22})/2 + i\cdot(r_{21} - r_{12})/2, \\ f_j(-1,-1) = f_j(1,1), \\ f_j(1,-1) = (r_{11} - r_{22})/2 + i\cdot(r_{21} + r_{12})/2, \\ f_j(-1,1) = f_j(1,-1), \\ f_j(1,0) = r_{12} + i\cdot r_{23},\ f_j(-1,0) = f_j(1,0), \\ f_j(0,1) = (r_{31} - i\cdot r_{32})/2,\ f_j(0,-1) = f_j(0,1), \\ f_j(0,0) = r_{33}, \end{gathered} \qquad [1.30]$$

where r_{lm} are the elements of the rotation matrix determined by the rf pulse characteristics. Given a net B field with a phase angle φ and elevated from the transverse plane by angle α, a rotation about this vector by angle θ is given by the rotation matrix,

$$R = R_z(-\phi)R_y(\alpha)R_x(\theta)R_y(-\alpha)R_z(\phi), \qquad [1.31]$$

where $R_z(\varphi)$, $R_y(\alpha)$, and $R_x(\theta)$ are standard rotation matrices about Cartesian axes (Gonzalez and Woods, 1993).

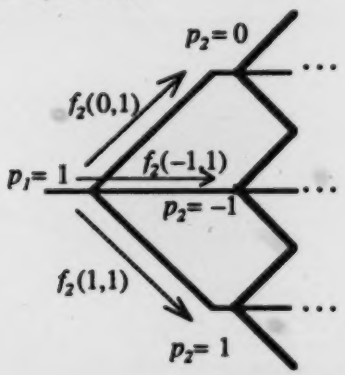

Fig. 1.3. A tree representing the possible coherence pathways of a multi-pulse sequence. The fraction of magnetisation that is transferred from one coherence level to another is represented by the scalar $f_n(p_n, p_{n-1})$, which is determined from the rf pulse characteristics.

Equipped with the tools of equ's [1.27] through [1.31], the transverse magnetisation resulting from every pathway contributing to a particular echo can be computed. Assuming an inhomogeneous B_0, which is particularly relevant when using a read gradient, only pathways that will form an echo at $t = nTE$ need be considered. For the eighth echo there are 750 such pathways that may contribute, and these pathways can be grouped into three categories:

true-T_2, T_1-artefact, and phase-artefact (assuming the case of spin-warp imaging) (Crawley and Henkelman, 1987). The true-T_2 pathways contain only coherence levels of ± 1, making all relaxation due solely to T_2. T_1-artefact pathways contain some number of $p_j = 0$ terms, which results in intervals during which the magnetisation is relaxing with a time constant of T_1 instead of T_2. Phase-artefact pathways also contain $p_j = 0$ terms, but, in the case of spin-warp imaging, they do not contribute directly to the echo. The act of phase encoding requires that the number of phase reversals throughout the multi-echo pathway be of the same parity as the echo number, otherwise reconstruction will result in signal being mapped to an inverted image location.

Contributions from the true-T_2 and the T_1-artefact pathways add together to generate the primary image, while the signal from the phase-artefact pathway generates the so-called ghost image. If there are phase artefacts, without a priori knowledge of the sample at both a given point in space, (x_o, y_o), and at the ghost image location, $(x_o, -y_o)$, the observed signal from that point in space cannot be predicted. For coping with this in computer simulation, the observed signal (M_{OBS}) is defined as the sum of magnetisation from true-T_2 (M_{T2}) and the T_1-artefact (M_{T1}) pathways, and the phase artefact signal (M_P) is tabulated independently as an estimate of the potential ghost image contribution to the observed signal at a given point in space.

The limiting factor in implementing coherence pathway simulations is the computational requirements. The number of pathways grows exponentially with the number of rf pulses in a pulse sequence, so simulating multi-echo sequences with 16 or more echoes becomes computationally impractical. In these cases, simulations based directly on the Bloch equations, which only yield observed magnetisation, must be used. In Chapter 5, where multi-echo pulse sequence modifications are investigated using computer simulation, both coherence pathway and bulk simulations are employed.

NMR Properties of Peripheral Nerve

Transverse Relaxation of Peripheral Nerve Water

A simple, homogeneous saline solution exhibits mono-exponential transverse relaxation; however, the T_2 of many tissues—particularly nervous tissues—has been found to be distinctly multi-exponential (Vasilescu et al., 1978; Fenrich and Allen, 1991; Menon et al., 1992; Fenrich, 1992; Kreis et al., 1992; Stewart et al., 1993; Rutt and Mitchell, 1993; MacKay et al., 1994; Whittall et al., 1997), resulting in a distribution of T_2 times referred to as the T_2 spectrum. The origin of multi-exponential relaxation in tissue has and continues to be investigated (Belton and Ratcliffe, 1985; Fenrich, 1992; Menon et al., 1992; Bronskill et al., 1994). In nerve tissue, the evidence strongly indicates that multi-exponential relaxation results, at least partially, from a variety of unique, anatomically separated water environments. Normal animal peripheral

nerve T_2 has been decomposed into at least three broad ranges of exponential relaxation rates (Vasilescu et al., 1978; Fenrich and Allen, 1991; Menon et al., 1992), and the respective signal fractions of these three signal components have been correlated to the estimated water content of myelinic, axonal, and inter-axonal (connective tissue) water domains (Menon et al., 1992; Fenrich, 1992). The shortest-lived fraction of the signal is believed to result from myelin water because this rapidly relaxing signal is absent in nonmyelinated nerve (Fenrich and Allen, 1991; Fenrich, 1992), gray matter (Kreis et al., 1992; Rutt and Mitchell, 1993; MacKay et al., 1994; Whittall et al., 1997), and multiple sclerosis plaques (Rutt and Mitchell, 1993; MacKay et al., 1994). The assignment of the two longer-lived components is not as clear, although micro-images of crayfish nerve cord suggests that axonal water is faster relaxing than connective tissue water (Menon et al., 1992), thus suggesting that the intermediate T_2 component arises from the axonal water while the longest-lived component is derived from the inter-axonal water.

If indeed multi-exponential relaxation results from anatomic compartmentalisation of the nerve water, then changes in nerve microanatomy should be reflected in the T_2 spectrum. Hence, with respect to peripheral nerve injury, changes in multi-exponential T_2 relaxation may identify the loss (and regrowth) of axons and myelin. A number of studies report Wallerian degeneration, both in the central (Terae et al., 1993; Pennock et al., 1993; Waragai et al., 1994) and in the peripheral (Jolesz et al. 1984; Titelbaum et al., 1989) nervous systems, to appear hyperintense on T_2-weighted images—indicating a general increase in transverse relaxation time. Multi-exponential T_2 spectra have been shown, *in vitro*, to change due to experimental allergic encephalomyelitis (Stewart et al., 1993), an observation that supports the assignment of the short-lived component to myelin which breaks down and is removed during degeneration.

Studies have shown that, given sufficient spatial resolution, peripheral nerve can be distinguished from adjoining tissue in T_2-weighted images (Howe et al., 1992; Filler et al., 1993; Enochs et al. 1994). However, traditional T_2 measurements derived from images are usually unable to identify multiple components because either too few echoes are formed or a significant portion of the magnetisation is lost or distorted by repeated imperfect refocussing pulses. This distortion of T_2 relaxation rates may have contributed to little or no nerve-muscle contrast in T_2-weighted images of normal nerve (Fahr and Sauser, 1988; Howe et al., 1992; Enochs, 1994). Proper estimation of the T_2 spectrum of a tissue by imaging requires a multi-echo pulse sequence capable of yielding a sufficient number of uncorrupted echoes (Poon and Henkelman, 1993). Using such imaging pulse sequences, multiple T_2 components have been identified in white matter (Rutt et al., 1993; Oatridge et al., 1993; MacKay et al., 1994; Whittall et al., 1997). Investigation of multiple T_2 in normal and

injured peripheral nerve using in-vitro and imaging techniques is discussed in Chapters 2 and 3.

Magnetisation Transfer in Peripheral Nerve

Given the supposition that multi-exponential transverse relaxation of nerve water is due to anatomic compartmentalisation, it may be that MT characteristics of nerve water exhibit multiple unique components.

Magnetisation transfer has been widely investigated as a contrast mechanism in neuroimaging, particularly, but not exclusively, as a means of identifying and characterising multiple sclerosis (MS) lesions. Reduction of magnetisation transfer contrast (*MTC*) (one minus the ratio of longitudinal magnetisation at steady-state with and without semi-solid pool saturation) has been found to be greater in demyelinating MS lesions than oedemous experimental allergic encephalomyelitis (EAE) ones (Dousset et al., 1992), and *MTC* reduction has been correlated with the appearance of spectroscopic peaks believed to result from myelin breakdown (Hiele et al. 1994). From these results and others (Lexa et al. 1994; Loevner et al., 1995; Mehta et al., 1996), it has been suggested that *MTC* decreases are primarly due to the loss of myelin and even that it may serve as a relatively specific indicator of demyelination (Hiele et al., 1994; Loevner et al., 1995). However, it was shown that some myelinated and non-myelinated nerves to have similar *MTC*s (Beaulieu and Allen, 1994) and that similar steady-state MT characteristics are exhibited by both white matter and grey matter (Morrison and Henkelman, 1995). These studies indicate that the sources of *MTC* in nerve are not restricted to myelin. Thus, the specific contributions of different anatomic compartments of nerve to its bulk *MTC* are not clear.

One investigation, which attempted to correlate the T_2 components of white matter with their respective *MTC*s found both components to exhibit similar *MTC*s over a wide range of off resonance frequencies. The conclusion drawn was that water mixing between the two anatomic compartments must be rapid enough to result in an effectively singular anatomic compartment over the time course of an MT measurement (several seconds) (Harrison et al., 1995).

Steady-state and transient MT-CPMG investigations discussed in Chapter 4 attempt to clarify the reasoning behind the apparent similarity between myelinic and axonal MT.

References

Allen P. S., 1994. Class notes, ASM 579.

Andrew, 1955. *Nuclear Magnetic Resonance*, Cambridge University Press, Cambridge.

Barker G J, Mareci T H, 1989. Suppression of artefacts in multiple-echo magnetic resonance. *J. Magn. Reson.* 83, 11.

Beaulieu C, Allen P S, 1994. Some magnetisation transfer properties of water in myelinated and nonmyelinated nerves. *Proc. of the SMR. 2nd Annual Meeting*, p. 169.

Belton P S, Ratcliffe R G, 1985. NMR and compartmentation in biological tissues. *Prog. NMR Spec.* 17:241.

Bloch F, Hansen W W, Packard M E, 1946. Nuclear induction. *Phys. Rev.* 69:127.

Bloembergen N, Purcell E M, Pound R V, 1948. Relaxation effects in nuclear magnetic resonance absorption. *Phys. Rev.* 73:679.

Bronskill M J, Santyr G E, Walters B, Henkelman R M, 1994. Analysis of discrete T_2 components of NMR relaxation for aqueous solutions in hollow fibre capillaries. *Magn. Reson. Med.* 31, 611.

Carr H Y, Purcell E M, 1954. Effects of diffusion on free precession in nuclear magnetic resonance experiments. *Phys. Rev.* 94:630.

Chaudhry V, Glass J D, Griffin J W, 1992. Wallerian degeneration in peripheral nerve disease. *Neurologic Clinics* 10:613.

Crawley A P, Henkelman R M, 1987. Errors in T_2 estimation using multislice multiple-echo imaging. *Magn. Reson. Med.* 4:34.

Dousset V, Grossman R J, Ramer K N, Schnall M D, Young L H, Gonzalez-Scarano F, Lavi E, Cohen J A, 1992. Experimental allergic encephalomyelitis and multiple sclerosis: lesion characterisation with magnetisation transfer imaging. *Radiology* 182:483.

Dyck P J, 1975. "Pathological alterations of the peripheral nervous system of man", in *Peripheral Neuropathy* (P. J. Dyck, P. K. Thomas, E. H. Lambert Eds.) pp. 296-336, Saunders, Philadelphia.

English A E, Whittall K P, Joy M L G, Henkelman R M, 1991. Quantitative two-dimension time correlation relaxometry. *Magn. Reson. Med.* 22:425.

Enochs W S, Shaffer B, Bhide P G, et al. 1993. MR imaging of slow axonal transport *in vivo*. *Exp. Neurol.* 123:235.

Enochs W S, 1994. MR imaging of the peripheral nervous system. *J. Magn. Reson. Imag.* 4:251.

Fahr L M, Sauser D D, 1988. Imaging of peripheral nerve lesions. *Orthop. Clin. North Amer.* 19:27.

Fenrich F R E, Allen P S, 1991. Transverse relaxation rate distributions for water protons in myelinated and unmyelinated nerves. *Proc. of SMRM. 10th Annual Meeting.* p. 693.

Fenrich F R E, 1992. *A simulation and experimental study of water proton relaxation in a white matter model.* M.Sc. Thesis, University of Alberta.

Filler A G, Howe F A, Hayes C E, Kliot M, Winn H R, Bell B A, Griffiths J R, Tsuruda J S, 1993. Magnetic resonance neurography. *Lancet* 341:659.

Filler A G, 1994. Axonal transport and MR imaging: prospects for contrast agent development. *J. Magn. Reson. Imag.* 4:259.

Frykman G K, McMillan P J, Yegge S, 1988. A review of experimental methods of measuring peripheral nerve regeneration in animals. *Orthopedic Clinics of North America* 19:209.

Gonzalez R C, Woods R C, 1992. *Digital Image Processing.* Addison-Wesley, Reading, Mass.

Gounot D, Mauss Y, Chambron J, 1995. Magnetisation Transfer Kinetics. *Proc. of the SMR. Third Scientific Meeting.* p. 1029.

Graham S J, Stanchev P L, Bonskill M J, 1996. Criteria for analysis of multicompartment tissue T_2 relaxation data. *Magn. Reson. Med.* 35:370.

Hahn E L, 1950. Spin Echoes. *Phys. Rev.* 80:580.

Harrison R, Bronskill M J, Henkelman R M, 1995. Magnetisation transfer and T_2 relaxation components in tissue. *Magn. Reson. Med.* 33:490.

Henkelman R M, Huang X, Xiang Q-S, Stanisz G J, Swanson S D, Bronskill M J, 1993. Quantitative interpretation of magnetisation transfer. *Magn. Reson. Med.* 29:759.

Howe F A, Filler A G, Bell B A, Griffiths J R, 1992. Magnetic resonance neurography. *Magn. Reson. Med.* 28:328.

Jolesz F A, Polak J F, Ruenzel P W, Adams D F, 1984. Wallerian degeneration demonstrated by magnetic resonance: spectroscopic measurements on peripheral nerve. *Radiology* 152:85.

Kaiser R, Bartholdi E, Ernst R R, 1974. Diffusion and field-gradient effects in NMR Fourier spectroscopy. *J. Chem. Phys.* 60:2966.

Kreis R, Fusch C, Boesch C, 1992. *In vivo* characterisation of three water compartments in human white matter using a single voxel technique with short TE. *Proc. of the SMRM. 11th Annual Meeting* p. 1963.

Kuwata K, Brooks D, Yang H, Schleich T, 1994. Relaxation-matrix formalism for rotating frame spin-lattice proton NMR relaxation in the presence of an off-resonance irradiation field. J. Magn. Reson. *J. Magn. Reson. B* 104:11.

Lauterbur P C, 1973. Image formation by induced local interactions: examples employing nuclear magnetic resonance. *Nature* 242:190.

Levitt M H, Freeman R, 1981. Compensation for pulse imperfections in NMR spin-echo experiments. *J. Magn. Reson.* 43:65.

Lexa F J, Grossman R I, Rosenquist A C, 1994. MR of Wallerian degeneration in the feline visual system: characterisation by magnetisation transfer rate with histopathologic correlation. *AJNR* 15:201.

Mateescu G D, Valeriu A, 1993. *2D NMR Density Matrix and Product Operator Treatment.* Prentice-Hall, Englewood Cliffs, NJ.

MacKay A, Whittall K, Adler J, Li D, Paty D, Graeb D, 1994. *In vivo* visualization of myelin water in brain by magnetic resonance. *Magn. Reson. Med.* 31, 673.

Madjumar S, Orphanoudakis S C, Gmitro A, O'Donnell M, Gore J C, 1986. Errors in the measurement of T_2 using multiple-echo MRI techniques. I. Effects of radiofrequency pulse imperfection. *Magn. Reson. Med.* 3:397.

Meiboom S, Gill D, 1958. Modified spin-echo method for measuring nuclear relaxation time. *Rev. Sci. Instrum.* 29:688.

Menon R S, Rusinko M S, Allen P S, 1992. Proton relaxation studies of water compartmentalisation in a model neurological system. *Magn. Reson. Med.* 28, 264.

Morrison C, Henkelman R M, 1995. A model for magnetisation transfer in tissues. *Magn. Reson. Med.* 33:475.

Oatridge A, Hajnal J V, Kasuboski L, Young I R, Bydder G M, 1993. Measurement of long T_2 components in normal brain tissue. *Proc. of the SMRM. 12th Annual Meeting.* p. 348.

Parry G J, 1992. Electrodiagnostic Studies in the evaluation of peripheral nerve and brachial plexus injuries. *Neurologic Clinics* 10:921.

Pennock J M, Rutherford M A, Cowan F M, Bydder G M, 1993. MRI: early onset of changes in Wallerian degeneration. *Clin. Rad.* 47:311.

Poon C S, Henkelman R M, 1992. Practical T_2 quantitation for clinical applications. *J. Magn. Reson. Imag.* 2:541.

Poon C S, Henkelman R M, 1993. 180° refocussing pulses which are insensitive to static and radiofrequency field inhomogeneity. *J. Magn. Reson.* 99:45.

Poon C S, Henkelman R M, 1995. Robust Refocussing Pulses of Limited Power. *J. Magn. Reson.* 116:161.

Purcell E M, Torrey H C, Pound R V, 1946. Resonance absorption by nuclear magnetic moments in a solid. *Phys. Rev.* 69:37.

Rutt B K, Mitchell J D, 1993. Myelin-selective imaging with 3D fast spin echo MRI. *Proc. of the SMRM. 12th Annual Meeting.* p. 137.

Schröder J M, 1975. Degeneration and regeneration of myelinated nerve fibres in experimental neuropathies, *in* "Peripheral Neuropathy" (P. J. Dyck, P. K. Thomas, E. H. Lambert Eds.) pp. 337-362, Saunders, Philadelphia.

Simbrunner J, 1994. Generalization of the partition method for calculating echo magnitudes. *J. Magn. Reson. A.* 109:117.

Slichter C P, 1990. *Principles of Magnetic Resonance*, Springer-Verlag, Berlin.

Stewart W A, MacKay A L, Whittall K P, Moore G G, W, Paty D W, 1993. Spin-spin relaxation in experimental allergic encephalomyelitis. Analysis of CPMG data using a non-linear least squares method and linear inverse theory. *Magn. Reson. Med.* 29, 767.

Sunderland S, 1991. *Nerve Injuries and their Repairs*, Churchill Livingstone, Edinburgh.

Swanson S D, 1992. *Proceedings of SMRM, 11th Annual Meeting*, p. 255.

Terae S, Taneichi H, Abumi K, 1993. MRI of Wallerian degeneration of the injured spinal cord. *J. Comp. Asst. Tomog.* 17:700.

Titelbaum D S, Frazier J L, Grossman R I, Joseph P M, Yu L T, Kassab E A, Hickey W F, LaRossa D, Brown M J, 1989. Wallerian degeneration and inflammation in rat peripheral nerve detected by *in vivo* MR imaging. *AJNR* 10:741.

Vasilescu V, Katona E, Simplaceanu V, Demco D, 1978. Water compartments in the myelinated nerve III. Pulsed NMR results. *Experimentia* 34:1443.

Vrbova G, Gordon T, Jones R, 1995. *Nerve-Muscle Interaction*, Chapmann & Hall, London.

Waller A V, 1850. Experiments on the section of the glossopharyngeal and hypoglossal nerves of the frog, and observations of the alterations produced thereby in the structure of their primitive fibres. *Phil. Trans. Roy. Soc. London B* 140:423.

Waragai M, Watanabe H, Iwabuchi S, 1994. The somatotopic localisation of the descending cortical tract in the cerebral peduncle: a study using MRI of changes following Wallerian degeneration in the cerebral peduncle after a supratentorial vascular lesion. *Neurorad.* 36:402.

Whittall K P, MacKay A L, 1989. Quantitative interpretation of NMR relaxation data. *J. Magn. Reson.* 84:134.

Whittall K P, Bronskill M P, Henkelman R M, 1991. Investigation of analysis techniques for complicated NMR relaxation data. *J. Magn. Reson.* 95:221.

Whittall K P, MacKay A L, Graeb D A, Nugent R A, Li D K B, Paty D W, 1997. *In vivo* measurement of T_2 distributions and water contents in normal human brain. *Magn. Reson. Med.* 37:34.

Woessner D E, 1961. Effects of diffusion in nuclear magnetic resonance spin-echo experiments. *J. Chem. Phys.* 34:2057.

Zur Y, Stokar S, 1987. A phase-cycling technique for cancelling spurious echoes in NMR imaging. *J. Magn. Reson.* 71:212.

Chapter 2.
T_2 Relaxation of Peripheral Nerve Measured *In vivo*[‡]

Introduction

Although peripheral nerve may regenerate following injury, it does so at a rate of only 1-5 mm/day in mammals (Sunderland, 1991). This rate of regeneration can result in weeks or months between the time of injury of a nerve and the return of function depending upon the site of injury. The ability to derive quantitative information from images of injured nerve could prove valuable in monitoring the course of nerve regeneration, as well as in an initial diagnosis of the nerve pathology. Of the various imaging modalities, only magnetic resonance appears capable of yielding such information.

Studies have shown that, given sufficient spatial resolution, peripheral nerve can be distinguished from adjoining tissue in T_2-weighted images (Howe et al., 1992; Filler et al., 1993; Enochs et al. 1994). Studies have also shown, both in images and *in vitro*, a difference to exist between the transverse relaxation of the water proton in normal and in degenerating nerve (Jolesz et al., 1984; Titelbaum et al., 1989; Rosenberg et al., 1993). In addition, *in vitro* studies of normal peripheral nerve and spinal cord have identified at least three transverse-relaxation components of nerve water and have provided evidence that these components correspond to anatomical compartments—myelin, axon, and connective tissue water (Fenrich and Allen, 1991; Menon et al., 1992; Fenrich, 1992). It would thus appear that the T_2-relaxation spectrum of peripheral nerve may reflect micro-anatomical information that could assist in the diagnosis and monitoring of pathological nerve.

Although *in vitro* studies have identified multiple T_2-relaxation components in white and grey matter (Stewart et al., 1993), spinal cord (Menon et al., 1992; Stewart et al., 1993), and peripheral nerve (Vasilescu et al., 1978; Fenrich and Allen, 1991; Fenrich, 1992), as well as in muscle (English et al., 1991), traditional T_2 measurements derived from images are usually unable to identify multiple components because either too few echoes are formed or a significant portion of the magnetisation is lost or distorted by repeated imperfect refocussing pulses. Proper estimation of the T_2 spectrum of a tissue by imaging requires a multi-echo pulse sequence capable of yielding a sufficient number of uncorrupted echoes. Using such imaging pulse sequences, multiple T_2 components have been identified in white matter (Rutt and Mitchell, 1993; Oatridge et al., 1993; MacKay et al., 1994). As a step toward the extraction of quantitative data from images of pathological nerve, this paper reports the results of a T_2 study in which normal peripheral nerve was imaged using a

---

[‡] A version of this chapter has been published in *Magnetic Resonance Imaging*, 13:575, 1995.

similar pulse sequence. An animal model was chosen to allow for future investigation of surgically induced peripheral nerve pathology.

METHODS

ANIMAL MODEL

The amphibian *Xenopus laevis* (African clawed toad) was chosen as the experimental animal because it is easily handled and exhibits negligible respiratory motion. Female specimens weighing 125-150 g were housed in water-filled tanks at room temperature and fed frog brittle (Nasco, Fort Atkinson, WI) once per week. For purposes of *in vivo* imaging, animals were anesthetized by immersion for 20-30 min in a 2% aqueous solution of urethane (ethyl carbamate) and kept moist during imaging by partially wrapping in a moist cloth. The animals remained anesthetized for 4-6 h, much longer than was required for an imaging procedure. For *in vitro* studies, following anesthesia, animals were decapitated and 1-2 cm of sciatic nerve was removed from one leg and placed in a 5-mm (o.d.) NMR tube that contained HEPES-buffered amphibian saline, pH 7.40 (Snyder, 1989). *In vitro* measurements began within 60 minutes of animal sacrifice.

IMAGING STUDIES

All experiments were performed at room temperature with a Bruker CXP 2.35-T (Bruker Analytische Messtechnik GmbH, Rheinstetten-Forchheim, Germany), 40-cm bore system. Imaging experiments used an in-house built cylindrical resonator 25 mm in diameter by 17 mm in length and in-house built gradients with an 11-cm inner diameter and maximum strengths of approximately 10 G/cm. Transverse images of the mid-thigh region of ten animals were acquired using a single-slice, 32-echo, Carr-Purcell-Meiboom-Gill (CPMG) pulse sequence (TE = 20.144 ms, TR = 2.1 s, 4 NEX) with a slice thickness of 2 mm. Each image was generated using 128 samples per echo and 128 phase-encoding steps, zero filled to 256 by 256. Prior to reconstruction the raw data was multiplied by a Hamming window in order to reduce Gibbs artefact (Kuc, 1988). The field of view was 27-mm square, resulting in a spatial resolution of approximately 200 x 200 μm^2.

The pulse sequence used a 1024-μs Gaussian modulated 90° excitation pulse, 640-μs Version S composite 180° refocussing pulses (Poon and Henkelman, 1992), and an alternating and decreasing pattern of spoiler gradients (Crawley and Henkelman, 1987; Poon and Henkelman, 1993) with a smallest dephasing strength of approximately π per pixel. The composite refocussing pulses, designed to be relatively insensitive to both B_1 and B_0 inhomogeneities, minimized the appearance of increased relaxation due to unrefocussed magnetisation, while the spoiler gradients dephased unwanted magnetisation

that would otherwise corrupt echo intensity. The accuracy of T_2 values estimated from imaged data was assessed by a comparison between imaged and non-imaged data obtained from aqueous $CuSO_4$ solutions of varying concentration.

In vitro Studies

The transverse relaxation of nine samples of sciatic nerve was measured using a phase-cycled CPMG sequence with a *TE* of 1.6 ms and a *TR* of 20 s. A total of 16 excitations was generated with 4096 echoes collected per excitation. From these echoes, 256 logarithmically spaced echoes were extracted for processing.

Analysis of Data

T_2 components of nerve and muscle were estimated from images; only the T_2 components of nerve were estimated from *in vitro* experiments. Nerve and muscle regions of interest (ROIs) were visually segmented on a pixel by pixel basis from the images. ROIs of nerve were conservatively segmented for analysis in an effort to minimize possible partial volume effects. The cross-sectional area of the sciatic nerve was estimated from images and dissection to be 0.25-0.75 mm^2; nerve ROIs were restricted to a maximum of 0.18 mm^2. T_2-relaxation data were fitted, in a non-negative least squares sense (*NNLS*), to a sum of decaying exponentials and smoothed with a minimum energy constraint (Whittall and MacKay, 1989). *In vitro* T_2 data were fitted to 96 exponentials with logarithmically distributed T_2 times between 10 ms and 5 s, while image data were fitted to 32 exponentials logarithmically distributed between one half the shortest and twice the longest echo times.

On the basis of the T_2-relaxation components of nerve, estimates were made of the optimal echo time(s) for nerve visualization. The ability to visualize a structure may be quantified in terms of a contrast-to-noise ratio (*CNR*) which, for purposes of this paper, is defined as the difference between the average nerve and muscle signals divided by the standard deviation of the noise per pixel. The standard deviation of the noise was estimated for each echo as that of the signal from muscle in the vicinity of the sciatic nerve. In order to determine the effect of multi-echo averaging on noise, and in-turn on the *CNR*, the standard deviation of the noise was estimated from images that were the cumulative average of images.

Results

Four images from the same animal but with different echo times are shown in Fig. 2.1. From these images it is clear that the sciatic nerve is readily distinguishable from the adjacent muscle in the latter echoes and that the average transverse relaxation time of nerve is much longer than that of muscle. Typical *in vitro* and image-derived sciatic nerve T_2 spectra are shown in Fig. 2.2.

Table 2.1 summarizes T_2 results for nerve and muscle, identifying three components from both *in vitro* nerve and imaged nerve, and one component from muscle. Analysis of data acquired from images of $CuSO_4$ solutions (not shown) revealed that imaged T_2 values underestimated *in vitro* derived values by less than 10% (cf. Poon and Henkelman, 1993).

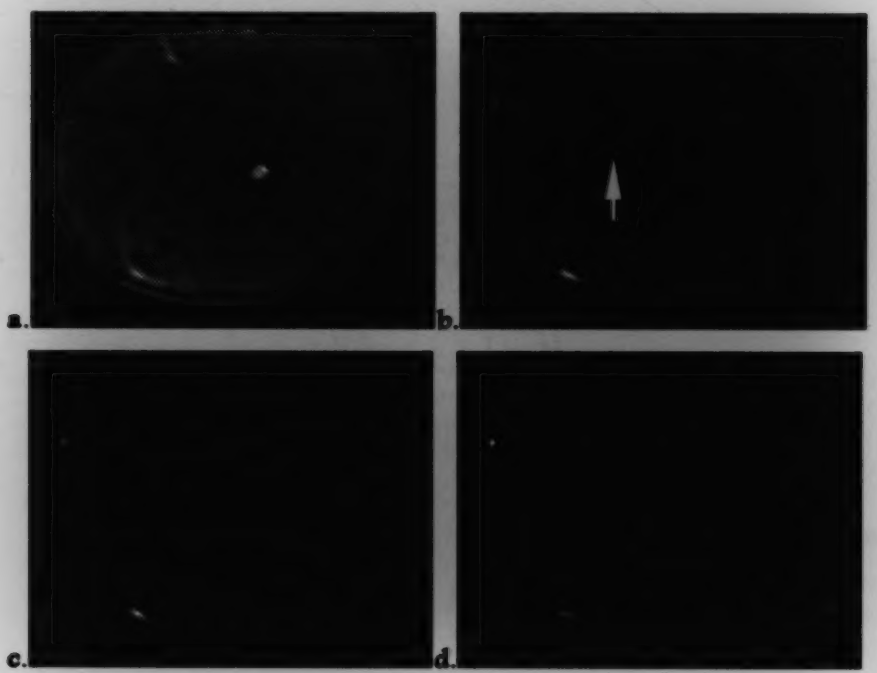

Fig. 2.1. Four transverse images from a 32-echo set of the thigh of *Xenopus laevis* corresponding to echoes 1, 4, 8, and 16 (TE = 20.144 ms). The sciatic nerve is identified by the arrow in the TE = 80.6 ms image. The dark circles slightly above and to the left of the nerve are the femoral vein and artery (from left to right). The bone marrow (bright) surrounded by the cortical region (dark) of the femur are seen slightly below and to the right of the nerve. The sharp bend in the skin on the upper right of the image is due to the wrap-around plastic spacer that separated the thigh from the coil. The maximum width of the thigh is approximately 15 mm.

Analysis revealed the standard deviation of the noise to contain both a constant and an echo-dependent portion, the latter of which decreased monotonically with echo number. The decreasing portion of noise resulted in a *CNR* of 20 to 30 for images corresponding to echoes 120-260 ms following excitation. Summing images revealed that the standard deviation of the noise increased nearly linearly with each echo during the times that the echo-dependent noise was significant. As this noise decreased in significance, the standard deviation began to increase as the square root of the number of summed images. It was

found numerically that the greatest improvement in *CNR* resulted from averaging the 11th through 25th echo images, although a broad maximum existed for the choice of the longest echo image to include in the average. Figure 2.3 shows the average image obtained from echoes 11 through 25 for the same animal as depicted in Fig. 2.1. The *CNR* in this image is approximately 80.

Structure	*n*	T_2 (ms ± S.D.)	Population (% ± S.D.)
Nerve†	9	16 ± 2	16 ± 2
		78 ± 6	48 ± 3
		317 ± 18	36 ± 3
Nerve‡	10	19 ± 7	26 ± 9
		63 ± 31	29 ± 11
		241 ± 24	45 ± 7
Muscle‡	6	44 ± 4	100

Table 2.1. Measured multi-exponential transverse relaxation times of nerve and muscle.
† Data acquired spectroscopically (*in vitro*).
‡ Data acquired by imaging (*in vivo*).

Discussion

There appears to be a good correlation between the *in vitro* and imaged T_2 spectral data, although some points are worth noting. Although the uncertainties of the parameter values estimated from the imaged data are somewhat larger than those from the *in vitro* data, this is not surprising considering the relatively long echo time (*TE*) used for imaging and a signal-to-noise ratio 25 times lower than that obtained *in vitro*. Differences in component fractions between *in vitro* and imaged spectra are at least partially due to T_1 weighting that results from a *TR* of 2.1 s used for imaging.

The observation here *in vivo* of a long-lived T_2 component in peripheral nerve provides support for a similar component observed by others *in vitro* (Vasilescu et al., 1978; Fenrich and Allen, 1991; Fenrich, 1992; Menon et al., 1992). The existence of long-lived T_2-relaxation provides substantially improved visualization of nerve in T_2-weighted images. Previous magnetic resonance images suggest that nerve is best visualized in T_2-weighted images (*TE* approximately 70-105 ms), with further improvement from diffusion or diffusion anisotropy weighting (Howe et al., 1992; Enochs et al. 1994). The multi-echo images presented here indicate that an echo time as long as 200-300 ms may provide maximal *CNR* by T_2-weighting, with multi-echo averaging providing a simple means of further improving peripheral nerve visualization. The *CNR* value of 80 present in the average image (Fig. 2.3) represents nearly a three-fold increase over the best single-echo image *CNR*.

Imaging sequences or post-processing that reduces or eliminates echo-dependent noise may result in a still greater increase in *CNR* due to multi-echo averaging.

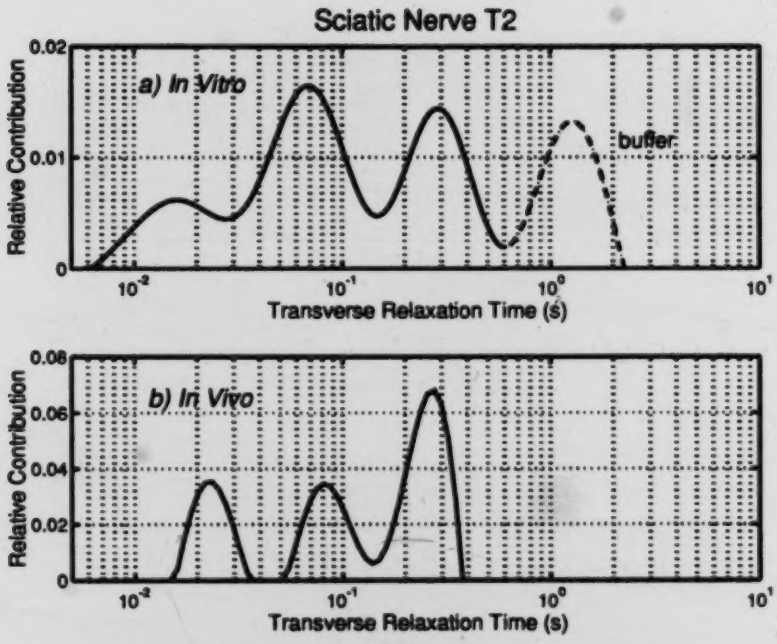

Fig. 2.2. T_2 spectra of the sciatic nerve of *Xenopus laevis* measured a) *in vitro* and b) *in vivo*. In a) the longest-lived component (dashed line) is due to buffer.

Conclusion

Using a multi-echo imaging sequence designed to generate uncorrupted echo trains, three T_2-relaxation components are seen in peripheral nerve *in vivo*, including a long-lived component ($T_2 > 200$ ms) which previously has only been identified *in vitro*. The existence of a long-lived T_2-relaxation component indicates echo times as long as 200-300 ms may provide maximal *CNR* (nerve to muscle) in T_2-weighted images. By averaging selected images from the multi-echo image set, the *CNR* may be increased by a factor of nearly three.

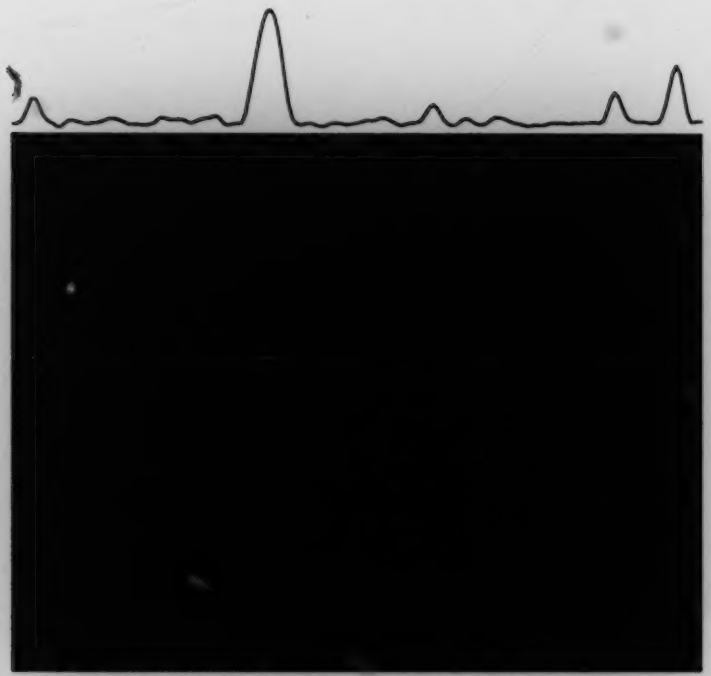

Fig. 2.3. Image obtained by averaging the 11th through 25th echo images of the 32-echo set presented in Fig. 2.1. The intensity profile at the top of the image corresponds to the horizontal line that passes through the sciatic nerve. The contrast-to-noise ratio as defined in the text is approximately 80.

References

Crawley A P, Henkelman R M, 1987. Errors in T_2 estimation using multislice multiple-echo imaging. *Magn. Reson. Med.* 4:34.

English A E, Whittall K P, Joy M L G, Henkelman R M, 1991. Quantitative two-dimension time correlation relaxometry. *Magn. Reson. Med.* 22:425.

Enochs W S, 1994. MR imaging of the peripheral nervous system. *J. Magn. Reson. Imag.* 4:251.

Fenrich F R E, Allen P S, 1991. Transverse relaxation rate distributions for water protons in myelinated and unmyelinated nerves. *Proc. of SMRM. 10th Annual Meeting.* p. 693.

Fenrich F R E, 1992. *A simulation and experimental study of water proton relaxation in a white matter model.* M.Sc. Thesis, University of Alberta.

Filler A G, Howe F A, Hayes C E, Kliot M, Winn H R, Bell B A, Griffiths J R, Tsuruda J S, 1993. Magnetic resonance neurography. *Lancet* 341:659.

Howe F A, Filler A G, Bell B A, Griffiths J R, 1992. Magnetic resonance neurography. *Magn. Reson. Med.* 28:328.

Jolesz F A, Polak J F, Ruenzel P W, Adams D F, 1984. Wallerian degeneration demonstrated by magnetic resonance: spectroscopic measurements on peripheral nerve. *Radiology* 152:85.

Kuc R, 1988. *Introduction to Digital Signal Processing*, McGraw-Hill, New York.

MacKay A, Whittall K, Adler J, Li D, Paty D, Graeb D, 1994. *In vivo* visualization of myelin water in brain by magnetic resonance. *Magn. Reson. Med.* 31:673.

Menon R S, Rusinko M S, Allen P S, 1992. Proton relaxation studies of water compartmentalisation in a model neurological system. *Magn. Reson. Med.* 28, 264.

Oatridge A, Hajnal J V, Kasuboski L, Young I R, Bydder G M, 1993. Measurement of long T_2 components in normal brain tissue. *Proc. of the SMRM. 12th Annual Meeting.* p. 348.

Poon C S, Henkelman R M, 1992. Practical T_2 quantitation for clinical applications. *J. Magn. Reson. Imag.* 2:541.

Poon C S, Henkelman RM, 1993. 180° refocussing pulses which are insensitive to static and radiofrequency field inhomogeneity. *J. Magn. Reson.* 99:45.

Rosenberg Z S, Beltran J, Cheung Y Y, Ro S Y, Green S M, Lenzo S R, 1993. The elbow: MR features of nerve disorders. *Rad.* 188:235.

Rutt B K, Mitchell J D, 1993. Myelin-selective imaging with 3D fast spin echo MRI. *Proc. of the SMRM. 12th Annual Meeting.* p. 137.

Snyder R E, 1989. Loss of material from the retrograde axonal transport system in frog sciatic nerve. *J. Neurobiol.* 20:81.

Stewart W A, MacKay A L, Whittall K P, Moore G G, W, Paty D W, 1993. Spin-spin relaxation in experimental allergic encephalomyelitis. Analysis of CPMG data using a non-linear least squares method and linear inverse theory. *Magn. Reson. Med.* 29:767.

Sunderland S, 1991. *Nerve Injuries and their Repairs*, Churchill Livingstone, Edinburgh.

Titelbaum D S, Frazier J L, Grossman R I, Joseph P M, Yu L T, Kassab E A, Hickey W F, LaRossa D, Brown M J, 1989. Wallerian degeneration and inflammation in rat peripheral nerve detected by *in vivo* MR imaging. *AJNR* 10:741.

Vasilescu V, Katona E, Simplaceanu V, Demco D, 1978. Water compartments in the myelinated nerve III. Pulsed NMR results. *Experimentia* 34:1443.

Whittall K P, MacKay A L, 1989. Quantitative interpretation of NMR relaxation data. *J. Magn. Reson.* 84:134.

Chapter 3.
Multi-Exponential T_2 Relaxation in Degenerating Peripheral Nerve[‡]

Introduction

Magnetic resonance imaging serves as a modality for the investigation of abnormalities of the peripheral nervous system (PNS). To date, diagnoses have rested largely upon morphological findings (Enochs, 1994). Although some abnormalities have been observed to result in changes in the signal intensity of nerve (Jolesz et al., 1984; Middleton et al., 1987; Titelbaum et al., 1989; Filler et al, 1993; Rosenberg et al., 1993), these changes in themselves have not been used to distinguish between neuropathies. Imaging methods capable of rendering information related to the function or microanatomy of nerve, although potentially valuable in a differential diagnosis, have, with few exceptions (Filler et al., 1994), yet to be developed. This paper reports on one such method, measurement of the transverse (T_2) relaxation spectrum of nerve, and shows that spectral changes can be observed as the result of Wallerian degeneration that follows traumatic injury to nerve.

Imaging of the PNS was initially restricted by the supposition that nerve is iso-intense with muscle (Fahr and Sauser, 1988; Enochs, 1994), limiting visualization of nerve to regions where it is juxtaposed to tissues such as cortical bone, tendon, or adipose tissue, although visualization has been aided with the use of fat suppression, diffusion anisotropy, and paramagnetic contrast agents (Enochs, 1994; Howe et al., 1992). More recent studies, however, have demonstrated that nerve is hyperintense to muscle in heavily T_2-weighted images (Howe et al., 1992; see Chapter 2), thus making it possible to image nerve in essentially the entire body.

Early magnetic resonance studies suggested nerve to be characterised by multi-exponential T_2 (MET_2) relaxation of water (Swift et al., 1969; Vasilescu et al., 1978). This has been confirmed by more recent *in-vitro* studies that have identified at least three exponential rates of T_2 decay in normal nerve (Fenrich and Allen, 1991; Menon et al., 1992). Employing protocols designed specifically for multi-echo imaging together with newer methods of data analysis three T_2 components have now been observed *in vivo* in peripheral nerve (see Chapter 2). Although the origin of these components remains uncertain, evidence suggests each is derived from a different anatomic water compartment of nerve: myelinic, axonal, and extra-axonal (Fenrich and Allen, 1991; Fenrich, 1992; Menon et al., 1992; Stewart et al., 1993; MacKay et al., 1994). If this is

---

[‡] This work was presented in part at the 2nd Annual Meeting of the Society of Magnetic Resonance, August 1994, San Francisco. Also, a version of this chapter has been published in *Magnetic Resonance in Medicine*, 35:207, 1996.

correct, pathologies which result in alterations to the microanatomy of nerve, such as demyelination or axonal loss, may be reflected in the MET_2 relaxation spectra of nerve, making such spectra potentially valuable as clinical adjuncts in assessing nerve pathology. To test the hypothesis that changes in microanatomy may be reflected in the T_2-relaxation spectra, nerve was studied both *in vivo* and *in vitro* as it underwent Wallerian degeneration following crush injury.

METHODS

ANIMAL MODEL

The amphibian *Xenopus laevis* (African clawed toad) was chosen as the experimental animal because it is easily handled and exhibits negligible respiratory motion. Female specimens weighing 125-150 g were housed in water-filled tanks at room temperature and fed frog brittle (Nasco, Fort Atkinson, WI) once per week. Surgery was performed on a total of 18 animals following their being anaesthetized in a 2% aqueous solution of urethane (ethyl carbamate). The sciatic nerve in one leg was exposed at the upper-thigh level and crushed with a nylon thread drawn against a glass rod for 30 seconds. This procedure has been shown histologically to interrupt all nerve fibres (Chan et al., 1989). The skin incision was closed and the animals, following recovery, were returned to their holding tanks. For purposes of *in-vivo* imaging, animals were anesthetized as for surgery and kept moist during imaging by partially wrapping in a moist cloth. The animals remained anesthetized for 4-6 h, much longer than was required for an imaging procedure. For *in-vitro* studies, following anesthesia, animals were decapitated and 1-2 cm of sciatic nerve was removed from one leg and placed in a 5-mm (o.d.) NMR tube that contained HEPES-buffered amphibian saline, pH 7.40 (Snyder, 1989). *In-vitro* measurements began within 60 minutes of animal sacrifice. Following some *in-vitro* measurements, nerves were fixed and transverse sections prepared for light microscopy as described in the literature (Chan et al., 1989).

IN-VITRO STUDIES

At three different times following surgery 4-6 animals each time were sacrificed and the transverse relaxation of their excised degenerating sciatic nerve was measured *in vitro*. For some animals, the contralateral normal nerve was also measured *in vitro*. A phase-cycled CPMG sequence was used with a TE of 1.6 ms, a TR of 20 s, and 16 excitations of $n = 4096$ echoes each. From the full set of data, 128 logarithmically-spaced echoes were extracted for processing. These data were then fitted in a non-negative least squares (NNLS) sense to the sum of 96 decaying exponentials with logarithmically distributed T_2 times between 10 ms and 5 s, and smoothed with a minimum energy constraint (Whittall and MacKay, 1989). The minimum energy constraint was

adjusted such that the χ^2 statistic was increased to the 75% confidence limit as described by Whittall and MacKay (Whittall and MacKay, 1989). Fitting to relaxation times as long as 5 seconds was necessitated by the relatively long T_2 relaxation time (1-2 s) of the buffer solution in which the nerves were bathed.

Imaging Studies

All NMR experiments were performed at room temperature with a Bruker CXP 2.35-T 40-cm bore system. Experiments used an in-house built cylindrical resonator 25 mm in diameter by 17 mm in length to image the thigh of *Xenopus* and in-house built gradients with an 11-cm inner diameter and maximum strengths of approximately 10 G/cm. Imaging of the degenerating nerve was performed at various times between 4 and 35 days following surgery. Upon a number of occasions the contralateral (normal) sciatic nerve was also imaged. Transverse images of the mid-thigh region were acquired using a single-slice, 32-echo, Carr-Purcell-Meiboom-Gill (CPMG) protocol (TE = 20.144 ms, TR = 2.1 s, 4 NEX) with a slice thickness of 2 mm. The image plane was located approximately 10 mm distal to the site of the nerve crush for degenerating nerves, with a similar location selected for the imaging of normal nerves. The pulse sequence used a 1024-μs Gaussian modulated 90° excitation pulse, 640-μs Version S composite 180° refocussing pulses (Poon and Henkelman, 1992), and an alternating and decreasing pattern of spoiler gradients (Crawley and Henkelman., 1987; Poon and Henkelman, 1993) with a smallest dephasing strength of approximately π per pixel. The composite refocussing pulses, designed to be relatively insensitive to both B_1 and B_0 inhomogeneities, minimized the appearance of increased relaxation due to unrefocussed magnetisation, while the spoiler gradients dephased unwanted magnetisation that would otherwise corrupt echo intensity. This protocol has been demonstrated to underestimate T_2 values acquired from $CuSO_4$ by no more than 10% (see Chapter 2).

Each image was generated using 128 samples per echo and 128 phase-encoding steps, and zero filled to 256 by 256. Prior to reconstruction the raw data was multiplied by a Hamming window to reduce Gibbs artefact (Kuc, 1988). The field of view was 27-mm square, resulting in a spatial resolution of approximately 200 x 200 μm^2. Nerve regions of interest (ROIs) were visually segmented on a pixel by pixel basis from the images. At echo times beyond ≈ 40 ms the normal sciatic nerve is hyperintense compared to surrounding muscle tissue and thereby easily segmented (see Chapter 2). A few images obtained from frogs less than two-weeks post-surgery occasionally contained hyperintense pixels bordering the nerve, possibly due to fluid accumulation resulting from the surgery. To insure that such pixels were not included for analysis as well as to avoid partial volume effects, only those pixels near the core of a nerve and having similar signal intensities were included in a ROI. This resulted in ROIs being restricted to a maximum of 0.18 mm^2, compared to

the cross-sectional area of normal sciatic of 0.25-0.75 mm^2 as estimated from images and dissection. T_2-relaxation data were fitted in an NNLS sense (Whittall and MacKay, 1989) to a sum of 64 decaying exponentials, logarithmically distributed between the shortest and twice the longest relaxation times found *in vitro*. Smoothed spectra were not generated from image data as it has been shown that with relatively low signal-to-noise data, unconstrained NNLS solutions are more likely to identify the correct number of spectral components (Graham et al., 1994).

Results

Magnetic Resonance

T_2-relaxation spectra derived from the *in-vitro* CPMG measurement of normal frog nerve and nerve at three different post-surgery times are shown in Fig. 3.1. In order to demonstrate the variation of frog nerve MET_2 data, the spectrum from every *in-vitro* measurement is included. The notable similarity between all normal nerve spectra suggests that the variation seen in the spectra of degenerating nerve is due to physiological variation as opposed to limitations of the measurement or analysis processes. The spectral domains in Fig. 3.1 have been truncated at a T_2 of one second in order to exclude the large spectral component due to the buffer in which the nerves were bathed during measurement.

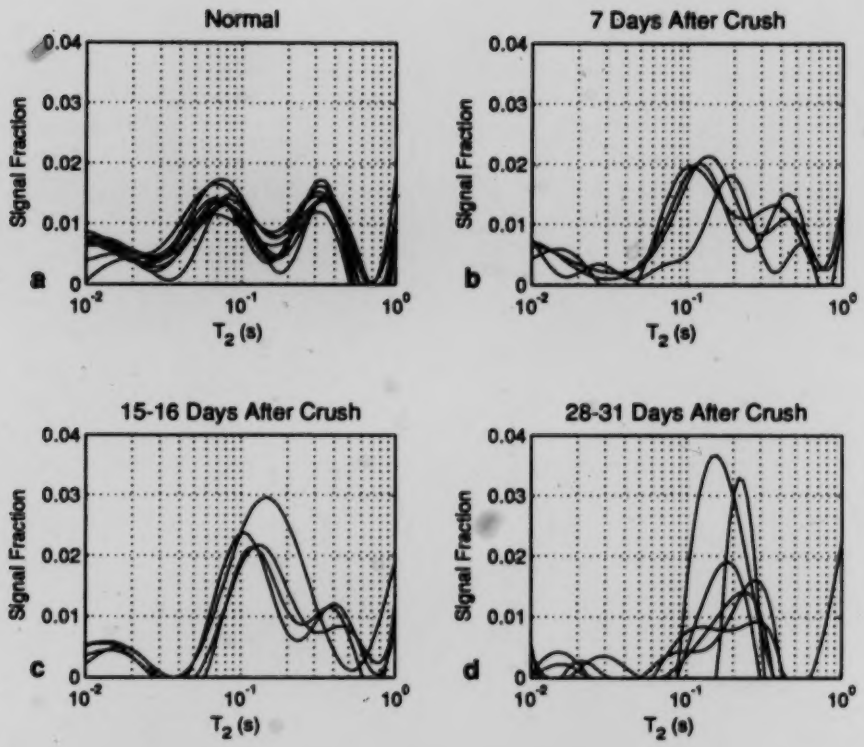

Fig. 3.1. T_2 spectra of the sciatic nerve of *Xenopus* measured *in vitro*, corresponding to a) normal, b) 7 days post-injury, c) 15-16 days post-injury, and d) 28-31 days post-injury.

Images at the mid-thigh level of a normal (unoperated) frog leg and legs at three different times following surgery are shown in Fig. 3.2. Injury is seen to result in an increase in signal intensity in the region corresponding to the sciatic nerve of operated legs in comparison to the unoperated leg. This is also evident in Fig. 3.3 in which the intensity of normal and degenerating nerves is plotted versus echo time. Figure 3.2 suggests an increase in the size of injured compared to normal nerve. No attempt was made to quantify the cross-sectional area of injured nerve, however histology (see below) and physical examination of nerves used in the *in-vitro* study suggested that an increase in nerve volume did occur, especially during the first two weeks following surgery.

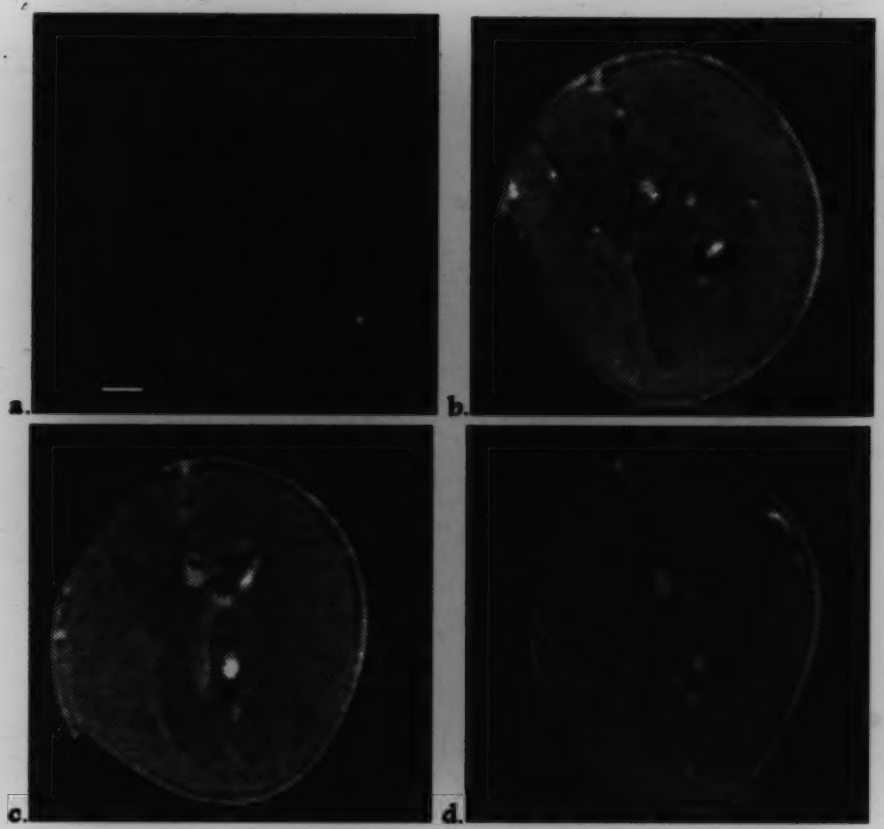

Fig. 3.2. Four transverse images from the thigh of *Xenopus* corresponding to a) normal, b) 7 days post-injury, c) 14 days post-injury, and d) 32 days post-injury. Each image is from the third echo (≈ 60 ms) of a 32 echo data set. The sciatic nerve is identified by the arrow in the normal nerve image and can be seen in a similar location in each of the degenerating nerve images. The dark circles slightly above and to the left of the nerve are the femoral vein and artery (from left to right). The bone marrow (bright) surrounded by the cortical region (dark) of the femur are seen slightly below and to the right of the nerve. The sharp bend in the skin on the image (seen in the lower right of a) is due to the wrap-around plastic spacer that separated the thigh from the coil. Scale bar in lower-left corner of Fig. 3.2a represents 2 mm and applies to Figs. 3.2a-d.

The T_2 spectra derived from image-measured data and associated with the four images of Fig. 3.2 are shown in Fig. 3.4. Each NNLS spectral fit was found to be acceptable on the basis of having a χ^2 statistic value less than one standard deviation different from the expected χ^2 value (Whittall et al., 1991). The most striking feature of the spectra of degenerating nerve is a reduction in the number of resolvable components as a function of increased post-operative time. In agreement with an earlier study (see Chapter 2), image-measured T_2

spectra of normal frog sciatic nerve consistently resolved into three components; however, this was not the case for degenerating nerve measured in this study. Five of six measurements made 4 days following surgery were resolved into three components, as were six of ten on day 7, and four of six made on day 11. Beyond 11 days post-surgery, three components were resolved in only 6 of 43 measurements. In order to average results obtained from different animals, only those spectra that resolved into three (two) components for data obtained ≤ 11 d (> 11 d) post-surgery were included in subsequent analysis (Table 3.1). It is important to note, however, that the data not included in Table 3.1 agree in general with the included data, both *in vivo* and *in vitro*, but were simply not amenable to direct comparison. T_2 values less than 50 ms were considered part of what is herein referred to as the low T_2 component. In the case of three components, the intermediate component refers to signal with T_2 values between 50 and 150 ms, while no intermediate component is defined in two component cases. Table 3.1 contains the average image-measured MET_2 values and signal fractions for normal and degenerating nerve. A feature evident in Table 3.1 is the reduction in the low T_2 component fraction as a function of post-operative time, seen more clearly in Fig. 3.5.

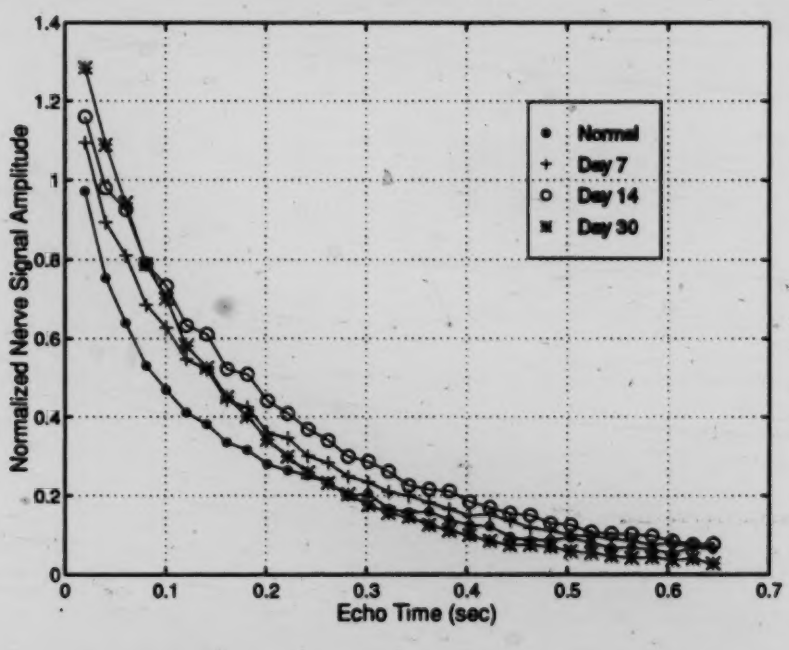

Fig. 3.3. Signal intensity versus echo time for normal and degenerating nerve. Each data point results from the average of ROI nerve intensities from six images normalized to the intensity of muscle for the first echo.

HISTOLOGY

Figure 3.6 shows representative light-microscope sections of normal and degenerated nerve from the regions imaged. Normal nerve (Fig. 3.6a) is seen to be composed largely of myelinated axons, typically 13-17 μm in diameter. The axons are arranged more or less uniformly with mean separations of 2-5 μm, larger gaps being filled with smaller myelinated and unmyelinated axons. The section of nerve fixed 7 days following injury (Fig. 3.6b) shows myelinated axons that appear similar to those in the normal section, but having an increased mean separation characteristic of interstitial oedema. By day 15 (Fig. 3.6c) the majority of myelinated axons have undergone some degree of collapse, and their separations, while less than at 7 days, remain greater than in normal nerve. Examples of myelin disintegration are occasionally seen, although the amount of myelin does not appear to be substantially reduced from day 7. Regenerating, but unmyelinated as yet, axons are occasionally seen. By 28 days following surgery (Fig. 3.6d) few degenerating axons remain, myelin loss is substantial, and regenerating axons are evident.

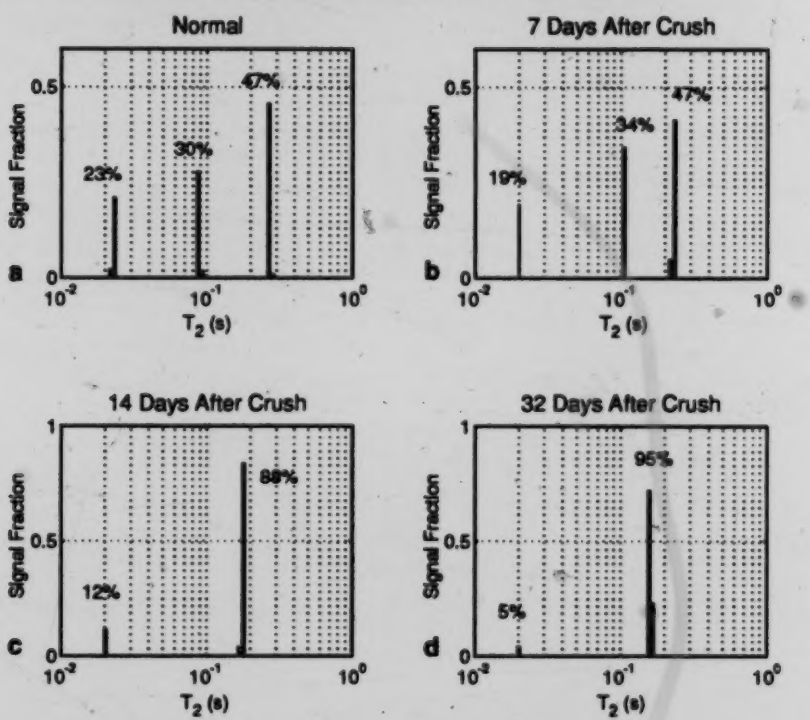

Fig. 3.4. Typical T_2 spectra of the sciatic nerve of *Xenopus* measured *in vivo*, corresponding to a) normal, b) 7 days post-injury, c) 14 days post-injury, and d) 32 days post-injury.

Discussion

The primary finding of this study is that Wallerian degeneration results in measurable changes in the T_2 relaxation spectra of nerve. Histologic observations verify the occurrence of Wallerian degeneration and agree with the known evidence of nerve degeneration and regeneration (Dyck, 1975; Schröder, 1975; Sunderland, 1991).

		Low T_2 Component		Intermediate T_2 Component		High T_2 Component	
Sample	N	T_2 (ms)	Fraction (%)	T_2 (ms)	Fraction (%)	T_2 (ms)	Fraction (%)
Normal	10	22±3	27±7	71±16	29±10	247±26	44±6
day 4	4	24±8	23±11	78±22	35±9	215±14	42±7
day 7	6	21±2	17±6	111±26	33±14	286±45	50±17
day 11	4	20±0	13±8	107±27	37±15	344±93	51±16
day 14-16	10	24±9	13±10	-	-	202±29	87±10
day 21-25	12	20±0	5±7	-	-	187±22	95±7
day 28-35	21	22±6	4±5	-	-	143±25	96±5

Table 3.1. Image (*In vivo*) measured T_2 parameters (± S.D.) of normal and degenerating peripheral nerve.

A number of studies report Wallerian degeneration, both in the central (Koenig et al., 1990; Terae et al., 1993; Pennock et al., 1993; Waragai et al., 1994) and in the peripheral (Jolesz et al., 1984; Titelbaum et al., 1989) nervous systems, to be manifested as an increase in signal intensity in MRI. The results here confirm this finding, but, of greater importance, offer insight into the anatomic changes that underlie this increase in intensity. The most apparent difference between the MET$_2$ relaxation spectra of normal and degenerated (> 4 weeks post-injury) nerve (Figs. 3.1 and 3.4) is a transition from non-monoexponential spectra with three well-defined T_2 components to spectra composed almost entirely of one component. The ability to resolve and quantify spectral components using NNLS techniques (Whittall and MacKay, 1989) is dependent upon the number of echoes used, their times in relation to the spectral relaxation times, and the signal-to-noise ratio of the data (Fenrich,

1992; Graham et al., 1994). The inability to resolve an intermediate component in some cases during the first 11 days following injury is likely primarily indicative of the lower spectral resolution available from imaging, due to fewer echoes and a lower signal-to-noise ratio compared to in-vitro studies, as three components can be seen in all but one in-vitro measured spectra (Fig. 3.1) up to 15-16 days post surgery. By four weeks of degeneration, neither in-vitro nor in-vivo measurements resolve into three components, suggesting the disappearance of two separate long-lived water pools.

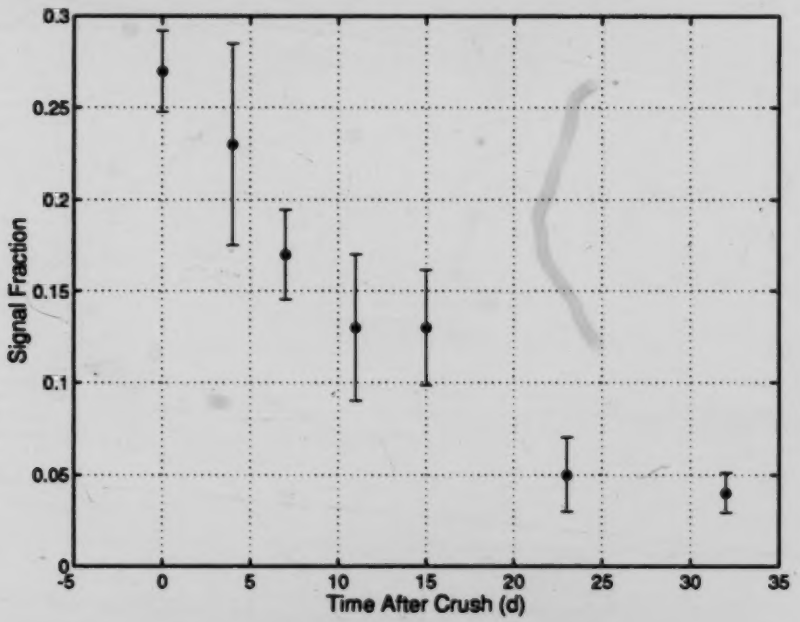

Fig. 3.5. Fraction of spectra corresponding to low T_2 component determined from *in-vivo* measurements versus time following operation. Error bars represent ± 1 S.E.M.

The reduction from three to two components coincides with the collapse of myelinated fibres. Although the histology shows that degenerating nerve throughout the course of this study can not be considered truly homogeneous (Fig. 3.6), the anatomical heterogeneity in four-week degenerated nerve results primarily from aqueous pools bounded by thin membrane layers, and not the multi-membrane layers of myelin. Previous work (Fenrich and Allen, 1991; Fenrich, 1992; Menon et al., 1992; MacKay et al., 1994; Stewart et al., 1993) that assigned the three T_2 components to myelinic, axonal, and extra-axonal water, in order of increasing T_2 value, did so by reasoning, in part, that whereas the permeability of plasma membrane to water is such as to allow for the rapid mixing of nerve water, the closely packed layers of myelin (typically >

30 for *Xenopus* sciatic nerve) are a significant diffusion barrier on the time scale of nerve water T_2 relaxation to prevent the mixing of axonal and extra-axonal water (Koenig et al., 1990). This is consistent with the histology that, although showing axonal regeneration, shows very little space enclosed by myelin. Therefore, it is concluded that with the collapse of myelinated fibres, water pools no longer remain segregated by myelin and the two long-lived T_2 components merge into one.

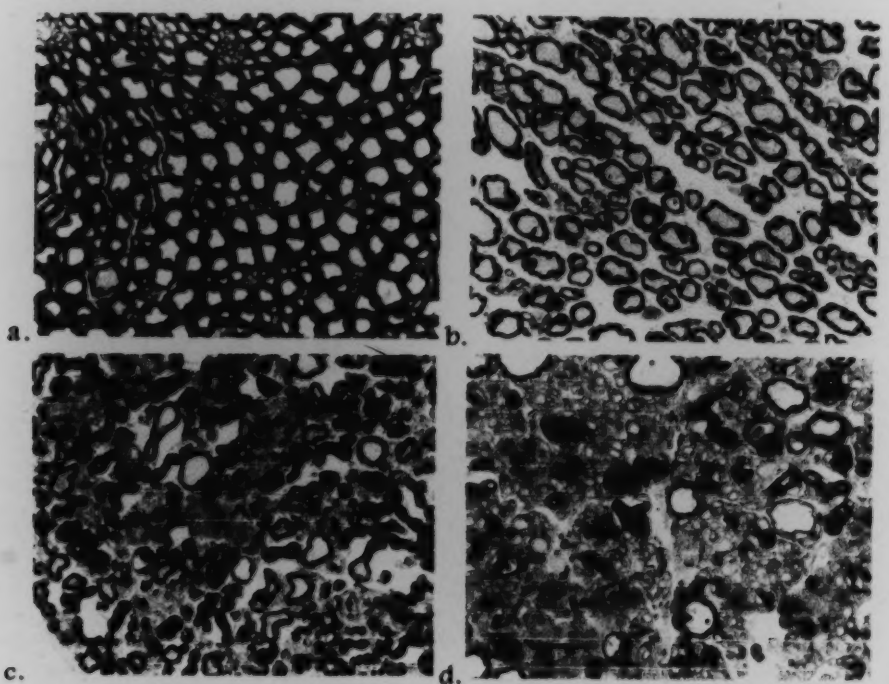

Fig. 3.6. Light micrographs of sciatic nerve of *Xenopus*. a) Normal nerve: myelinated fibres are regularly and closely packed. b) 7 days post-injury: inter-axonal space is greatly increased and axonal discontinuity is noticeable. c) 14 days post-injury: most myelinated fibres are collapsed and small regenerating axons are visible. d) 28 days post-injury: significant myelin loss is evident and regenerating axons are abundant. Scale bar in lower-left corner of Fig. 3.6d represents 40 μm and applies to Figs. 3.6a-d.

A second measurable change as degeneration progresses is a reduction in the signal fraction associated with the low T_2 component, seen in both the in-vivo and the in-vitro data. Other researchers have presented evidence to suggest this component to be associated with the myelin water pool of nervous tissue: absence of a low T_2 component in unmyelinated nerve (Fenrich, 1992) and in gray matter of brain (Kreis et al., 1992; Rutt and Mitchell, 1993; MacKay et al., 1994). This assignment is consistent with the results here for degenerating nerve. However, it must be noted that a reduction in the low T_2 component

signal fraction does not in itself signify a loss of myelin; interstitial oedema, as is particularly evident within the first two weeks following nerve injury (Fig. 3.6), also contributes. Between two and four weeks following injury the signal fraction of the low T_2 component continues to decline, and it is during this period that a significant amount of myelin breakdown occurs.

Some differences exist between in-vivo and in-vitro data which may be due, to some degree, to the difference in signal localization between in-vitro and in-vivo measurements. *In vivo* the signal is localised in a slice (2 mm) of nerve approximately 10 mm from the crush site, while in-vitro measurements include signal from a 10-20 mm long section of nerve beginning immediately distal to the crush. Axonal necrosis is expected to be relatively uniform along the nerve (Malbouisson et al., 1984), but both myelin degeneration and remyelination progress in a proximal-distal manner (Lubinska, 1984; Sunderland, 1991). Thus, the in-vitro measurements, derived from nerve on both sides of the imaging slice, may contain more old myelin distal and some new myelin proximal to the image slice, resulting in a higher average low component signal fraction. Nevertheless, the pattern of MET_2 change seen *in vitro* (Fig. 3.1) agrees with, and thereby corroborates, the image-measured data (Fig. 3.4 and Table 3.1).

Conclusion

Multi-echo imaging showed that progressive changes are observable in the T_2 relaxation spectra of frog sciatic nerve undergoing Wallerian degeneration. The two most apparent changes as degeneration progressed are a reduction from three well-resolved T_2 components to one and a decline in the fraction of the spectra associated with the low T_2 component. The former change appears to reflect a collapse of myelinated fibres, while the latter a combination of interstitial oedema and myelin loss.

References

Chan H, Smith R S, Snyder R E, 1989. Junction between parent and daughter axons in regenerating myelinated nerve: properties of structure and rapid axonal transport. *J. Comp. Neurol.* 283:391.

Crawley A P, Henkelman R M, 1987. Errors in T_2 estimation using multislice multiple-echo imaging. *Magn. Reson. Med.* 4:34.

Dyck P J, 1975. "Pathological alterations of the peripheral nervous system of man", in *Peripheral Neuropathy* (P. J. Dyck, P. K. Thomas, E. H. Lambert Eds.) pp. 296-336, Saunders, Philadelphia.

Enochs W S, 1994. MR imaging of the peripheral nervous system. *J. Magn. Reson. Imag.* 4:251.

Fahr L M, Sauser D D, 1988. Imaging of peripheral nerve lesions. *Orthop. Clin. North Amer.* 19:27.

Fenrich F R E, Allen P S, 1991. Transverse relaxation rate distributions for water protons in myelinated and unmyelinated nerves. *Proc. of SMRM. 10th Annual Meeting.* p. 693.

Fenrich F R E, 1992. *A simulation and experimental study of water proton relaxation in a white matter model.* M.Sc. Thesis, University of Alberta.

Filler A G, Howe F A, Hayes C E, Kliot M, Winn H R, Bell B A, Griffiths J R, Tsuruda J S, 1993. Magnetic resonance neurography. *Lancet* 341:659.

Filler A G, 1994. Axonal transport and MR imaging: prospects for contrast agent development. *J. Magn. Reson. Imag.* 4:259.

Graham S J, Stanchev P L, Bronskil M J, 1994. Feasibility of multicomponent T_2 relaxation analysis using data measured on clinical MR scanners, *in Proc., SMR, 2nd Annual Meeting,* p. 848.

Howe F A, Filler A G, Bell B A, Griffiths J R, 1992. Magnetic resonance neurography. *Magn. Reson. Med.* 28:328.

Jolesz F A, Polak J F, Ruenzel P W, Adams D F, 1984. Wallerian degeneration demonstrated by magnetic resonance: spectroscopic measurements on peripheral nerve. *Radiology* 152:85.

Koenig S H, Brown R D III, Spiller M, Lundbom, 1990. Relaxometry of brain: why white matter appears bright in MRI. *Magn. Reson. Med.* 14:482.

Kreis R, Fusch C, Boesch C, 1992. *In vivo* characterisation of three water compartments in human white matter using a single voxel technique with short TE. *Proc. of the SMRM. 11th Annual Meetin*" p. 1963.

Kuc R, 1988. *Introduction to Digital Signal Processing,* McGraw-Hill, New York.

Lubinska L, 1984. Patterns of Wallerian degeneration of myelinated fibres in short and long peripheral stumps and in isolated segments of rat phrenic nerve. Interpretation of the role of axoplasmic flow of the trophic factor. *Brain Res.* 233:227.

MacKay A, Whittall K, Adler J, Li D, Paty D, Graeb D, 1994. *In vivo* visualization of myelin water in brain by magnetic resonance. *Magn. Reson. Med.* 31, 673.

Malbouisson A M B, Ghabriel M N, Allt G, 1984. The non-directional pattern of axonal changes in Wallerian degeneration: a computer-aided morphometric analysis. *J. Anat.* 139:159.

Menon R S, Rusinko M S, Allen P S, 1992. Proton relaxation studies of water compartmentalisation in a model neurological system. *Magn. Reson. Med.* 28, 264.

Middleton W D, Kneeland J B, Kellman G M, Cates J D, Sanger J R, Jesmanowicz A, Froncisz W, Hyde J S, 1987. MR imaging of the carpal tunnel: normal anatomy and preliminary findings in the carpal tunnel syndrome. *AJR* 148:307.

Pennock J M, Rutherford M A, Cowan F M, Bydder G M, 1993. MRI: early onset of changes in Wallerian degeneration. *Clin. Rad.* 47:311.

Poon C S, Henkelman R M, 1992. Practical T_2 quantitation for clinical applications. *J. Magn. Reson. Imag.* 2:541.

Poon C S, Henkelman RM, 1993. 180° refocussing pulses which are insensitive to static and radiofrequency field inhomogeneity. *J. Magn. Reson.* 99:45.

Rosenberg Z S, Beltran J, Cheung Y Y, Ro S Y, Green S M, Lenzo S R, 1993. The elbow: MR features of nerve disorders. *Radiology.* 188:235.

Rutt B K, Mitchell J D, 1993. Myelin-selective imaging with 3D fast spin echo MRI. *Proc. of the SMRM. 12th Annual Meeting.* p. 137.

Schröder J M, 1975. Degeneration and regeneration of myelinated nerve fibres in experimental neuropathies, *in* "Peripheral Neuropathy" (P. J. Dyck, P. K. Thomas, E. H. Lambert Eds.) pp. 337-362, Saunders, Philadelphia.

Snyder R E, 1989. Loss of material from the retrograde axonal transport system in frog sciatic nerve. *J. Neurobiol.* 20:81.

Stewart W A, MacKay A L, Whittall K P, Moore G G, W, Paty D W, 1993. Spin-spin relaxation in experimental allergic encephalomyelitis. Analysis of CPMG data using a non-linear least squares method and linear inverse theory. *Magn. Reson. Med.* 29, 767.

Sunderland S, 1991. *Nerve Injuries and their Repairs*, Churchill Livingstone, Edinburgh.

Swift T J, Fritz O G Jr., 1969. A proton spin-echo study of the state of water in frog nerves. *Biophys. J.* 9:54.

Terae S, Taneichi H, Abumi K, 1993. MRI of Wallerian degeneration of the injured spinal cord. *J. Comp. Asst. Tomog.* 17:700.

Titelbaum D S, Frazier J L, Grossman R I, Joseph P M, Yu L T, Kassab E A, Hickey W F, LaRossa D, Brown M J, 1989. Wallerian degeneration and inflammation in rat peripheral nerve detected by *in vivo* MR imaging. *AJNR* 10:741.

Vasilescu V, Katona E, Simplaceanu V, Demco D, 1978. Water compartments in the myelinated nerve III. Pulsed NMR results. *Experimentia* 34:1443.

Waragai M, Watanabe H, Iwabuchi S, 1994. The somatotopic localisation of the descending cortical tract in the cerebral peduncle: a study using MRI of changes following Wallerian degeneration in the cerebral peduncle after a supratentorial vascular lesion. *Neurorad.* 36:402.

Whittall K P, MacKay A L, 1989. Quantitative interpretation of NMR relaxation data. *J. Magn. Reson.* 84:134.

Whittall K P, Bronskill M P, Henkelman R M, 1991. Investigation of analysis techniques for complicated NMR relaxation data. *J. Magn. Reson.* 95:221.

Chapter 4.
Multi-Component T_2 and MT in Peripheral Nerve‡

Introduction

Accumulating evidence suggests that the multiexponential transverse relaxation (T_2) of nervous tissue water is due to compartmentalisation. Three T_2 components have been observed in nerve (Vasilescu et al., 1978; Menon et al., 1992) and spinal cord (Stewart et al., 1993), both *in vitro* and *in vivo* (see Chapter 2), and have been identified with the myelinic, axonal, and inter-axonal water (Fenrich and Allen; 1991; Menon et al., 1992; see Chapter 3). Similar results in white matter have found two components and attributed them to myelinic and other compartments, respectively (MacKay et al., 1994). Given this supposition, it may be that other NMR signal characteristics of nerve water exhibit multiple unique components. Of interest in this paper is the longitudinal relaxation (T_1) and magnetisation transfer (MT) characteristics of each of the nerve water T_2 components.

Magnetisation transfer has been widely investigated as a contrast mechanism in neuroimaging, particularly, but not exclusively, as a means of identifying and characterising multiple sclerosis (MS) lesions. Reduction of magnetisation transfer contrast (*MTC*) (one minus the ratio of longitudinal magnetisation at steady-state with and without semi-solid pool saturation) has been found to be greater in demyelinating MS lesions than oedemous experimental allergic encephalomyelitis (EAE) ones (Dousset et al., 1992), and reduction of *MTC* has been correlated with the appearance of spectroscopic peaks believed to result from myelin breakdown (Hiele et al. 1994). From these results and others (Lexa et al. 1994; Loevner et al.; 1995, Mehta et al., 1996), it has been suggested that *MTC* decrease is primarly due to the loss of myelin and even that it may serve as a relatively specific indicator of demyelination (Hiele et al., 1994; Loevner et al., 1995). However, it has been shown that some myelinated and non-myelinated nerves have similar *MTC*s (Beaulieu and Allen, 1994) and that similar steady-state MT characteristics are exhibited by both white matter and grey matter (Morrison and Henkelman, 1995). These studies indicate that the sources of *MTC* in nerve are not restricted to myelin. Thus, the specific contributions of different anatomic compartments of nerve to its bulk *MTC* are not clear.

One investigation, which attempted to correlate the T_2 components of white matter with their respective *MTC*s found both components to exhibit similar *MTC*s over a wide range of off resonance frequencies (Harrison et al., 1995).

---

‡ A portion of this work was presented at the 3nd Annual Meeting of the Society of Magnetic Resonance, August 1995, Nice, France. Also, a version of this chapter will be submitted for publication, most likely to *Magnetic Resonance in Medicine*.

The conclusion drawn was that water mixing between the two anatomic compartments must be rapid enough to result in an effectively singular anatomic compartment over the time course of an MT measurement (several seconds). The results herein show that this assumption of a significant rate of water exchange between myelin and axons is not necessary to explain the observed similarity of myelinic and axonal *MTC*, and, moreover, not likely the primary reason for these observed *MTC* similarities. In addition, the demonstration of unique transient MT characteristics of the three nerve water T_2 components indicates that a more myelin-specific MT measurement may be achieved following a brief duration of saturation, rather than at steady-state.

METHODS

The amphibian *Xenopus laevis* (African clawed toad) was chosen as the experimental animal. The frogs were anesthetized by immersion for ≈ 30 min in a 0.1% aqueous solution of MS-222. Following anesthesia, animals were decapitated and 1-2 cm of sciatic nerve was removed from one leg and placed in a 5 mm NMR tube that contained HEPES-buffered amphibian saline, pH 7.40 (Snyder, 1989). Measurements were performed using a 3.0 T magnet and began within 60 minutes of animal sacrifice.

LONGITUDINAL RELAXATION

Longitudinal relaxation of each of the T_2 components was measured using a combination saturation recovery(SR)-CPMG (SR-CPMG) pulse sequence. The CPMG sequence used a four-step phase cycle, TE = 1.6 ms, n = 4000 echoes, and TR = 20 s. From six samples of sciatic nerve, SR-CPMG measurements were collected with 128 different saturation recovery delays ranging logarithmically between 20 ms and 10 s. Regular CPMG measures were made immediately prior to and following each set of SR-CPMG measurements in order to confirm that only SR weighting was affecting the T_2 spectra.

The SR-CPMG data was processed in two manners. Direct non-negative least-squares (NNLS) fitting of the two-dimensional data (English et al., 1991) was performed using 32-x-32 sampling of the 4000-x-128 raw data array fit to a 22-x-22 grid of T_1 and T_2 values, logarithmically spaced between 100 ms and 5 s in the T_1 direction and between 10 ms and 5 s in the T_2 direction. In addition, the NNLS fits included a term that corrects for incomplete saturation (Roscher et al., 1996), which was computed iteratively from the bulk SR data (i.e., the first echo at each SR delay setting). The sampling of the raw data and the relaxation space is limited by computational practicality. Beyond the sampling densities used, computer memory requirements surpassed the workable limit, thus preventing use of the smoothing constraint normally incorporated in fitting CPMG data.

In order to process the SR-CPMG data while using spectral smoothing, numerous raw data samples, and fitting to a large grid of T_1-T_2 values, the CPMG measurement from each SR delay must be processed separately. The data were fitted in a NNLS sense to a sum of decaying exponentials and smoothed with a minimum energy constraint (Whittall and MacKay, 1989). Following this fitting, all the resulting T_2 spectra were segmented into four domains, corresponding to the three nerve water T_2 components and the buffer component, based on the normal T_2 spectrum for the given nerve, as shown in Fig. 4.1. The signal contained in each of the four domains was summed for each SR delay value, resulting in four SR curves. Each of these curves was, in-turn, fit to a sum of recovering exponentials in a NNLS sense, thereby yielding T_1 estimates of each of the T_2 components. Again, these NNLS fits included the correcting term for incomplete saturation, as described above.

MAGNETISATION TRANSFER

From a total of 10 additional sciatic nerve samples, magnetisation transfer data from each of the three nerve water T_2 components was measured. In addition to a standard CPMG measurement (parameters as above), in each case the CPMG sequence was repeated with a preceding saturation pulse (MT-CPMG) (Harrison et al., 1995) 5 seconds in duration, (ω_1/γ=) 16.5 μT strong, and (Δ =) 10 kHz off-resonance. In four of the cases, the MT-CPMG measurements were repeated at eight different off-resonance frequencies spaced between 4.3 and 32 kHz; and in the six other cases the MT-CPMG measurements were repeated with 28 different saturation pulse durations ranging logarithmically between 20 ms and 5 s. These MT-CPMG experiments with progressively increasing durations of rf saturation result in measures of T_{1sat} as a function of T_2. As described above, each of the MT-CPMG measures was fitted in a NNLS sense to a range of decaying exponentials and smoothed with a minimum energy constraint. The resulting T_{1sat} curves, one corresponding to each of the three nerve water T_2 components, were extracted by summing the spectra over the appropriate domains.

The standard approach to modelling MT in tissue is to modify the Bloch equations to account for two spin pools that exchange longitudinal magnetisation. The steady-state solution of these equations is then modified to allow the semi-solid pool to be characterised by a different line shape, because the Lorentzian line shape which results from the Bloch equations does not accurately describe the semi-solid magnetisation (Swanson et al., 1992, Henkelman et al., 1993, Kuwata et al., 1994, Morrison and Henkelman, 1995). This modification involves replacing rf related terms with a constant rate of rf absorption (R_{rf}). This rate in the semi-solid pool (R^b_{rf}) is tailored to conform to a particular line shape, such as the super-Lorentzian line shape (Morrison and Henkelman, 1995):

$$R_{rf}^{b} = \omega_1^2 T_2^b \sqrt{2\pi} \int_0^{\pi/2} \frac{\sin\theta}{\left|3\cos^2\theta - 1\right|} \exp\left\{-2\left[\frac{2\pi\Delta T_2^b}{\left|3\cos^2\theta - 1\right|}\right]^2\right\} d\theta, \qquad [4.1]$$

where T_2^b is the T_2 value of the semi-solid pool. The use of these constant rf absorption rates, having been arrived at from the steady-state solutions, are not strictly correct during the transient response to rf. However, the semi-solid pool reaches steady-state (or, at least, quite close to steady-state) much more quickly than does the liquid pool, which allows the use of a constant R_{rf}^b when investigating the transient response of the *liquid* pool. Then, the modified Bloch equations used to approximate the transient response of the liquid pool in a two-pool MT model are (Gounot et al., 1995)

$$\begin{bmatrix} \dot{M}_x^a \\ \dot{M}_y^a \\ \dot{M}_z^a \\ \dot{M}_z^b \end{bmatrix} = \begin{bmatrix} -R_2^a M_x^a - 2\pi\Delta M_y^a \\ 2\pi\Delta M_x^a - R_2^a M_y^a - \omega_1 M_z^a \\ \omega_1 M_y^a + \left(M_0^a - M_z^a\right) R_a - R_{ab} M_z^a + R_{ba} M_z^b \\ \left(M_0^b - M_z^b\right) R_b + R_{ab} M_z^a - \left(R_{ba} + R_{rf}^b\right) M_z^b \end{bmatrix}. \qquad [4.2]$$

(N.B. Equ. [4.2] also differs from equ. [1.20] in that the phase angle, ø, is assumed to be zero). Following a few simplifications, the T_{1sat} data is fit numerically to these modified Bloch equations to provide an estimate of the rate of magnetisation exchange between the liquid and semi-solid pool (R_{ab}). Firstly, fitting a R_{ab} value requires that R_{ba}, which is significantly less influential on T_{1sat} data, is constrained. Previous MT parameter fits of nervous tissues (optic nerve, white matter, and grey matter) have found R_{ba} to be in the range of 20 s^{-1} to 32 s^{-1} (Morrison and Henkelman, 1995). For these fits R_{ba} was fixed at 20 s^{-1}. The super-Lorentzian line shape has been used successfully in fitting MT parameters of several nervous tissues while utilising T_2^b values close to 10 µs, and is, therefore, employed here with T_2^b = 10 µs to calculate R_{rf}^b (Morrison and Henkelman, 1995). Also, noting that both M_o^b/M_o^a and $(R_b - R_a^{obs})/R_a$ are normally relatively small terms, the observed longitudinal relaxation rate of the liquid pool (R_a^{obs}) is chosen as a good approximation to the intrinsic R_a because (Henkelman et al., 1993)

$$R_a \approx \frac{R_a^{obs}}{1 + \left[\frac{M_o^b}{M_o^a}\right] \frac{\left(R_b - R_a^{obs}\right)}{R_a}}, \quad \text{when } R_{ba} >> \left(R_b - R_b^{obs}\right). \qquad [4.3]$$

And, lastly, R_b is set equal to 1 s^{-1}, as was used in MT fits of several tissue types (Henkelman et al., 1993; Morrison and Henkelman, 1995). Exchange rate values, R_{ab}, are then estimated from the minimum chi-squared fit of equ. [4.2] to the average of all six T_{1ssf} curves, and uncertainties in the resultant R_{ab} were determined by adjusting the fit until the chi-squared statistic increased by one (Bevington, 1969). Given the R_{ab} and T_1 estimates, *MTC*s (= 1– M_s/M_0 at steady-state) are calculated over the range 100 Hz to 100 kHz for each of the three liquid pools present in the multi-compartment model of peripheral nerve water.

T_2 component	short-lived	intermediate	long-lived	buffer
T_2 (ms) /Fraction (see Ch. 2)	16/16%	78/48%	317/36%	>1000/ (N/A)
T_1 (ms)	80%: 435 ± 27 20%: 2325 ± 677	1192 ± 54	1819 ± 90	2159 ± 133
MTC	0.70 ± 0.06	0.69 ± .03	0.41 ± .05	0.02 ± 0.03
T_{1ssf} (ms)	146 ± 29	457 ± 34	1140 ± 78	N/A
R_{ab} (s^{-1}) †	5.00 ± 0.10	1.80 ± 0.02	0.42 ± 0.01	N/A
$T_1 R_{ab}$ ‡	2.18 ± 0.50	2.15 ± 0.05	0.76 ± 0.09	N/A

Table 4.1. Estimated values of various parameters of the two-pool model for all three T_2 components of peripheral nerve water. Uncertainties are experimental standard deviations except for R_{ab} and T_1R_{ab}.
†Uncertainties in R_{ab} values are with respect to T_{1ssf} data and do not include further uncertainty present due to the other estimated parameters.
‡Uncertainties of T_1R_{ab} reflect only the propagation of uncertainties listed for T_1 and R_{ab}.

Results

Longitudinal Relaxation

Processing the full SR-CPMG data sets by repeated T_2 spectral fitting yielded a T_2 spectrum for each SR delay setting, several of which from one nerve are shown in Fig. 4.1. The vertical bars indicate the boundaries separating the three nerve water T_2 components from each other and the buffer. Computing the area of a given component (tabulated relative to the total nerve water spectral area acquired with an SR delay of 10 s) as a function of delay value renders the saturation recovery curve for that T_2 component. In Fig. 4.2 are the SR curves from each nerve water T_2 component from one nerve, and in Fig. 4.3 are the

resulting T_1 fits of each of these SR curves. All six samples from which SR-CPMG data were measured yielded a bi-exponential T_1 of the short-lived T_2 component and mono-exponential T_1 for the other T_2 components. A tabulation (means and standard deviations) of the T_1s for each of the T_2 components is displayed in Table 4.1.

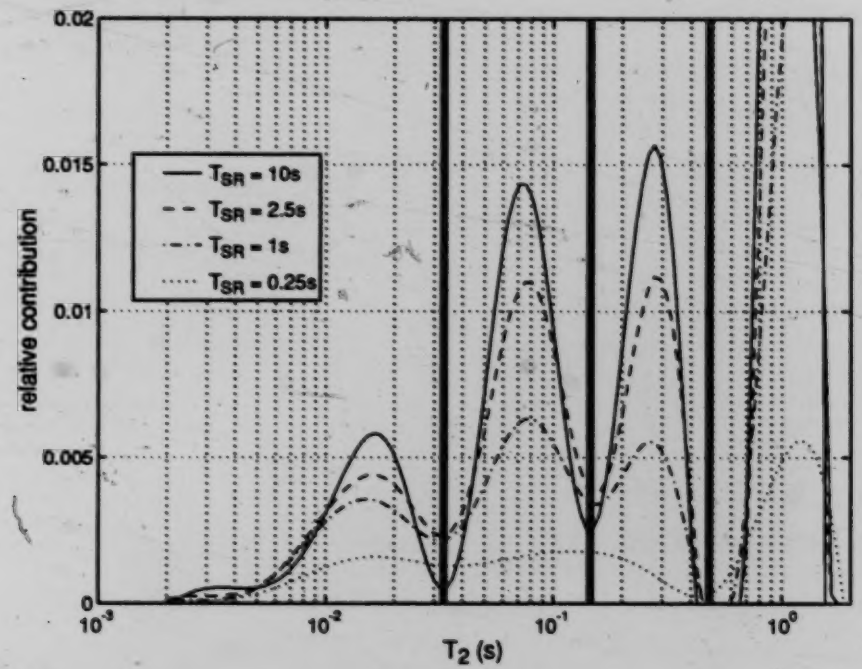

Fig. 4.1. T_2 spectra from one nerve following different SR delays in a combination SR-CPMG pulse sequence. Vertical bars indicate the separation of T_2 spectra into three nerve water components and the buffer component.

It is not possible to form such a tabulation from the direct 2-D fits of the SR-CPMG data because with the restricted sampling of T_1-T_2 space and without a smoothing constraint (particularly in the T_2 direction) the fits do not separate into well-defined components. This difficulty is demonstrated in Figs 4.4a and 4.4b which show the 2-D fits from two nerves, both of which exhibit approximately the same spectrum of T_1-T_2 components but do not separate into easily comparable components. In all six cases a similar pattern of T_1-T_2 values appeared, and in no case did a fit result in a component with relatively short T_2 (< 50 ms) having a relatively long T_1 (> 2000 ms) as resulted from the repeated 1-D fits.

MT MEASUREMENTS

Figure 4.5 shows a typical T_2 spectrum obtained from the frog sciatic nerve and the T_2 spectrum of the same nerve measured following the standard off-resonance saturation pulse. Table 4.1 gives the *MTC* value for each of the nerve water T_2 components, and in Fig. 4.6 is plotted 1–*MTC* as measured using saturation pulses of various off-resonance frequencies. This data shows that at steady-state the two shorter-lived nerve water T_2 components exhibit approximately the same *MTC* over a wide range of off-resonance frequencies, and the long-lived T_2 component exhibits a lower *MTC*. Although the steady-state *MTC*s do not differ significantly between the two shorter-lived T_2 components, all three T_2 components are seen in Fig. 4.7 to approach steady state at different rates. The results of T_{1sat} fits are listed in Table 4.1, showing widely different T_{1sat}s for each of the nerve water components, the myelin component exhibiting the most rapid approach and the inter-axonal tissue component the slowest. The R_{ab}s estimated from fitting the modified Bloch equations to the T_{1sat} curves, as well as the product of R_{ab} and T_{1sat}, are also reported in Table 4.1.

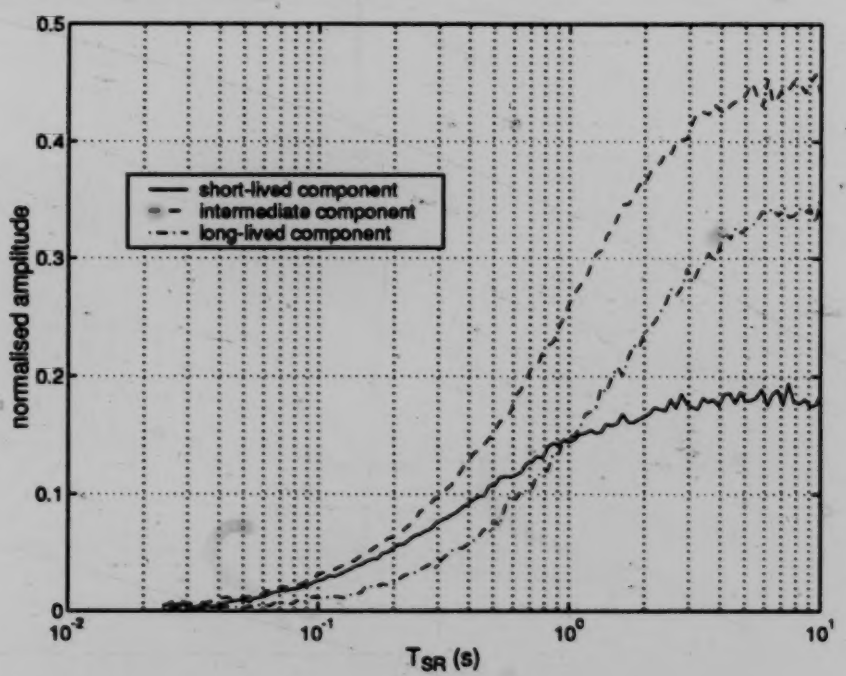

Fig. 4.2. Saturation recovery curves for each of the three nerve water components segmented from T_2 spectra as shown in Fig. 4.1.

As pointed out in the caption of Table 4.1, the uncertainties listed for the estimates of R_{ab} do not include the effect of estimating and fixing several of the other MT parameters. For example, for each T_2 component R_{ba} was fixed at 20 s^{-1}; allowing R_{ba} to range from 20 s^{-1} to 32 s^{-1} resulted in a variation of R_{ab} of approximately 8%. The R_{ab} estimates, therefore, should be considered approximate relative estimates of the three nerve water MT exchange rates, and their uncertainties, as listed in Table 4.1, serve only as an indication of numerical fit quality rather than genuine uncertainty in the value of that parameter.

Discussion

Longitudinal Relaxation

Bulk T_1 measurements of peripheral nerve (bathed in buffer) resolved into only two components (data not shown), a result that is consistent with measurements made on crayfish spinal cord and myelinated and non-myelinated garfish nerves (Menon et al., 1992). However, this appears to be a resolution limitation in which the dominating buffer signal, which has a T_1 (≈ 2100 ms) less than twice that of nerve mean T_1 (≈ 1400 ms, as measured in ref. Beaulieu, 1995), obfuscates the multiexponential nature of the nerve water. T_1 measures extracted from repeated 1-D processing of the SR-CPMG data (see Fig. 4.3 and Table 4.1) exhibit unique T_1s for each of the three nerve water T_2.

These fits also exhibit a biexponential T_1 for the short-lived T_2 component for all six nerves measured; however, the veracity of these results is questionable. Although the shorter-lived of these two T_1 components displays a plausible and reproducible T_1 (435±27 ms), the longer T_1 was astonishingly high (2325 ms) and varied widely (±677 ms). While exchange between compartments could result in one or more of the T_2 components exhibiting biexponential T_1, it could not result in a T_1 fraction from the short-lived component exhibiting a greater T_1 than any of the other two nerve compartments. Thus, it appears the long T_1 portion of the short-lived T_2 component is partially or entirely artefactual. This supposition is well-supported by the direct two-dimensional fits (Fig. 4.4): although these fits are not amenable to tabulation of relaxation rates by compartment, none exhibits a T_1-T_2 component near the presumed artefactual one found from the 1-D processing. Thus, for this discussion, the anomalous T_1 component is ignored, a simplification that amounts to neglecting approximately 3% of the total nerve water signal.

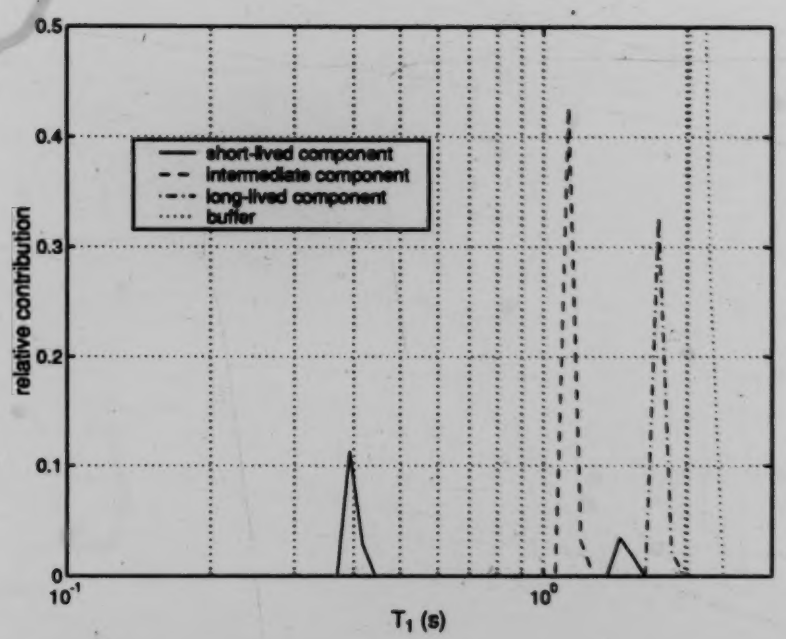

Fig. 4.3. T_1 spectra resulting from NNLS fits of each of the SR curves plotted in Fig. 4.2, corresponding to the three nerve water T_2 components, plus the T_1 spectrum resulting from the buffer's SR curve.

MAGNETISATION TRANSFER

Figure 4.5 and Table 4.1 show that the two shorter-lived T_2 components exhibit a significantly greater *MTC* than does the long-lived component, which is consistent with the assignment of the two shorter-lived components to myelin and axon associated water and the long-lived component to inter-axonal water. The fact that the two shorter-lived components did not differ significantly in *MTC* at any off-resonance frequency is not surprising in light of previous MT-CPMG measurements which showed the same phenomenon in the two T_2 components of bovine white matter (Harrison et al., 1995). However, the reason behind the similar *MTC*s of these two T_2 components is not clear.

Resulting from these aforementioned white matter measurements (Harrison et al., 1995), it was suggested that water mixing between the axon and myelin compartments is rapid enough to result in their acting as one liquid pool over the time course of a MT measurement. This was argued on the basis that two components can not exhibit identical *MTC* characteristics unless they also possess identical T_1/T_2 ratios, which is not the case with the two T_2 components

of white matter (or the two shorter-lived components of peripheral nerve). On the other hand, it can be argued that both axonal and myelinic water will display similar *MTC* characteristics, regardless of exchange, because of a finding that certain myelinated and non-myelinated nerves possess similar *MTC* characteristics (Beaulieu and Allen, 1994).

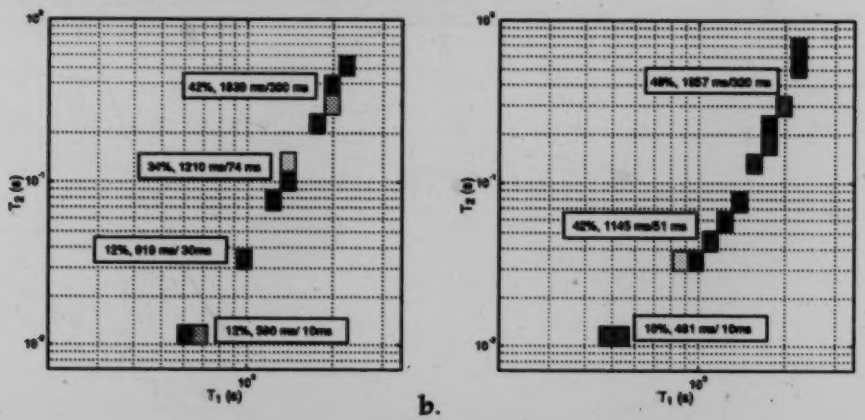

Fig. 4.4. Direct 2-D T_1-T_2 NNLS fits of SR-CPMG data from two different nerve samples (a) and (b). Shaded rectangles indicate non-zero components in the fit, darker shading corresponding to larger component amplitude. Signal fraction and mean T_1 and T_2 values are shown for groups of components. Components due to buffer are not shown and were not included in signal fraction calculation

The fact that each nerve water T_2 component exhibits a significantly different T_{1sat} strongly suggests that the MT characteristics of each T_2 component are governed by a different magnetisation exchange rate, R_{ab}. However, as referred to in a previous work, the observed *MTC* is closely related to the ratio of R_{ab} and R_a, not just R_{ab} alone (Morrison and Henkelman, 1995). Therefore, while the myelin component may posses a higher exchange rate than the axon component, its greater longitudinal relaxation rate may result in similar *MTC* characteristics. In fact, as seen in Table 4.1, the product $R_{ab} \times T_1$ is essentially identical for the axon and myelin T_2 components. Further, Fig. 4.8 shows the computed steady-state longitudinal magnetisation for each of the nerve water components given their R_{ab} and T_1 estimates. These curves, which bear a striking resemblance to corresponding curves measured from white matter (c.f. 6b in Harrison et al., 1995), demonstrate that observed *MTC*s from components with different T_1/T_2 ratios and R_{ab}s can be quite similar, all be they not identical, over a wide range of off-resonance frequencies without allowing for water exchange between the compartments.

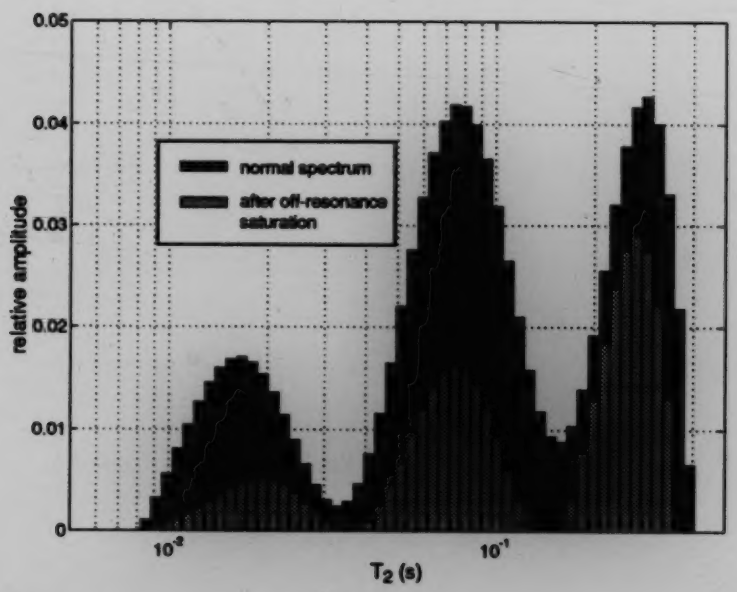

Fig. 4.5. A normal frog nerve T_2 spectrum (shaded dark) and the T_2 spectrum of the same nerve following off resonance rf saturation (shaded light). The T_2 component arising from the buffer signal is not shown.

In the scenario that two compartments have identical intrinsic liquid-pool longitudinal relaxation rates R_1s (= $1/T_2^a$) but different *MTC*s, water exchange between these compartments will tend to equalise the observed *MTC*s because each liquid pool will see some of both semi-solid pools. If the rate of water exchange is sufficiently fast compared to R_{1sat} (= $1/T_{1sat}$), the two *MTC*s will appear identical. If, on the other hand, the two compartments also possess differing intrinsic R_as, the effect of water exchange on *MTC* is not so direct because *MTC* also depends strongly on R_a. In a two compartment scenario where the intrinsic R_a is slower in the compartment with the smaller intrinsic *MTC* (which would be the case if the myelin compartment had a significantly larger *MTC* than the axon compartment, which has a significantly slower R_a), the equalising of *MTC* due to water exchange is mitigated by the effect of equalising R_as. Further, because R_{1sat} (= $1/T_{1sat}$) > R_a, the water exchange rate cannot be fast compared to R_{1sat} without also being fast compared to R_a; meaning that water exchange cannot equalise *MTC*s at a greater rate than the R_as. Thus, while water exchange may be influencing the observed *MTC* and T_1 of the axon and myelin components, it is unlikely that it is the primary reason for their apparent identical *MTC*.

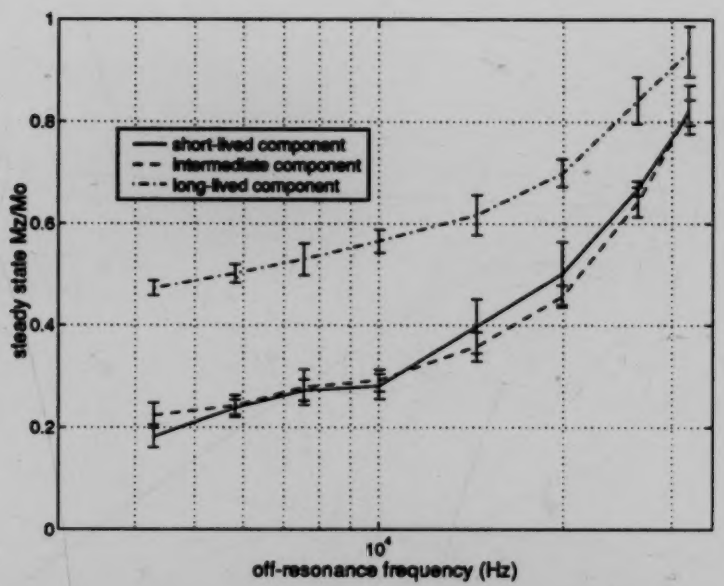

Fig. 4.6. Steady-state longitudinal magnetisation of each of the three nerve water T_2 components following rf saturation at various off resonance frequencies. Error bars indicate standard deviations.

In addition to helping elucidate the anatomic sources of nerve water *MTC*, the unique T_{1ss}s displayed in Fig. 4.5 and Table 4.1 also suggest a possible modification to standard clinical MT measurement protocol. Instead of measuring *MTC*s at steady-state, when both the myelin and axon water magnetisation has equilibrated with their respective semi-solid pools, a measurement after a brief saturating rf pulse would result in an *MTC* more dependent on the myelin component MT. This approach would also minimise any effect of water exchange between nerve water compartments.

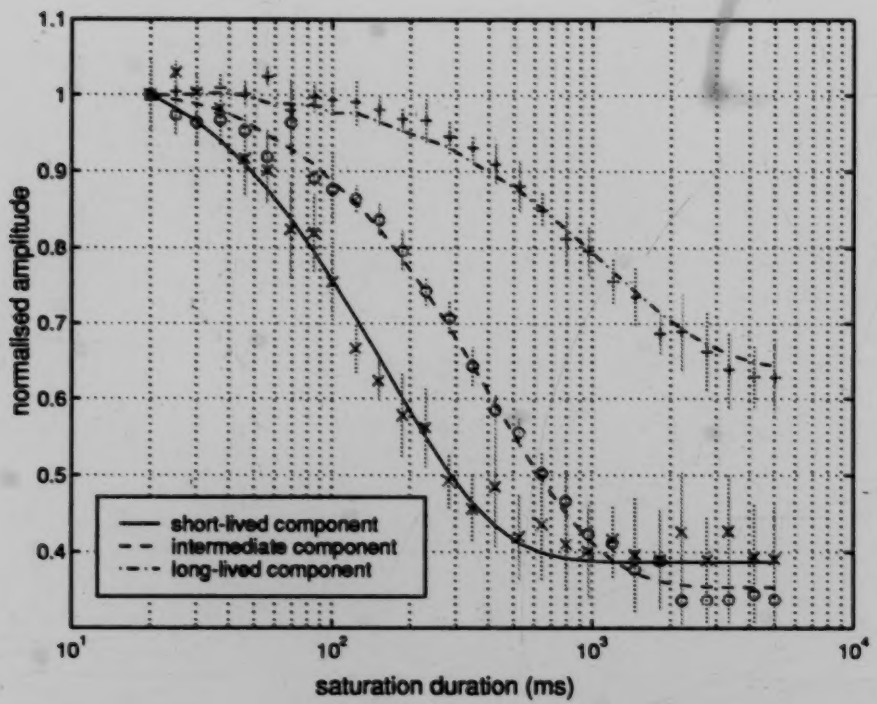

Fig. 4.7. Longitudinal magnetisation of each of the three nerve water T_2 components following off resonance rf saturation pulses of various durations (T_{1sat} data). Data points are the mean normalised values from all six nerves, and error bars are standard deviations. The continuous lines are the data resulting form the fits of R_{sat}.

Conclusion

Each of the three T_2 components of peripheral nerve water exhibit unique T_1 and MT characteristics, providing further support for the assignment of these three signal components to unique physical compartments of water. Numerical investigation of T_1 and T_{1sat} measurements of each of these three components indicates that while the two shorter-lived components exhibit similar steady-state *MTC*s, their respective MT rates are quite different. Further, simulations demonstrate that mobile water exchange between these two components is not necessary to explain their similar steady-state *MTC*s, and reasoning dictates that water exchange cannot be the primary mechanism for this similarity. Rather, the similar *MTC* of the two shorter-lived T_2 components results from differing intrinsic T_1s. In the context of the assignment of these two components to signal from myelinic and axonal water, this is to say that these two anatomic regions of nerve will exhibit similar steady-state *MTC* characteristic, despite possessing widely different MT exchange rates. Therefore,

interpreting *MTC* change to solely reflect a change in degree of myelination could lead to erroneous conclusions.

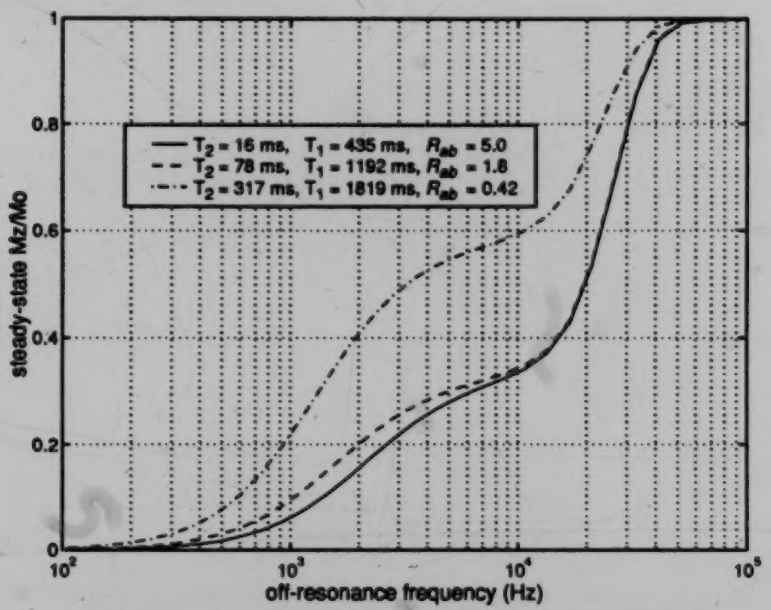

Fig. 4.8. Calculated steady-state longitudinal magnetisation of each of the three nerve water T_2 components given saturation rf at various off resonance frequencies and R_{ab}s estimated from the acquired T_{1ssf} data.

References

Beaulieu C, Allen P S, 1994. Some magnetisation transfer properties of water in myelinated and nonmyelinated nerves. *Proc. of the SMR. 2nd Annual Meeting*, p. 169.

Beaulieu C, 1995. *Diffusion and magnetisation transfer of nerve*. PhD. Thesis, University of Alberta.

Benvington P R, 1969. *Data reduction and error analysis for the physical sciences*. McGraw-Hill, New York.

Dousset V, Grossman R J, Ramer K N, Schnall M D, Young L H, Gonzalez-Scarano F, Lavi E, Cohen J A, 1992. Experimental allergic encephalomyelitis and multiple sclerosis: lesion characterisation with magnetisation transfer imaging. *Radiology* 182:483.

English A E, Whittall K P, Joy M L G, Henkelman R M, 1991. Quantitative two-dimension time correlation relaxometry. *Magn. Reson. Med.* 22:425.

Fenrich F R E, Allen P S, 1991. Transverse relaxation rate distributions for water protons in myelinated and unmyelinated nerves. *Proc. of SMRM. 10th Annual Meeting*. p. 693.

Gounot D, Mauss Y, Chambron J, 1995. Magnetisation transfer kinetics, *Proc. of the SMR. Third Scientific Meeting*. p. 1029.

Harrison R, Bronskill M J, Henkelman R M, 1995. Magnetisation transfer and T_2 relaxation components in tissue. *Magn. Reson. Med.* 33:490.

Henkelman R M, Huang X, Xiang Q-S, Stanisz G J, Swanson S D, Bronskill M J, 1993. Quantitative interpretation of magnetisation transfer. *Magn. Reson. Med.* 29:759.

Hiele J F, Lenkinski R E, Grossman R I, Dousset V, Ramer K N, Schnall M D, Cohen J A, Gonzalez-Scarano F, 1994. Correlation of spectroscopy and magnetisation transfer imaging in the evaluation of demyelinating lesions and normal appearing white matter in multiple sclerosis. *Magn. Reson. Med.* 32:285.

Kuwata K, Brocks D, Yang H, Schleich T, 1994. Relaxation-matrix formalism for rotating frame spin-lattice proton NMR relaxation in the presence of an off-resonance irradiation field. J. Magn. Reson. *J. Magn. Reson.* 104:16.

Lexa F J, Grossman R I, Rosenquist A C, 1994. MR of Wallerian degeneration in the feline visual system: characterisation by magnetisation transfer rate with histopathologic correlation. *AJNR* 15:201.

Loevner L A, Grossman R I, McGowan J C, Ramer K N, Cohen J A, 1995. Characterisation of multiple sclerosis plaques with T_1-weighted MR and quantitative magnetisation transfer. *AJNR* 16:1473.

MacKay A, Whittall K, Adler J, Li D, Paty D, Graeb D, 1994. *In vivo* visualization of myelin water in brain by magnetic resonance. *Magn. Reson. Med.* 31, 673.

Mehta R C, Pike G B, Enzmann D R, 1996. Measure of magnetisation transfer in multiple sclerosis demyelinating plaques, white matter ischemic lesions, and oedema. *AJNR* 17:1051.

Menon R S, Rusinko M S, Allen P S, 1992. Proton relaxation studies of water compartmentalisation in a model neurological system. *Magn. Reson. Med.* 28, 264.

Morrison C, Henkelman R M, 1995. A model for magnetisation transfer in tissues. *Magn. Reson. Med.* 33:475.

Rosher A, Emsley L, Roby C, 1996. The effect of imperfect saturation in saturation-recovery T_1 measurements. *J. Magn. Reson. A* 118:108.

Stewart W A, MacKay A L, Whittall K P, Moore G G, W, Paty D W, 1993. Spin-spin relaxation in experimental allergic encephalomyelitis. Analysis of CPMG data using a non-linear least squares method and linear inverse theory. *Magn. Reson. Med.* 29, 767.

Swanson S D, 1992. *Proceedings of SMRM, 11th Annual Meeting*, p. 255.

Vasilescu V, Katona E, Simplaceanu V, Demco D, 1978. Water compartments in the myelinated nerve III. Pulsed NMR results. *Experimentia* 34:1443.

Whittall K P, MacKay A L, 1989. Quantitative interpretation of NMR relaxation data. *J. Magn. Reson.* 84:134.

Chapter 5.
Multi-Echo Imaging with Sub-Optimal Spoiler Gradients[‡]

Introduction

It is often desirable to be able to measure transverse relaxation (T_2) in-vivo using a multi-echo magnetic resonance imaging protocol; however, implementing such a measurement is fraught with difficulty. Imperfections in multi-echo imaging arise due to B_1 and B_0 inhomogeneities which results in imperfect refocussing of magnetisation. Over the course of several echoes the fraction of magnetisation that does not experience the desired evolution becomes sizable and, consequently, interferes with the desired signal. The objective then of approaches to measuring T_2 accurately using a multi-echo imaging sequence is to eliminate this unwanted fraction of the signal.

One such approach is to dephase the unwanted signal using a pair of spoiler gradients centred around each rf refocussing pulse. The area of each gradient pulse must be adjusted such that unwanted magnetisation dephased by one spoiler will not be rephased by a later spoiler. Such a pattern of spoiler gradients has been developed (Crawley and Henkelman, 1987), but despite this pattern being optimised to require minimal gradient strengths most gradient hardware systems are unable to achieve the gradient strengths required in many multi-echo imaging situations, resulting in incomplete dephasing of unwanted signal. Although a modification to this spoiler pattern has been proposed for the case of sub-optimal spoiler gradient strengths (Poon and Henkelman, 1992), no quantitative investigation into the implications of using sub-optimal spoiler strengths has been published. This work demonstrates that when hardware limitations dictate the use of sub-optimal spoiler gradients, a small adjustment to the strength of the first spoiler gradient can greatly compensate for the deleterious effects of the insufficient spoiler gradients.

Spoiler Gradients

The objective of a given pattern of spoiler gradients is to suppress signal arising from selected coherence pathways. For the simple case of a rectangular, homogenous slice, the reduction of observable magnetisation due to a single slice-direction spoiler gradient pulse is a sinc function of half the gradient dephasing strength; therefore, it is ideal for all unwanted coherence pathways to experience a net dephasing of $\pm 2m\pi$ radians across the slice ($m = 1, 2, ...$) and the desired coherence pathway(s) to experience zero net dephasing (Barker

---

[‡] This work was presented in part at the 5th Annual Meeting of the Society of Magnetic Resonance, April 1997, Vancouver. Also, a version of this chapter has been submitted for publication to *Journal of Magnetic Resonance*.

and Mareci, 1989). In the case of multi-echo imaging it is desirable to preserve only the spin-echo pathway. In general, this can be achieved by placing a pair of identical spoiler gradients around each refocussing pulse. The strength of each pair must be adjusted such that no stimulated echo dephased by one spoiler gradient will be rephased by a later spoiler gradient. The pattern of spoiler gradient pairs shown in Fig. 5.1, for the case of $S_{add} = 0$, completely dephases magnetisation arising from all unwanted pathways in a multi-echo imaging sequence of NE echoes as long as the smallest spoiler strength, S_{min}, equals $\pm 2m\pi$. However, this spoiler gradient sequence requires a maximum spoiler dephasing strength of $(NE/2)*S_{min}$. When a large NE, short echo time (TE), and/or thin imaging slice is required, many gradient hardware systems are unable to achieve this maximum spoiler strength, resulting in erroneous T_2 measurements. For example, when multi-echo imaging with an echo time of 20 ms, it is unlikely to be able to use spoiler pulses longer than ≈ 4 ms in duration. Assuming a slice thickness of 5 mm and a maximum gradient amplitude of 1 Gauss/cm, the maximum spoiler could dephase no more than ≈ 17π across the slice. Therefore, for $NE > 16$ it would not be possible to completely eliminate signal from all unwanted coherence pathways.

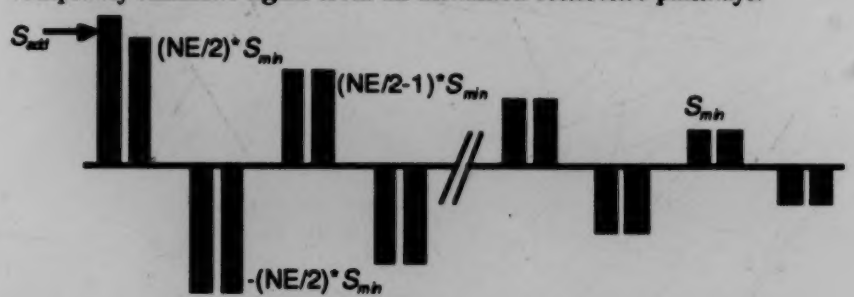

Fig. 5.1. Spoiler gradient pattern for quantitative multi-echo imaging. The grey bars depict the spoiler gradients proposed in (Poon and Henkelman, 1992), and the black bar is the addition to the first spoiler defined in the text as S_{add}.

The fact that all unwanted pathways cannot be completely eliminated, however, does not mean that the net signal from the unwanted pathways cannot be reduced to a tolerable level. For reasonably small rf pulse imperfections the vast majority of the unwanted pathways do not contribute a significant amount to the observed echo, and some of those that do will add destructively with others. In the following, it is shown using computer simulated data and experimentally acquired data that increasing the spoiler gradient prior to the first rf refocussing pulse by an additional strength S_{add} ($< 2\pi$) (Fig. 5.1) can increase the amount of mutual cancellation amongst the unwanted coherence pathways when $S_{min} < 2\pi$, thereby reducing the contamination of spin-echo data. This small adjustment to the spoiler gradient

pattern greatly reduces the maximum spoiler strength required to achieve acceptable T_2 measurements.

Methods and Results

Coherence Pathway Simulations

For a given echo in a multi-echo imaging sequence, the observed signal can be decomposed into contributions from different coherence pathways. Using the method described by Simbrunner (Simbrunner, 1994), a generalisation of earlier methods (Woessner, 1961; Kaiser et al., 1974; Shen and Saunders, 1992), the observable magnetisation at time $t = n*TE$ ($n = 1, 2, ...$) can be computed for each coherence pathway. For the eighth echo there are 750 such pathways that may contribute, and these pathways can be grouped into three categories: true-T_2, T_1-artefact, and phase-artefact (assuming the case of spin-warp imaging) (Crawley and Henkelman, 1987). The contributions from the true-T_2 and the T_1-artefact pathways add together to generate the primary image, while the signal from the phase-artefact pathway generates a ghost image. If there are phase artefacts, without a priori knowledge of the sample at both a given point in space, (x_o, y_o), and at the ghost image location, $(x_o, -y_o)$, the observed signal from that point in space cannot be predicted. For the case of the computer simulations presented, the observed signal (M_{OBS}) is defined as the sum of the signals from the true-T_2 (M_{T2}) and the T_1-artefact (M_{T1}) pathways. The phase artefact signal (M_P) is tabulated independently as an estimate of the potential ghost image contribution to the true observed signal at a given point in space.

Parameter*	Coherence Pathway	Bulk Magnetisation
NE	8	32
TE (ms)	20	20
R_1 (s^{-1})	1.0	0.5
R_2 (s^{-1})	10	5
B_1 amplitude (Hz)	333	333
B_{OFF} (Hz)	25	25
B_{MIS} (%)	5	5

Table 5.1. Parameter values used in simulations.
* *NE* = number of echoes, *TE* = echo time, R_1 = longitudinal relaxation rate, R_2 = transverse relaxation rate, B_{OFF} = offset frequency from resonance of rf refocussing pulse, B_{MIS} = amplitude missetting of rf refocussing pulse.

Coherence pathway simulations were performed using the parameters given in Table 5.1. For each value of S_{min} tested (Figs. 5.2-5.4) simulations were computed using 201 values of S_{add} equally spaced between 0 and 2π. From each set of M_{OBS} values that were generated, a T_{2OBS} was calculated using a least-squares fit to a single exponential. Figure 5.2 shows T_{2OBS} as a function of S_{add} for four values of S_{min}. The horizontal line is T_{2OBS} for the case of ideal spoiler gradients, $S_{min} = \pm 2m\pi$, a value that will henceforth be referred to as the optimal T_{2OBS}, or simply T_{2OPT}. The remaining four curves represent cases of sub-optimal spoiler gradients. From the same collection of simulations is plotted the mean fractional contribution per echo of the M_{T1} pathways to M_{OBS} as a function of S_{add} (Fig. 5.3). In Fig. 5.4 is shown the corresponding amount of M_P for each of the four cases of sub-optimal spoilers. The asterisk on each of these curves identifies the S_{add} adjustment required to minimise M_{T1} (Fig. 5.3) for that case of S_{min}.

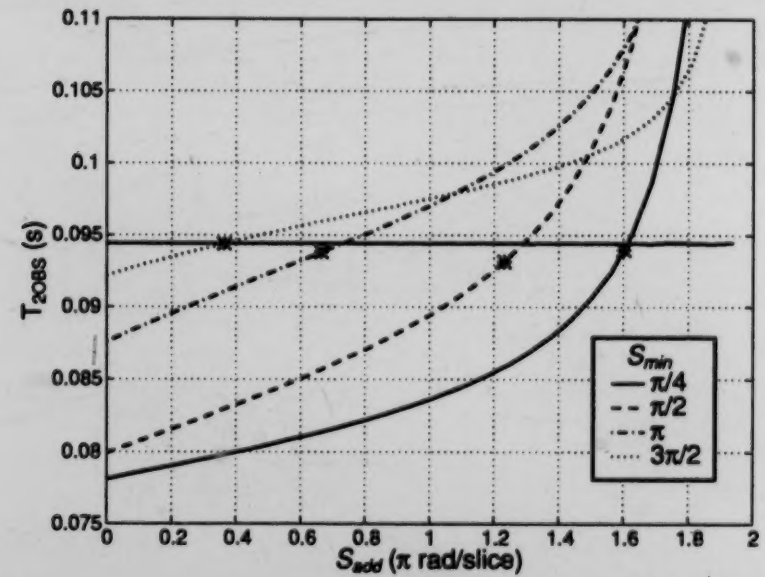

Fig. 5.2. Observed T_2s as a function of the spoiler adjustment, S_{add}, for four cases of minimum spoiler gradient strength. Horizontal solid line is T_{2OBS} for the case of ideal spoiler gradients; $S_{min} = \pm 2m\pi$ (m = 0,1,2 ...). Asterisks represents S_{add} values that result in minimal T_1-artefact corruption for corresponding S_{min} as seen in Fig. 5.3.

Figure 5.5a shows the amplitudes of all unwanted coherence pathways with magnitudes > 0.1% of the observed magnitude of the eighth echo for the case of $S_{min} = \pi$ and $S_{add} = 0$. Figure 5.5b shows the corresponding data that results when the first spoiler gradient is increased by $S_{add} = 0.7\pi$, i.e., the value of S_{add}

required to minimise M_{T1} for the case of $S_{min} = \pi$. In each plot the net magnitude of the unwanted pathways is stated as a fraction of the observed echo magnitude.

Bulk-Magnetisation Simulations

In order to investigate the effects of S_{add} under the condition of large NE, bulk-magnetisation simulations (i.e., using the Bloch equations) were employed because it is computationally impractical to perform full coherence pathway simulations for a multi-echo sequence when NE becomes large. The results of multi-echo simulations using parameters given in Table 5.1 for three spoiler gradient settings are shown in Fig. 5.6. Bulk simulations were also generated to assess the dependence of S_{add} upon missetting of the rf refocussing pulse; the results are shown in Figs. 5.7 and 5.8.

In order to assess how a given S_{add} adjustment affects the T_{2OBS} of samples with various relaxation rates, 32-echo data were simulated using three different R_2 rates, and for each of these up to five different R_1 rates. For each of these simulations $S_{min} = \pi$ and $S_{add} = 0.7\pi$. Table 5.2 shows the resulting T_{2OBS} for each of these simulations.

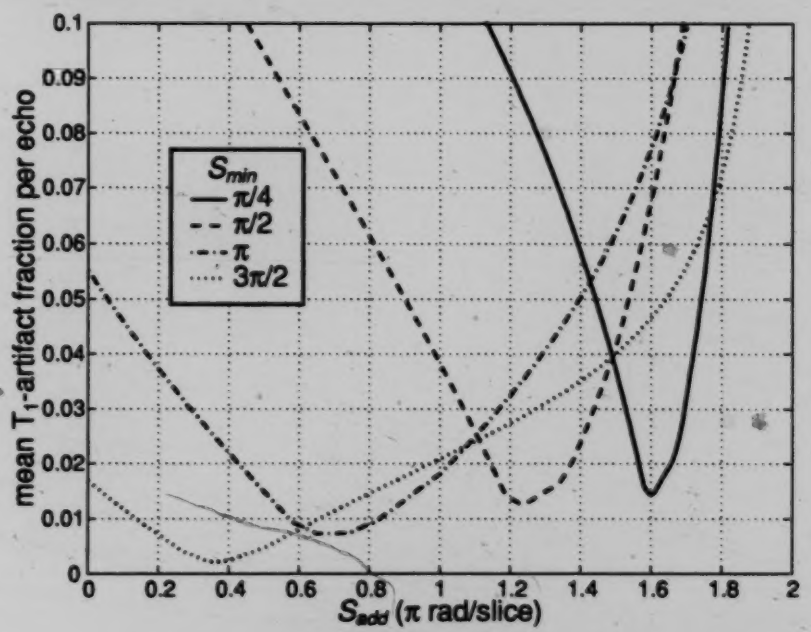

Fig. 5.3. Mean contribution per echo of magnetisation from the T_1-artefact pathways as a function of the spoiler adjustment, S_{add}, for four cases of minimum spoiler gradient strength.

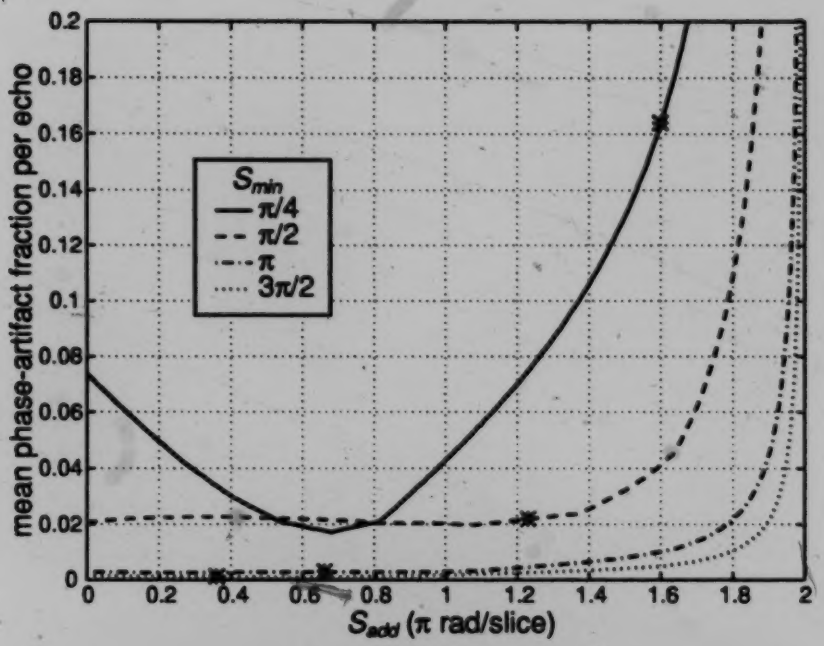

Fig. 5.4. Mean contribution per echo of magnetisation from the phase-artefact pathways as a function of the spoiler adjustment, S_{add}, for four cases of minimum spoiler gradient. Asterisks represents S_{add} values that result in minimal T_1-artefact corruption for corresponding S_{min} as seen in Fig. 5.3.

SLICE SELECTION

One factor of an imaging protocol to which S_{add} is sensitive is slice location. The above simulations were performed assuming no offset in the slice direction in which case the spoiler gradients produce no net phase shift of magnetisation. When imaging with an offset in the slice direction, a spoiler gradient imparts a net phase shift to the transverse magnetisation equal to

$$\varphi = \gamma G \Theta \tau, \qquad [5.1]$$

where G is the gradient amplitude, Θ is the slice offset, and τ is the gradient duration. In the multi-echo spoiler pattern employed here (Fig. 5.1), every spoiler gradient (prior to implementing S_{add} adjustment) has an amplitude equal to

$$G = \frac{\pm n S_{min}}{\gamma \delta \tau}, \qquad [5.2]$$

where δ is the slice thickness and n is an integer. Substituting [5.2] into [5.1] yields

$$\varphi = \frac{\pm n S_{min} \Theta}{\delta} \quad . \qquad [5.3]$$

Therefore, as long as $S_{min}\Theta/\delta = \pm 2m\pi$ ($m = 1, 2, \ldots$) no spoiler gradient will impart a non-zero net phase shift. For example, for the case of $S_{min} = \pi$, slice offsets need to be chosen as an integer multiple of twice the slice thickness. If this constraint is not met, different S_{add} values must be used to minimise the unwanted signal, and the minimal signal contribution will not be as low as otherwise found for the case of zero net phase shift. These results are demonstrated in Fig. 5.9 which shows T_1- and phase-artefact contributions to the observed signal for three cases of slice direction offset and the previously shown case of zero offset.

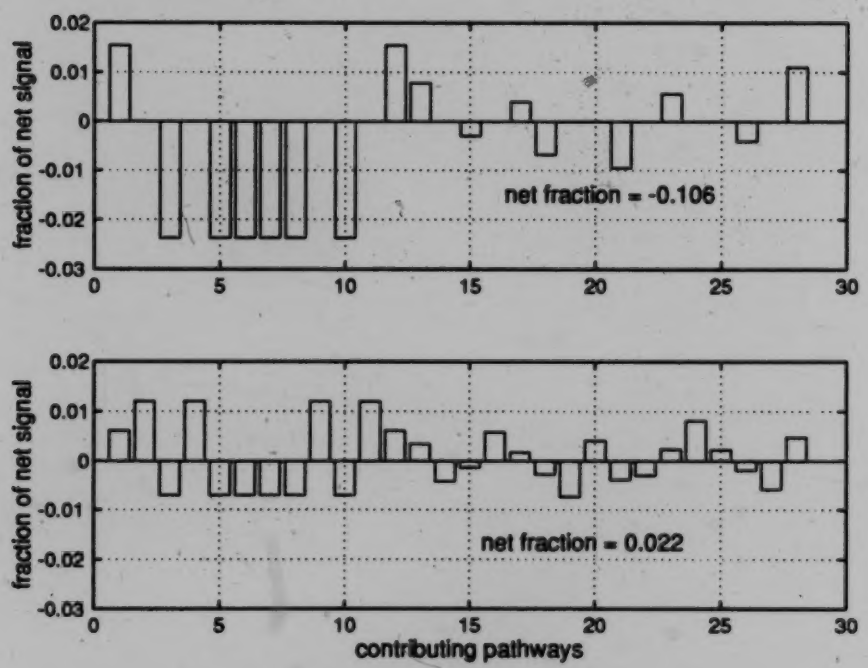

Fig. 5.5. Amplitudes of unwanted pathways contributing to the eighth echo under the condition $S_{min} = \pi$ and (a) $S_{add} = 0$, (b) $S_{add} = 0.7\pi$. Only unwanted pathways with amplitudes > 0.1% of the echo amplitude are shown.

T_2 = 163.0 ms and T_1 = 1260 ms. Eight echoes were collected using an echo time of 40 ms with B_1 intentionally misset by +5% and the resonance frequency offset by +25 Hz. Data were collected for $S_{min} = 2\pi$, π, and $\pi/2$, and for various S_{add} settings; selected results are plotted in Fig. 5.10.

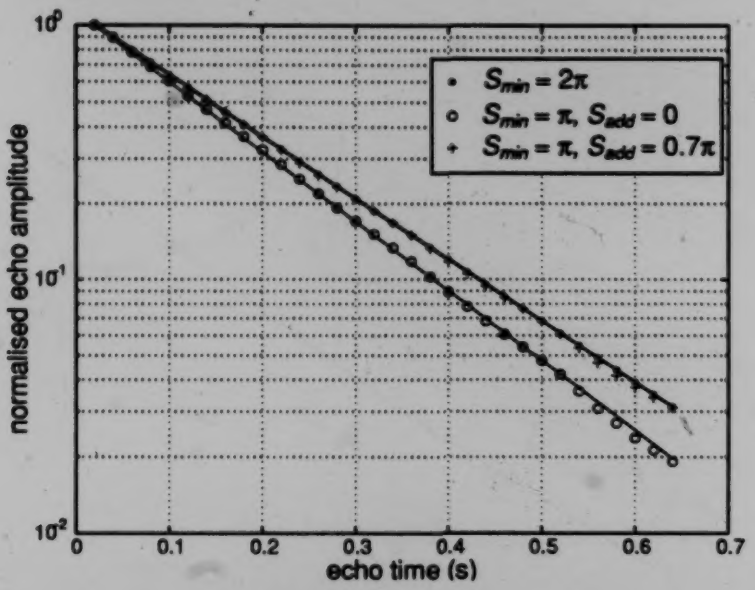

Fig. 5.6. Echo magnitudes from 32 echo bulk-magnetisation simulations using the parameters given in Table 5.1. The optimal case ($S_{min} = 2\pi$) yields a T_{2OBS} = 179.0 ms. With $S_{min} = \pi$ and no spoiler adjustment ($S_{add} = 0$) T_{2OBS} = 157.9 ms, while with the first spoiler increased by $S_{add} = 0.7\pi$, T_{2OBS} = 178.6 ms.

Discussion

Minimising Unwanted Signal

From Fig. 5.2, which demonstrates the dependence of T_{2OBS} on S_{add}, it can be seen that for the four cases of sub-optimal spoiler gradients shown there is a S_{add} adjustment that will yield T_{2OBS} equal to T_{2OPT}. However, this does not indicate that at this S_{add} adjustment one is measuring a true transverse relaxation, that is, measuring only signal arising from true-T_2 coherence pathways. Therefore, M_{OBS} is broken into M_{T2} and M_{T1}, and the relative amount of corruption from T_1-artefact pathways is plotted in Fig. 5.3. Inspection of Figs. 5.2 and 5.3 reveals that for a given value of S_{min}, the S_{add} adjustment that minimises M_{T1} relative to M_{OBS} is very near the value of S_{add} required to yield a T_{2OBS} equal to T_{2OPT}. These two values are not exactly equal

because the T_1-artefact contribution is not reduced completely to zero (Fig. 5.5b), so at the point of minimum T_1-artefact contribution there is still some contamination of M_{OBS}.

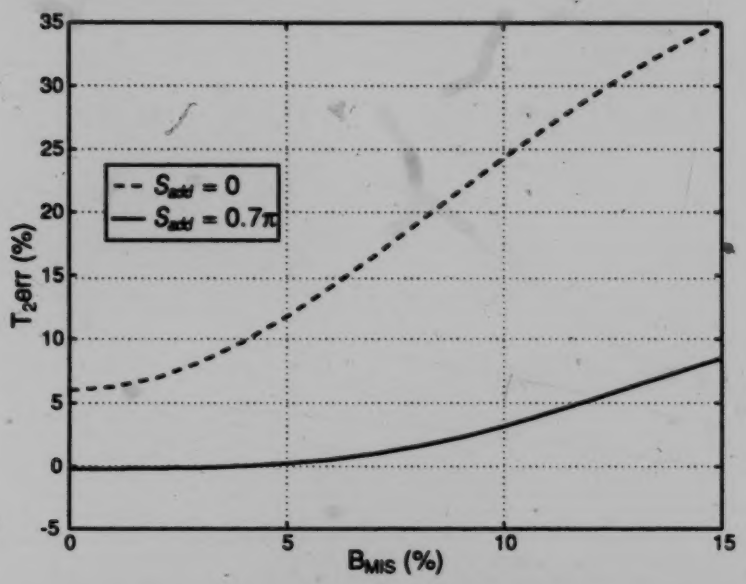

Fig. 5.7. Difference between T_{2OPT} and T_{2OBS} as a percentage of T_{2OPT} plotted as a function of amplitude missetting of the rf refocussing pulse (B_{MIS}), with the offset frequency from resonance of the rf refocussing pulse (B_{OFF}) held constant at 25 Hz.

If phase-artefacts were not a problem it would appear that even for values of S_{min} as low as $\pi/4$ an appropriate S_{add} adjustment would reduce the mean contribution of M_{T1} to < 2% per echo and result in a T_{2OBS} very near T_{2OPT} (≈1% low for $S_{min} = \pi/4$, $S_{add} = 1.6\pi$). However, in general, the observed signal will be further corrupted by the ghost image arising from phase-artefact pathways. Similar to Fig. 5.3, Fig. 5.4 shows the relative (potential) contribution of M_P to M_{OBS}. While there are S_{add} adjustments that will reduce this contribution to approximately 2% per echo in all four S_{min} cases shown, these S_{add} values do not correspond to the S_{add} values prescribed from Fig. 5.3 which are identified in Fig. 5.4 by asterisks. Figures 5.3 and 5.4 together indicate that for $S_{min} = \pi/4$ the combination of M_{T1} and M_P cannot be reduced below an average of ≈ 12% per echo, while for $S_{min} \geq \pi$, the combined corrupting contribution can be reduced to average less than 1% per echo.

The mechanism by which the corrupting signal is reduced is demonstrated in Fig. 5.5. With $S_{min} = \pi$ and no spoiler adjustment, 16 unwanted coherence

pathways are found to contribute significantly to the eighth echo and their amplitudes are plotted in Fig. 5.5a. The net signal from these 16 unwanted pathways represents 10.5% of the observed echo magnitude. With the spoiler adjustment of $S_{add} = 0.7\pi$, the number of contributing unwanted pathways jumps to 28, as shown in Fig 5.5b, but the net signal from these pathways drops to 2.2% of the observed echo because of an increased mutual cancellation of unwanted signals.

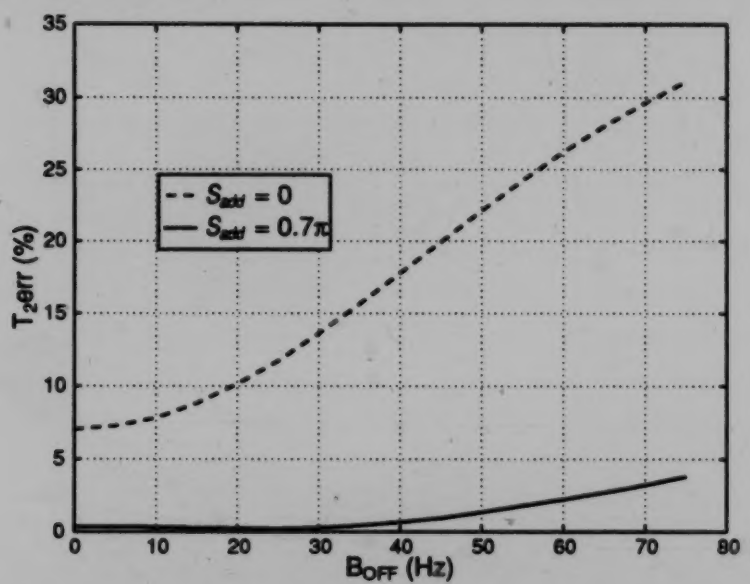

Fig. 5.8 Difference between T_{2OFF} and T_{2ON} as a percentage of T_{2OFF} plotted as a function of the offset frequency from resonance of the rf refocussing pulse (B_{OFF}), with amplitude missetting of the rf refocussing pulse (B_{MIS}) held constant at 5%.

FACTORS AFFECTING S_{add}

For relatively small NE values it is practical to perform coherence pathway simulations that will yield plots similar to those in Figs. 5.2-5.4 from which it is possible to determine the optimal S_{add} for a given imaging protocol and rf refocussing pulse imperfections. However, for large NE, due to the large number of coherence pathways, reliance must be made upon bulk simulations which cannot determine S_{add} explicitly because only M_{ONS} can be computed. If the S_{add} value required to minimise unwanted signal were sensitive to the number of echoes, determining the best S_{add} setting could prove problematic. However, as demonstrated in Fig. 5.6, this is not the case. With 32 echoes and $S_{min} = \pi$, an S_{add} value of 0.7π, the same value that was used with $NE = 8$,

results in echo magnitudes very close to those resulting from the optimal case of $S_{min} = 2\pi$. Also, as seen in Table 5.2, results from simulations using the same spoiler setting showed that over a wide range of biologically relevant R_1 and R_2 values T_{2OBS} was very near T_{2OPT}, suggesting a near maximal reduction of net signal from unwanted coherence pathways. Therefore, the best S_{add} value for a given multi-echo imaging protocol does not appear to be particularly sensitive to *NE* or relaxation rates.

	T_2 (ms)	T_2 (ms)	T_2 (ms)
True T_2	300.0	100.0	40.0
T_{2OPT}	255.0	94.5	39.1
R_1 (s^{-1})	T_{2OBS} (ms)	T_{2OBS} (ms)	T_{2OBS} (ms)
0	253.7	94.6	38.9
1	253.3	94.5	38.9
3.33	252.5	94.3	38.9
10	–	94.0	38.9
25	–	–	38.9
Range	0.47%	0.32%	0.00%

Table 5.2. Observed T_2s from 32 echo simulations using a range of R_1 and R_2 values.

The sensitivity of S_{add} to B_{OFF} and B_{MIS} is another potential problem to implementing an S_{add} adjustment. Knowing the characteristics of the rf coil and the refocussing pulse being used will provide an estimate of the potential B_{MIS}, as will the line width provide an estimate of the effective B_{OFF}, but in practice it is impossible to know precisely B_{OFF} and B_{MIS}, particularly as they vary spatially. If a composite refocussing pulse is used, one might expect as little as ≈ 5% variation in effective B_1 amplitude throughout a volume (Poon and Henkelman, 1993). Fig. 5.7 indicates that with up to ±5% missetting of B_1 (given B_{OFF} = 25 Hz) there is virtually no additional cost in using sub-optimal spoiler gradients with the S_{add} adjustment. This does not mean that T_{2OBS} will not vary over a ±5% range of B_{MIS}, but only that over such a range T_{2OBS} will remain as accurate as possible (i.e., ≈ T_{2OPT}) given the particular B_{MIS}. For comparison, also shown in Fig. 5.7 is the corresponding T_2 error when sub-optimal spoilers are implemented without the adjustment which demonstrates a much greater sensitivity to B_{MIS}. Similar results for the case of B_{OFF} variation (given B_{MIS} = 5%) are plotted in Fig. 5.8. Thus, for a reasonably wide range of B_{MIS} and B_{OFF} values it is expected that near optimal T_2 values can be measured

using the appropriate S_{add} adjustment determined from coherence pathway simulations.

It should be noted, however, that the sensitivity of S_{add} to rf inaccuracies becomes significantly greater with decreasing S_{min} values. This is due to the fact that the M_{T1} minima (Fig. 5.3) become much narrower with decreasing S_{min} which results in the increasing slopes of the T_{2OBS} curves seen in Fig. 5.2. Thus, at lower settings of S_{min}, small missettings of S_{add} will result in greater increases in M_{T1} contribution to the echo and, in turn, greater difference between T_{2OBS} and T_{2OPT}.

Finally, one must consider the signal-to-noise cost of implementing the S_{add} adjustment, because, while providing additional dephasing to unwanted pathways, S_{add} is also dephasing the desired signal. For $S_{add} = 1.2\pi$, which would be required for the case of $S_{min} = \pi/2$, approximately 50% of the observed signal is lost. This value drops significantly, however, to less than 20% when S_{add} is reduced to 0.7π, corresponding to the case of $S_{min} = \pi$. In most situations, a 20% signal loss is probably a tolerable cost for reducing gradient demands by nearly a factor of two.

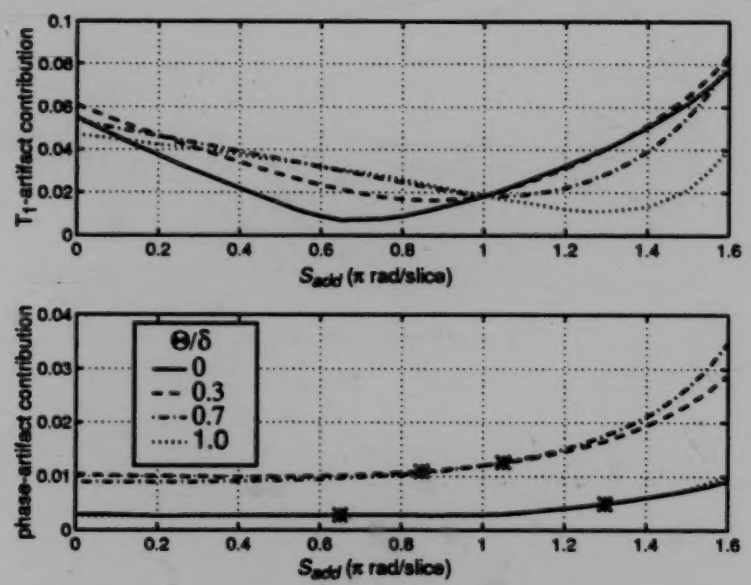

Fig. 5.9 Mean contribution per echo of magnetisation from the T_1- and phase-artefact pathways as a function of the spoiler adjustment, S_{add}, for $S_{min} = \pi$ and four cases of slice offset (Θ) divided by slice thickness (δ).

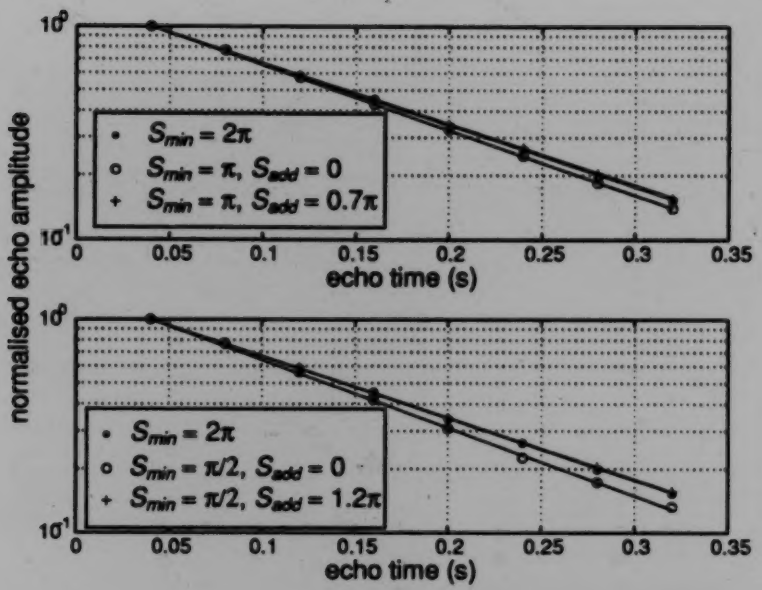

Fig. 5.10. MRI echo magnitudes from 8 echo acquisitions. The optimal case ($S_{min} = 2\pi$) yields a $T_{2OBS} = 150.1$ ms, compared to the spectroscopically measured value of 163.0 ms. With $S_{min} = \pi$ (a) and no spoiler adjustment ($S_{add} = 0$) $T_{2OBS} = 142.6$ ms, while with the first spoiler increased by $S_{add} = 0.7\pi$ $T_{2OBS} = 151.5$ ms. With $S_{min} = \pi/2$ (b) and no spoiler adjustment ($S_{add} = 0$) $T_{2OBS} = 136.8$ ms, while with the first spoiler increased by $S_{add} = 1.2\pi$ $T_{2OBS} = 150.9$ ms.

CONCLUSION

Using computer simulations and experimental data we have demonstrated that when sub-optimal spoiler gradients of $S_{min} \geq \pi/2$ are used in multi-echo imaging sequences designed to measure T_2, increasing the strength of the first spoiler gradient by the appropriate amount reduces the contamination from unwanted coherence pathways by a factor of several times. With this reduction of corrupting signal, ensuing T_2 measurements are typically within 1% of those obtained using optimal spoiler gradient strengths. With $NE = 8$, the use of the sub-optimal spoiler gradient of $S_{min} = \pi/2$ along with an appropriate adjustment gradient S_{add} reduces the maximum spoiler gradient strength required by ≈ 60%, this value approaching 75% with increasing NE. Correction for values of $S_{min} < \pi/2$ are restricted by the ghost image that arises from phase-artefact pathways. Coherence pathway simulations have shown that the effect of the additional spoiler gradient S_{add} is to cause an increase in mutual cancellation of unwanted signals arising from deleterious coherence pathways.

Computer simulations have shown that the optimal adjustment S_{adj} for a given sub-optimal gradient strength does not depend significantly upon R_1 and R_2 relaxation times or upon a reasonably wide range of rf refocussing pulse missetings. However, the sensitivity of S_{adj} to rf inaccuracies increases with decreasing values of S_{min}. As well, the ability of the S_{adj} adjustment to reduce unwanted signal is sensitive to the slice location, being optimal for slices in which each unadjusted spoiler gradient produces a net phase shift of $\pm 2m\pi$ ($m = 1, 2, \ldots$).

References

Barker G J, Mareci T H, 1989. Suppression of artefacts in multiple-echo magnetic resonance. *J. Magn. Reson.* 83, 11.

Crawley A P, Henkelman R M, 1987. Errors in T_2 estimation using multislice multiple-echo imaging. *Magn. Reson. Med.* 4:34.

Kaiser R, Bartholdi E, Ernst R R, 1974. Diffusion and field-gradient effects in NMR Fourier spectroscopy. *J. Chem. Phys.* 60:2966.

Poon C S, Henkelman R M, 1992. Practical T_2 quantitation for clinical applications. *J. Magn. Reson. Imag.* 2:541.

Poon C S, Henkelman RM, 1993. 180° refocussing pulses which are insensitive to static and radiofrequency field inhomogeneity. *J. Magn. Reson.* 99:45.

Shen J. F., Saunders J. K., 1992. A slice-selective adiabatic refocussing pulse made up of two adiabatic inversion pulses. Suppression of unwanted echoes. *J. Magn. Reson.* 96:381.

Simbrunner J, 1994. Generalization of the partition method for calculating echo magnitudes. *J. Magn. Reson. A.* 109:117.

Woessner D E, 1961. Effects of diffusion in nuclear magnetic resonance spin-echo experiments. *J. Chem. Phys.* 34:2057.

Chapter 6. Closing Comments

The scientific investigations discussed within this thesis serve to advance the understanding of peripheral nerve water NMR signal characteristics and methods of their measurement in a quantitative manner. The intent with which these investigations were undertaken was to contribute to a research programme aimed towards understanding how various NMR tissue characteristics can serve to differentiate between various pathophysiologic states of nerve and how these characteristics can be measured *in vivo* using MRI. In particular, four studies have been expounded in this thesis, each contributing to the goals of the research programme in their own way.

The central basis of all the work within this thesis is that peripheral nerve water exists in three broadly unique environments—myelinic, intra-axonal, and extra-axonal. In the first study (Chapter 2) presented within this thesis, the premise that each of these environments exhibits unique transverse relaxation rates is used as the basis to generate improved nerve-muscle contrast and as a motivation to measure these rates *in vivo*. Using a multi-echo imaging sequence designed to generate uncorrupted echo trains, three T_2-relaxation components were measured in peripheral nerve *in vivo*, including a long-lived component ($T_2 > 200$ ms) which previously had only been identified *in vitro*. The existence of a long-lived T_2-relaxation component indicated echo times as long as 200-300 ms may provide maximal *CNR* (nerve to muscle) in T_2-weighted images. Averaging selected images from the multi-echo image set, the *CNR* was increased by a factor of nearly three.

Based on the hypothesis that each of the three nerve water T_2s measured in the prior study are derived from unique microanatomic compartments, the second study (Chapter 3) used the imaging methodology investigated in the prior study in an attempt to measure changes in peripheral nerve water T_2-relaxation during the process of Wallerian degeneration. Multi-echo imaging and *in-vitro* methods showed progressive changes in the T_2-relaxation spectra of frog sciatic nerve undergoing Wallerian degeneration. The two most apparent changes as degeneration progressed were a reduction from three well-resolved T_2 components to one and a decline in the fraction of the spectra associated with the short-lived T_2 component which is thought to arise from myelinic water. The former change appears to reflect a collapse of myelinated fibres, while the latter a combination of interstitial oedema and myelin loss.

Given the evidence that the multi-exponential nature of peripheral nerve water arises from microanatomic compartmentalisation, the objective of the third study was to investigate whether these compartments also exhibit unique T_1 and MT characteristics. This study was of particular interest given the conflicting information previously published regarding the role of myelin in generating MT contrast in nerve. In fact, it was found that each of the three T_2

components of peripheral nerve water exhibited unique T_1 and MT characteristics. Numerical investigation of T_1 and T_{1ss} measurements of each of these three components indicated that while the two shorter-lived components exhibited similar steady-state *MTC*s, their respective MT rates were quite different. Further, simulations demonstrated that mobile water exchange between these two components was not necessary to explain their similar steady-state *MTC*s, and reasoning dictated that water exchange cannot be the primary mechanism for this similarity. Rather, the similar *MTC* of the two shorter-lived T_2 components results from differing intrinsic T_1s. In the context of the assignment of these two components to signal from myelinic and axonal water, this is to say that these two anatomic regions of nerve exhibit similar steady-state *MTC* characteristic, despite possessing widely different MT exchange rates. Therefore, interpreting *MTC* change to solely reflect a change in degree of myelination could lead to erroneous conclusions.

Finally, the fourth study was geared at improving quantitation of multi-exponential transverse relaxation *in vivo*. In practice, this quantitation requires the use of spoiler gradients, which, in many clinical situations, are not strong enough to produce optimal measurements. Using computer simulations and experimental data it was demonstrated that when using sub-optimal spoiler gradients, increasing the strength of the first spoiler gradient by the appropriate amount reduces the contamination from unwanted coherence pathways by a factor of several times, resulting in T_2 measurements within 1% of those obtained using optimal spoiler gradient strengths. Use of this spoiler gradient adjustment effectively reduces the peak spoiler gradient requirement by a factor of 2-4.

In closing, it should be pointed out that drinks and food are being served in the reception room next door.

Appendix I
MATLAB™ Programs

WARNING/DISCLAIMER

Using any of the following programs blindly is strongly advised against. None have been written for general use and, therefore, require specific knowledge of the processes involved for reliable and accurate implementation. All of the following programs have been modified many times throughout the course of use, and there are no guarantees that the form below will produce the results anticipated from reading the body of this thesis.

These programs are, however, a worthwhile reference for anyone planning to generate similar MATLAB programs on their own. And, for such people, I will always be happy to clarify any confusion regarding the code below.

T_2 PROCESSING

Chapters 2, 3, and 4 all contain multi-echo data that has been processed by fitting echo amplitudes in a non-negative least-squares sense to the sum of a wide range of decaying exponential functions. The program shown below is set for processing in-vitro measured data which has 4000 echoes and high enough SNR to warrant the use of a spectral smoothing constraint. In-vivo measured (i.e., from images) data, uses a similar program with some obvious parameter changes and without the smoothing constraint (section identified below). Also, a slight variation in this program altering the matrix of decaying exponentials (variable 'A' below) into a matrix of recovering exponential and including a term for incomplete saturation makes it suitable for fitting multi-exponential T_1 data.

```
function [S,Ss,X,c,cs,T,lSi] = T2procNLS(D);
%function [S,Ss,X,c,cs,T,lSi] = T2procNLS(D);

TE = 1.6e-3;  % echo time
K = 96;       %number of spectral components
N = 128;      %number of echoes extracted from raw data
sp = fix(logspace(log10(20),log10(3997),N))-18;  %indices of extracted echoes
l = length(sp);
D = D(sp)';
D = D/max(D);
ts = TE*round(sp)';    %times of extracted echoes
T = [logspace(log10(3.2e-3),log10(3),K)];   %spectral space
R = 1./T;
A = ts *R;
A = exp(-A);
A = [A,ones(l,1)];      %matrix of decaying exponentials
Si = nnls(A,D);%initial fit
Pi = A*Si;              %predicted data
lSi = length(find(Si));
```

```
[X,chi] = uncert(Pi,D,lSi);      %returns uncertainties

for k = 1:l                %normalises fitting to uncertainties
Dm(k) = D(k)./X(k);
Am(k,:) = A(k,:)/X(k);
end
Ams = Am;

Dm = Dm';
Dms = Dm;
to = clock;,S = nnls(Am,Dm);,etime(clock,to)      %normalised fit
P = A*S;
R = P-D;        %residuals
c = sum(R.^2 ./ X.^2);        %chi-squared statistic
S = S(1:K);
%return at this point is no spectral smoothing is employed
cs = 170;
mu = 150     %set starting smoothing weighting
C = N+sqrt(2*N);      %objective chi-squared statistic
while cs>C

mu = mu-max([((cs-C)*0.60),1]);

Am = [Ams;eye(K+1,K+1)*(mu)];
Dm = [Dms;zeros(K+1,1)];
to=clock;,Ss = nnls(Am,Dm);,etime(clock,to)          %smoothed fit
Ps = A*Ss;
R = Ps-D;
cs = sum(R.^2 ./ X.^2);      %new chi-squared statistic
%cs = chisq(ch,l-lSi)
disp([cs,mu])
end
Ss = Ss(1:K);
return
```

2D PROCESSING

For the direct 2D-processing of the SR-CPMG data discussed in Chapter 4, the following routine was used, which is a modification of the above program.

```
function [Si,T1,T2,S,X,P,D,c] = T2procN(B,D,lspace,K1,K2);
%function [Si,T1,T2,S,X,P,D,c] = T2procN(B,D,lspace,K1,K2);
% Fitting space dimesions are passed in as variables K1 and K2
Tmul = 1;
TE = 1.6e-3;  %echo time
N2 = 32;      %number of samples in T1 direction
N1 = 32;      %numbert of samples in T2 direction
sp = fix(logspace(log10(4),log10(3980),N2))-2; %sample indices in T2
direction
spi = fix(linspace(4,128,N1));        %sample indices in T1 direction

D = D(sp,spi);
D = D(:);
D = D/max(D);
ts = TE*sp';
%Fitting spaces in T1 and T2 directions
T2 = [logspace(log10(10e-3),log10(3),K2)];
T1 = [logspace(log10(250e-3),log10(3),K1)];

[r,c] = find(ones(K2,K1)==1);
for kk = 1:length(spi)
for k = 1:length(sp)
%Fitting matrix, including 'B' term for incomplete saturation
A((kk-1)*length(sp)+k,:) = exp(-ts(k)./T2(r)).*[1-B*exp(-
lspace(spi(kk))./T1(c))];
end
end
Si = nnls(A,D);
Pi = A*Si;
disp('finished first fit')
Dm = reshape(D,N2,N1);
Pm = reshape(Pi,N2,N1);
[X,chi] = uncert2D(Pm,Dm);

clear Dm Pm
for k = 1:N2*N1
Dm(k) = D(k)./X(k);
Am(k,:) = A(k,:)/X(k);
end

Dm = Dm';
to = clock;,S = nnls(Am,Dm);,etime(clock,to)
P = A*S;
R = P-D;
c = sum(R.^2 ./ X.^2);
return
```

six pools, coressponding to three nerve water compartments and their respective semi-solid pools.

```
%Fixed Rf rates for semi-solid pools
Rrfb = 1*130.8753;,Rrfd = 1*130.8753;,Rrff = 1*130.8753;
dw = 1*10000*2*pi; %off-resonance frequency
w1 = 1*16.5e-6*gam*10000;                    %Sat pulse strength
%Pool sizes at equilibrium
Moa = .16;
Mob = Moa*0.2497*1.46;
Moc = .48;
Mod = Moc*0.0909/3;
Moe = 0.36;
Mof = Moe*0.0210;
Mo = [Moa Mob 0 0 Moc Mod 0 0 Moe Mof 0 0]';

%Relaxation rates
R2a = 1/16e-3;,R2c = 1/78e-3;, R2e = 1/317e-3;
R1a = 1/435e-3;, R1b = 1;
R1c = 1/1.192;,R1d = 1;
R1e = 1/1.819;,R1f = 1;
%MT rates
R1 =  20;
R2 =  20;
R3 =  20;
Rab = R1*Mob/Moa;
Rba = Rab*Moa/Mob;
Rcd = R2*Mod/Moc;
Rdc = Rcd*Moc/Mod;
Ref = R3*Mof/Moe;
Rfe = Ref*Moe/Mof;

%Water exchange rates
R4 = 0;
R5 = 0;
Rac = R4*Moc/Moa;
Rca = Rac*Moa/Moc;
Rae = R5*Moe/Moa;
Rea = Rae*Moa/Moe;

%Set up MT-modified Bloch equs in matrix form

A11 = [ -(R1a+Rab+Rac+Rae)      Rba    0       w1;
        Rab    -(R1b+Rba+Rrfb)          0       0 ;
        0              0       -(R2a+Rac+Rae) -dw;
        -w1            0       dw    -(R2a+Rac+Rae)];

A12 = [Rca    0       0       0;
       0      0       0       0;
       0      0       Rca     0;
       0      0       0       Rca];
```

```
A13 = [Rea   0     0     0;
       0     0     0     0;
       0     0     Rea   0;
       0     0     0     Rea];

A21 = [Rac   0     0     0;
       0     0     0     0;
       0     0     Rac   0;
       0     0     0     Rac];

A22 = [ -(R1c+Rcd+Rca)    Rdc              0      w1;
        Rcd    -(R1d+Rdc+Rrfd)             0      0 ;
        0              0      -(R2c+Rca)   -dw;
        -w1            0              dw   -(R2c+Rca)];

A23 = zeros(4,4);

A31 = [Rae   0     0     0;
       0     0     0     0;
       0     0     Rae   0;
       0     0     0     Rae];

A32 = zeros(4,4);

A33 = [ -(R1e+Ref+Rea)    Rfe              0      w1;
        Ref    -(R1f+Rfe+Rrff)             0      0 ;
        0              0      -(R2e+Rea)   -dw;
        -w1            0              dw   -(R2e+Rea)];


A = [A11,A12,A13;A21,A22,A23;A31,A32,A33];
C1 = [ R1a*Moa; R1b*Mob; 0;0];
C2 = [ R1c*Moc; R1d*Mod; 0;0];
C3 = [ R1e*Moe; R1f*Mof; 0;0];
C = [C1;C2;C3];

Mst(:,k) = inv(A)*(-C);
%Mst(:,1) = inv(A)*(-C);
return                  %end here if only interested in steady-state solutions

% Transient solutions by eigenvectors
[K,D] = eig(A);
X = inv(K)*(Mo-Mst);
F = K .* [X';X';X';X';X';X';X';X';X';X';X';X'];
[th,r] = cart2pol(real(F),imag(F));
F = r.*sign(cos(th));

M = F*exp(diag(D)*t)+Mst*ones(size(t));
return %return here if only interested in a particular solution
% continue if computation of error, if function is used for fitting

Mn = real(M(1,:))/real(M(1,1));
res = Mn-za;
er = sum(res.^2./si.^2);
return
```

MULTI-ECHO SIMULATIONS BY COHERENCE PATHWAY

%MEscript.m

```
%Root script file for running ME simulations of coherence pathwasy
SliceThickness = 1.0; %units of cm
Slo = 0; %2cm
%NE = 8; %Number of Echoes
NE = 8;
TE = 20e-3; %Echo Time
tspace = [TE:TE:NE*TE]';
TE2 = TE/2;
Tsp = 3e-3;
R1 = 1;, R2 = 10;
B1 = 1.05;     %180 pulse tip angle/180
phi = pi/2;    %180 pulse phase angle
BoffH = 25;    %180 pulse off-resonance frequency (Hz)
Boff = BoffH*2*pi/gam
Gspmin = 1.0;          %Minimum spoiler amplitude (Smin in text)
Bnom = pi/(1.500e-3*gam);%180 pulse strenth
alpha = atan(Boff/Bnom);
Gslice = 2*2*pi*750/(gam*SliceThickness);
%compute  rotation matrix and f terms for excitation
[f1,R] = RotationMf(0,0,pi/2);
%compute  rotation matrix and f terms for 180 pulse
[f,R] = RotationMf(alpha,phi,pi*B1);
%GESpace = [0.0:0.7:1.];
GESpace = 0.7;         %additional spoiler (Sadd in text)
lG = length(GESpace);
%gp = [-5 5 -4 4 -3 3 -2 2 -1 1]*Gspmin;
%spoiler pattern
gp= -1*[ -4 4 -3 3 -2 2 -1 1]*Gspmin;

MTTh = zeros(NE,lG);

for N = 1:NE
gps = gp(1:N);
gpm = [0 gps] + [gps 0];

clear Mt Mraw
%call pathway caculation function for each echo
MEpathSF

for kR = 1:lG
%disp(kR)
GE = GESpace(kR);
g = gpm;, g(1) = gpm(1) + GE;
ø = g*PP;
Ω=ø*pi*Slo/SliceThickness;

%compute dephasing and phase shift due to spoilers, for each Sadd value
Mt(:,kR) = (Mraw.*sinc(ø/2).*exp(-i*Ω))';
end

Mt = [Mt;zeros(2,lG)];
```

```
%determine indices of different pathway categories
[mx,Ip] = max(abs(Mt(:,1)));
Ig = find(sum(abs(PP))==N+1);
Ih = find(rem(N+2-sum(abs(PP)),2)==0);
It = find((rem(N+2-sum(abs(PP)),2)~=0)&sum(abs(PP))<N+1);

[Il,dummy] = size(Mt);
MTTp(N,:) = Mt(Ip,:);
MRWp(N) = Mraw(Ip);

%compute transverse magnetisation fromeach pathways group.
MTT(N,:) = sum(Mt);
MTTg(N,:) = sum(Mt([Ig,Il,Il-1],:));
MTTh(N,:) = sum(Mt([Ih,Il,Il-1],:));
MRWh(N) = sum(Mraw(Ih));
MTTt(N,:) = sum(Mt([It,Il,Il-1],:));
MRWt(N) = sum(Mraw(It));
MTTo(N,:) = sum(Mt([Ig,It,Il,Il-1],:));

end

%compute echo amplitudes by group, if necessary.
Et = abs(MTT);
Etg = abs(MTTg);
Etp = abs(MTTp);
Ett = abs(MTTt);
Eth = abs(MTTh);
Eto = abs(MTTo);
Rp = MTTp./(MRWp'*ones(1,lG));
Rt = MTTt./(MRWt'*ones(1,lG));
Rh = MTTh./(MRWh'*ones(1,lG));

clear P
return
```

```
% MEpathSF.m
%builp pathways matrix unless or load a pre-calculated one
%PP = buildP(N);
eval(['load Ppath',int2str(N)])
PP = P;, clear P
%row 1 is P1, row N is Pn
%P1 = ± 1, Pn = 1
 [r,c] = size(PP);
for k = 1:c
P = PP(:,k);
%compute magnetisation passes along pathway due to rf pulses
M = buildf(P,f,f1);
n = 1;
%compute effect  of T2 and T1
M = M*exp(-abs(P(n))*TE2*R2)*exp((abs(P(n))-1)*TE2*R1);
 for n = 2:r-1
  M = M*exp(-abs(P(n))*TE*R2)*exp((abs(P(n))-1)*TE*R1);
 end
Mraw(k) = M*exp(-i*0-TE2*R2);
end
return
**********
function P = buildP(N);
%function P = buildP(N);
%BuildP.m builds P, a matrix of possible pathway vectors,
%given a number of echoes, N
%if N > 8, return, end
P = ones(N+1,2*3^(N-1));
[r,c] = size(P);
%build row P1 = - 1
lc = c/2;
P(1,lc+1:2*lc) = -1*ones(1,lc);
%build rows 2 through N
% row N+1 remains all 1
for k = 2:N;
lc = c/2/(3^(k-1));
zc = zeros(1,lc);
nc = -1*ones(1,lc);
        for l = 1:3:c/lc
        P(k,l*lc+1:(l+1)*lc) = zc;,P(k,(l+1)*lc+1:(l+2)*lc) = nc;
        end
end

if N == 2, Ps = sum(P)+P(2,:);, else
Ps = sum(P) + sum(P(2:N,:));, end
ind = find(Ps==0);
Pa = P(:,ind);
P = Pa;
%eval(['save Ppath',int2str(N),' P'])
return

function ff = buildf(P,f,f1);
%function ff = buildf(P,f,f1);
%computes effect of rf pulses on magnetisation by pathway
map = [1,2,3;4,5,6;7,8,9]';
```

```
r = length(P);
lZ = length(f(1,:));
ff = zeros(r,lZ);
f1 = f1*ones(1,lZ);
ff(1,:) = f1(map(P(1)+2,0+2),:);
for k = 2:r
ff(k,:) = f(map(P(k)+2,P(k-1)+2),:);
end
ff = prod(ff);
return
**********
function [f,R] = RotationMf(al,be,th);
%function [f,R] = RotationMf(al,be,th);
% al is angle from xy plane -- offres component
% be is phase angle
% th is angle of rotation about Beff
th = -th;

Sa = sin(al);, Sas = Sa^2;, S2a = sin(2*al);
Sb = sin(be);, Sbs = Sb^2;, S2b = sin(2*be);
St = sin(th);, Sts = St^2;, S2ts = (sin(th/2))^2;
Ca = cos(al);, Cas = Ca^2;
Cb = cos(be);, Cbs = Cb^2;
Ct = cos(th);, Cts = Ct^2;


R = [Sbs*Ct+Cbs*(Cas+Sas*Ct), -Sa*St+S2b*Cas*S2ts, Sb*Ca*St+Cb*S2a*S2ts;
    +Sa*St+S2b*Cas*S2ts, Cbs*Ct+Sbs*(Cas+Sas*Ct), -Cb*Ca*St+Sb*S2a*S2ts;
        -Sb*Ca*St+Cb*S2a*S2ts, +Cb*Ca*St+Sb*S2a*S2ts, Sas+Cas*Ct];

f = zeros(3,3);
f(3,3) = (R(1,1)+R(2,2))/2 + i*(R(2,1)-R(1,2))/2;
f(1,1) = conj(f(3,3));
f(3,1) = (R(1,1)-R(2,2))/2 +i*(R(2,1)+R(1,2))/2;
f(1,3) = conj(f(3,1));
f(3,2) = R(1,3)+i*R(2,3);
f(1,2) = conj(f(3,2));
f(2,3) = (R(3,1)-i*R(3,2))/2;
f(2,1) = conj(f(2,3));
f(2,2) = R(3,3);
f = f(:);

return
```

MULTI-ECHO SIMULATIONS BY BLOCH EQUATION

```
load SliceDat5/25PPP
lZ = length(Zspace);
to = clock;
NoEchoes = 32;
Mt = zeros(NoEchoes,length(Zspace));
Mz = Mt;
Mzo = Mo(3);
TE = 20e-3;
tspace = [TE:TE:NoEchoes*TE]';
B1 = 1.05;
phi = pi/2;
BigR = spalloc(3*lZ,3*lZ,9*lZ);
%Boff = randn(size(Zspace))*11.7e-3*0;
Bnom = pi/(1.500e-3*gam);
Boff = -BO*2*pi/gam;
alpha = atan(Boff/Bnom);
R180 = RotationM(alpha,phi,pi*B1);
%load Boff
%Boff = zeros(size(Zspace));
SliceThickness = 0.5;
Gslice = 2*2*pi*1500/(gam*SliceThickness);
R1 = 0.5;,R2 =5.00;
Tex = 1332e-6;
TrefE = 0e-6;
T180 = 0;
Tsp = 3e-3;
Gspstep =1;

GESpace = [0,[0.7047-5/16:1/16:0.7047+5/16]];

GESpace =0.7;
lG = length(GESpace);
if Gspstep == 0, Gsp = zeros(1,NoEchoes);, else
        temp = [NoEchoes/2*Gspstep:-Gspstep:Gspstep];
        Gsp(1:2:NoEchoes-1) = temp;
        Gsp(2:2:NoEchoes) = -temp;
end
Gsp = Gsp+256;
Gspace = -(Gsp)*pi/(gam*Tsp*SliceThickness);

for kkk = 1:lG
GspA = -(Gsp(1)+GESpace(kkk))*pi/(gam*Tsp*SliceThickness);

% Twait1 assumes 90 is infinitely narrow, and "perfectly" refocused
Twait1 = TE/2 - (TrefE+Tsp+T180/2);
        if Twait1 < 0, disp('Timing Error: Increase TE'), return, end
Twait = TE/2 - (T180/2+Tsp);
        if Twait < 0, disp('Timing Error: Increase TE'), return, end
%Mti = Mti*exp(-i*pi);
% Add Subtract Sequence
%for l = 1:2
%Mti = Mti*exp(-i*pi);
```

```
kk = 1;
Gz = Gslice;
%%%%%%%%%%%%%%%%%%%%%%%%%%%%%%%%%%%%
%Excite with Sinc Pulse
%A = [B1, phi, Z, Gz, R1, R2,Tex];
%[T,V] = ode45('excite',0,Tex,Mo);
%Lt = length(T);
%Mz(kk,k) = V(Lt,3)';, Mt(kk,k) = (V(Lt,1)+i*V(Lt,2))';
%%%%%%%%%%%%%%%%%%%%%%%%%%%%%%%%%%%%

%%Evolve With Slice Refocussing Gradient
Gz = -Gslice;, Tev = TrefE;
[Mz(kk,:),Mt(kk,:)] = Evolve(Mzi,Mti,Tev,0,R2,Gz,Zspace,Boff);

%Evolve Without Gradients

Tev = Twait1;
[Mz(kk,:),Mt(kk,:)] = Evolve(Mz(kk,:),Mt(kk,:),Tev,0,R2,0,Zspace,Boff);

%Turn on First Spoiler Gradient
Gz = GspA;, Tev = Tsp;
[Mz(kk,:),Mt(kk,:)] = Evolve(Mz(kk,:),Mt(kk,:),Tev,0,R2,Gz,Zspace,Boff);

%%Turn on Refocusing Pulse
M = [real(Mt(kk,:));imag(Mt(kk,:));Mz(kk,:)];
M = R180*M;
Mz(kk,:) = M(3,:);, Mt(kk,:) = M(1,:)+i*M(2,:);

%Bnom = pi/(1.326e-3*gam);
%alpha = atan(Boff/Bnom);
%for kz = 1:length(Zspace)
%  kz3 = kz*3;
%  R180 = RotationM(alpha(kz),phi,pi*B1);
%  BigR(kz3-2:kz3,kz3-2:kz3) = R180;
%end

%M = [real(Mt(kk,:));imag(Mt(kk,:));Mz(kk,:)];
%BigM = M(:);
%BigM = BigR*BigM;
%M = reshape(BigM,3,lZ);
%Mz(kk,:) = M(3,:);, Mt(kk,:) = M(1,:)+i*M(2,:);

%Turn on Spoiler Gradient
Gz = Gspace(kk);, Tev = Tsp;
[Mz(kk,:),Mt(kk,:)] = Evolve(Mz(kk,:),Mt(kk,:),Tev,R1,R2,Gz,Zspace,Boff);

%Evolve Without Gradients
Tev = Twait;
[Mz(kk,:),Mt(kk,:)] = Evolve(Mz(kk,:),Mt(kk,:),Tev,R1,R2,0,Zspace,Boff);


%%%%%%%%%%%%%%%%%%%%%%%%%%%%
% Collect First Echo
%%%%%%%%%%%%%%%%%%%%%%%%%%%%
%keyboard
```

```
for kk = 2:NoEchoes
%disp(kk)
%Evolve Without Gradients
Tev = Twait;
[Mz(kk,:),Mt(kk,:)] = Evolve(Mz(kk-1,:),Mt(kk-1,:),Tev,R1,R2,0,Zspace,Boff);

%Turn on Spoiler Gradient
Gz = Gspace(kk);, Tev = Tsp;
[Mz(kk,:),Mt(kk,:)] = Evolve(Mz(kk,:),Mt(kk,:),Tev,R1,R2,Gz,Zspace,Boff);

%Turn on Refocusing Pulse
M = [real(Mt(kk,:));imag(Mt(kk,:));Mz(kk,:)];
M = R180*M;
Mz(kk,:) = M(3,:);, Mt(kk,:) = M(1,:)+i*M(2,:);

%M = [real(Mt(kk,:));imag(Mt(kk,:));Mz(kk,:)];
%BigM = M(:);
%BigM = BigR*BigM;
%M = reshape(BigM,3,lZ);
%Mz(kk,:) = M(3,:);, Mt(kk,:) = M(1,:)+i*M(2,:);

%Turn on Spoiler Gradient
Gz = Gspace(kk);, Tev = Tsp;
[Mz(kk,:),Mt(kk,:)] = Evolve(Mz(kk,:),Mt(kk,:),Tev,R1,R2,Gz,Zspace,Boff);

%Evolve Without Gradients
Tev = Twait;
[Mz(kk,:),Mt(kk,:)] = Evolve(Mz(kk,:),Mt(kk,:),Tev,R1,R2,0,Zspace,Boff);

%%%%%%%%%%%%%%%%%%%%%%%%%%%%%%%%%%%%%%%%
% Collect kkth Echo
%%%%%%%%%%%%%%%%%%%%%%%%%%%%%%%%%%%%%%%%
%keyboard
end
Eto(:,kkk) = abs(sum(Mt'))';

end
%etime(clock,to)
```